Protoplanetary disk dynamics in high dust-to-gas ratio environments

Matías Gárate Silva

München 2020

Protoplanetary disk dynamics in high dust-to-gas ratio environments

Matías Gárate Silva

Dissertation
an der Fakultät für Physik
der Ludwig–Maximilians–Universität
München

vorgelegt von
Matías Gárate Silva
aus Santiago, Chile

München, den 24.07.2020

Erstgutachter: Prof. Dr. Til Birnstiel
Zweitgutachter: Prof. Dr. Barbara Ercolano
Tag der mündlichen Prüfung: 24.09.2020

Contents

List of Figures

List of Tables

Zusammenfassung

Protoplanetare Scheiben sind der Geburtsort von Planeten. Gas und Staub umkreisen den Zentralstern und unterliegen den Effekten der Schwerkraft, des Drucks, der Turbulenzen und der gegenseitigen Wechselwirkung. Mit dem Aufkommen neuer Teleskope benötigen wir mehr denn je genaue Modelle zur Interpretation der Beobachtungen der Scheiben, die eine Vielzahl von Unterstrukturen aufweisen. In dieser Arbeit untersuchen wir die Wirkung der gegenseitigen Wechselwirkung zwischen Gas und Staub auf die Dynamik und Entwicklung protoplanetarer Scheiben, insbesondere in den Fällen, in denen das Staub-zu-Gas-Verhältnis hoch genug ist, sodass die Festkörper dynamisch wichtig werden. Wir leiten die kollektive Gas- und Staubdynamik aus den Impulserhaltungsgleichungen her, indem wir die Wechselwirkung vom Staub auf die Gas-Reibung einbeziehen und dabei den Beitrag mehrerer Staubarten berücksichtigen. Die resultierenden Geschwindigkeiten werden in die Evolutions-Software `Dustpy` und `Twopoppy` implementiert, welche die protoplanetaren Scheibe, die Advektion der Gas- und Staubkomponenten der protoplanetaren Scheibe zusammen mit dem Wachstum von Festkörpern durch Koagulation und Fragmentation lösen. Schließlich kombinieren wir unsere Gleichungen für die Fluiddynamik mit verschiedenen Scheibenszenarien, darunter die Reaktivierung einer "Dead Zone", die Verdampfung und Kondensation von Wasser an der Schneegrenze und die Entwicklung einer Scheibe unter dem Einfluss von photoevaporationsgetriebenen Winden. Wir charakterisieren die Wirkung der Staubwechselwirkung auf die Gas- und Staubdynamik in verschiedenen Szenarien. Wir stellen dabei fest, dass im Falle einer Dead-Zone-Reaktivierung der hohe Staubgehalt, der sich in den inneren Regionen ansammelt, die kollektive Scheibenentwicklung verlangsamt, da durch die gleiche viskose Kraft mehr Material abtransportiert werden muss. An der Schneegrenze kann die Staubwechselwirkung den Gasstrom stoppen, die innere und äußere Scheibe in Bezug auf den Gasfluss trennen und sowohl die radiale Ausdehnung als auch die Konzentration der Staubansammlungen erhöhen. Außerdem werden Staubringe, die sich am Rand einer photoevaporations-getriebenen Lücke bilden, über eine größere Fläche verteilt, da die Staub-Rückwirkung das Gasdruckprofil glättet, indem sie Material vom Druckmaximum wegdrückt. Zudem stellen wir fest, dass die Rückreaktion die Scheibenentwicklung nur in Umgebungen mit hohen Staub-zu-Gas-Verhältnissen, niedriger turbulenter Viskosität und bei großen Partikelgrößen merklich beeinflusst. Unsere Arbeit zeigt die Auswirkungen der Staub-Wechselwirkung auf die globale Scheibendynamik und kann verwendet werden, um Beobachtungssignaturen besser zu charakterisieren, indem ein genaueres Modell für die

Staubverteilung sowie ein Leitfaden zur Beurteilung der Frage bereitgestellt wird, ob die Staubwechselwirkung in der Scheibenentwicklung berücksichtigt werden sollte.

Abstract

Protoplanetary disks are the birthplace of planets. Gas and dust orbit around the central star subject to the forces of gravity, pressure, turbulence, and mutual drag. With the advent of the new telescopes, we need more than ever accurate models to interpret the observations of disks, which display a wide variety of substructures. In this work we study the effect of the mutual drag force between gas and dust on protoplanetary disk dynamics and evolution, particularly in the cases where the dust-to-gas ratio is high enough for the solids to become dynamically important. We derive the collective gas and dust dynamics from the momentum conservation equations, by including the back-reaction from the dust to the gas drag force, and considering the contribution of multiple dust species. The resulting velocities are implemented into the protoplanetary disk evolution codes `Dustpy` and `Twopoppy`, that solve the advection of the gas and dust components of the protoplanetary disk, along with the growth of solids through coagulation and fragmentation. Finally, we combine our equations for the fluid dynamics with different disk scenarios, including: the re-activation of a dead zone, the evaporation and condensation of water at the snowline, and the evolution of a photo-evaporative disk. We characterize the effect of dust back-reaction on the gas and dust dynamics in the different scenarios. We find that in the event of a dead zone re-activation the high dust content accumulated in the inner regions damps the collective disk motion, since more material is carried away by the same viscous force. At the snowline the dust back-reaction can stop the gas flow, disconnect the inner and outer disk in terms of gas accretion, and enhance both the radial extend and the level concentration of dust accumulations. Also, dust rings formed at the edge of a photo-evaporative gap are spread over a wider area, since the dust back-reaction smooths the gas pressure profile by pushing the material away from the pressure maximum. Lastly, we find that the back-reaction only affects the disk motion in environments with high dust-to-gas ratios, low turbulent viscosity, and large particle sizes. Our work shows the effects of the the dust back-reaction on the global disk dynamics, and can be used to better characterize observational signatures, by providing a more accurate model for the dust distribution, as well as a guideline to assess whether the dust back-reaction should be considered, given the disk conditions.

Chapter 1

Introduction

In the last decade, with the advent of new telescopes and instruments, protoplanetary disk observations have revolutionized our understanding of planet formation. We transitioned from having only spectral information and unresolved images, to high-angular resolution images of gas and dust in scattered-light, millimeter continuum, and narrow band-emission. The observations have revealed disks with multiple rings, gaps, and signposts of planet formation, which previously where only studied through theoretical models. Similarly, numerical models have grown more complex, allowing us to make testable predictions about these disks, and to explain the observed features.

Studying the evolution of protoplanetary disks can help us to understand the diversity of exoplanetary systems found in the recent decades, the process of planet formation, and the diversity of disk morphologies found since the first ALMA observation of HL Tau (ALMA Partnership et al., 2015; Ansdell et al., 2016; Andrews et al., 2018).

Protoplanetary disks are born during the process of star formation. It all begins when a cloud of gas and dust collapses due to its own gravity, resulting in a central star and the surrounding envelope orbiting around it.

As the envelope contracts, it also speeds up due to the conservation of angular momentum. The centrifugal force balances the radial component of the stellar gravity (when viewed in cylindrical coordinates in the rotation frame of the material), while the vertical component forces the material to settle towards the midplane, until the pressure support is strong enough to counter the stellar gravity.

The evolution of protoplanetary disks lasts for approximately 10 Myr (Strom et al., 1989; Skrutskie et al., 1990; Haisch et al., 2001), and ends once all the material has been dispersed, accreted into the star, or transformed into planets and debris disks.

The dynamic of disk is affected by several forces acting over the gas and dust component. These include the stellar gravity, the gas pressure, the viscous drag, the magnetic force, the radiation pressure, the torque exerted by a forming planet, and the drag force between gas and dust, among others.

In the classical disk evolution models the dust is assumed to be only a 1% of the total gas mass, as in the interstellar medium (ISM, Bohlin et al., 1978). Under this assumption, the drag force exerted by the dust onto the gas is negligible for their collective evolution, and

the gas component evolve independently of the solid grains. However, both observations and theoretical models show that the dust grains can concentrate in different regions of the disk (Pinilla et al., 2012; ALMA Partnership et al., 2015), reaching higher dust-to-gas ratios for which the dust back-reaction becomes dynamically important for the collective gas and dust evolution.
In this work we extend the traditional expressions for the gas and dust velocities, by including the contribution of the drag force back-reaction from the dust onto the gas, and study the disk evolution in high dust-to-gas ratio environments considering the collective gas and dust dynamics.
This thesis is structured as follows:
In Chapter 1 we review the classical model of gas and dust evolution, where the dust back-reaction is typically ignored.
In Chapter 2 we derive the correct expressions for the gas and dust velocities considering the dust back-reaction onto the gas, and analyse the new expressions.
In Chapter 3 we perform numerical simulations of protoplanetary disks that illustrate the effects of dust back-reaction.
In Chapter 4 and 5 we study the disk evolution by considering respectively: the reactivation of a dead zone, the water snowline.
In Chapter 6 we report our work in progress in the study case of dust accumulation around a gap, opened either by photo-evaporation or by a massive planet.
In Chapter 7 we summarize our work and propose future applications in which the collective dynamics of gas and dust might be a key ingredient.

1.1 Evolution of a gas disk

Observations of young star forming regions reveal that protoplanetary disks are typically found in systems younger than 10 Myrs (Haisch et al., 2001). During this time all the gas must be either accreted towards the star or blown away. Currently, we know of three mechanisms that can lead to disk dispersal: viscous accretion (Shakura & Sunyaev, 1973; Lynden-Bell & Pringle, 1974), photo-evaporation (Alexander et al., 2006a,b), and magnetic driven winds (Blandford & Payne, 1982). These processes work by either redistributing the material across the disk, or by removing it into the interstellar medium.
The mass transport of the gas disk can be modelled as a continuity equation:

$$\frac{\partial}{\partial t}\left(r\,\Sigma_{\rm g}\right)+\frac{\partial}{\partial r}\left(r\,\Sigma_{\rm g}\,v_{\rm g,r}\right)=0 \tag{1.1}$$

where $\Sigma_{\rm g}$ is the gas surface density of the disk, r is the distance to the central star, and $v_{\rm g,r}$ is the gas velocity in the radial direction.
We use this advection equation in our disk evolution models, assuming axial symmetry and vertical hydro-static equilibrium. While this assumption is simple, it allows to incorporate more ingredients in the models, and understand the basic principles that govern the disk evolution. Moreover, high angular resolution observations show that most disks

are axisymmetric (see DSHARP observations, Andrews et al., 2018), despite presenting substructures.
While this approximation is good in general, we should note that it will fail fail in situations where the disk rotation deviate significantly from keplerian motion, such as in regions with steep pressure gradients, massive self-gravitating disks that present fragmentation (Lichtenberg & Schleicher, 2015), or disks with a massive companion that creates strong perturbations, such as spirals or a tilted inner disk (Cuello et al., 2019a; Nealon et al., 2020).
Now we proceed to describe each of the gas dispersal mechanisms, along with the equations relevant to our model.

1.1.1 Viscous accretion

Observations reveal that protoplanetary disks present a wide range of accretion rates onto the star, with values ranging between $10^{-10}\,\mathrm{M}_\odot/\mathrm{yr}$ to $10^{-6}\,\mathrm{M}_\odot/\mathrm{yr}$ (Hartigan et al., 1995; Manara et al., 2017), varying with the age, mass, and morphology of the disk.
To produce such accretion rates, there must exist an underlying process responsible of transporting the material towards the star.
In a keplerian disk orbiting around a star with mass M_*, the material orbits with an angular velocity of:

$$\Omega_K = \sqrt{\frac{GM_*}{r^3}}, \tag{1.2}$$

with G the gravitational constant.
In such a disk, the exchange of material between two neighboring rings of gas results in the outwards transport of angular momentum, causing the inner ring to spread inward while the outer ring spreads outwards. On global scales, this causes in the inner regions of the disk to be accreted towards the star while the outer regions disperse outwards (Lynden-Bell & Pringle, 1974; Pringle, 1981).
The efficiency of the angular momentum transport is controlled by the exchange of material between adjacent gas parcels. The observed disk lifetimes and the corresponding accretion rates indicate that molecular diffusivity is too low to be the dominant driver of disk accretion. Turbulence, which transports material much faster, is a better candidate to fit the observational constraints, and can can be modeled as a viscous torque acting over the fluid, which results in the gas evolving as a diffusive process (Lüst, 1952; Lynden-Bell & Pringle, 1974):

$$\frac{\partial \Sigma_\mathrm{g}}{\partial t} = \frac{3}{r}\frac{\partial}{\partial r}\left(r^{1/2}\frac{\partial}{\partial r}\left(\nu\Sigma_\mathrm{g} r^{1/2}\right)\right), \tag{1.3}$$

where ν is the viscosity of the material.
The turbulent viscosity ν, can be written according to the α model (Shakura & Sunyaev, 1973) as follows:

$$\nu = \alpha\, c_s^2 \Omega_K^{-1}, \tag{1.4}$$

where c_s is the gas isothermal sound speed:

$$c_s = \sqrt{\frac{k_{\rm B} T}{\mu m_{\rm H}}}, \tag{1.5}$$

with $k_{\rm B}$ the Boltzmann constant, T the gas temperature, μ the mean molecular weight, and $m_{\rm H}$ the hydrogen mass.
The dimensionless α parameter (with $\alpha < 1$) controls the strength of the turbulent viscosity. Numerical models indicate that the α parameter has values between 10^{-4} to 10^{-1}, depending on the physical process that drives the turbulence.
Some of the instabilities that can stir the gas turbulence are the Magneto Rotational Instability (MRI, Balbus & Hawley, 1991), the Vertical Shear Instability (VSI, Nelson et al., 2013; Stoll & Kley, 2014), and the Gravitational Instability (GI, Lin & Pringle, 1987), among others.
The viscous evolution of the disk, written as a diffusive process in Equation 1.3, can also be expressed as an advection equation (1.1), with the following viscous velocity:

$$v_\nu = -\frac{3}{\Sigma_{\rm g}\sqrt{r}} \frac{\partial}{\partial r}(\nu \, \Sigma_{\rm g} \sqrt{r}). \tag{1.6}$$

In terms of the momentum conservation equation, the force responsible for viscous diffusion can be written as:

$$f_\nu = \frac{1}{2} \Omega_K v_\nu, \tag{1.7}$$

where f_ν is the viscous force per mass unit in the azimuthal direction. We find that the expression for the viscous velocity v_ν, and the viscous force f_ν are particularly useful to re-derive the gas velocity in presence of additional force terms, as we will do in Chapter 2.

Steady state solution

If the disk evolution is dominated by viscous accretion, then Equation 1.1 has a steady state solution given by:

$$3\,\pi\,\Sigma_{\rm g}\,\nu = \dot{M}_{\rm g} \left(1 - \sqrt{\frac{r_{\rm in}}{r}}\right), \tag{1.8}$$

with $r_{\rm in}$ the disk inner boundary (where the torque is assumed to be zero), and the gas accretion rate $\dot{M}_{\rm g}$ being constant in time and radii. In the disk regions far from the inner edge ($r \gg r_{\rm in}$), this solution can be simplified to:

$$3\,\pi\,\Sigma_{\rm g}\,\nu = \dot{M}_{\rm g}, \tag{1.9}$$

which implies that the gas surface density is inversely proportional to the viscosity ν in steady state. In particular, for a disk with α-viscosity, and a temperature profile of $T \propto r^{-q}$, the steady state gas surface density follows a power law profile:

$$\Sigma_{\rm g}(r) = \Sigma_0 \left(\frac{r}{r_0}\right)^{-p}. \tag{1.10}$$

with Σ_0 and r_0 the normalization parameters, and $p = 3/2 - q$ the power law exponent. For a characteristic irradiated disk the temperature profile presents a value of $q = 0.5$, and $p = 1$.
Another consequence of the steady state solution is that regions with low turbulent viscosity act as a bottleneck for the gas accretion, accumulating more material than regions with higher viscosity. Dead zones, which are regions with low turbulence due to an inefficient MRI (Gammie, 1996), show this behavior. As we see in Gárate et al. (2019) (see also Chapter 4), these regions also act as dust traps, and are an ideal scenario to study the collective gas and dust dynamics.

Self similar solution

Another analytical solution to the advection equation has the form of a power law with an exponential cut-off:

$$\Sigma_{\rm g}(r) = \Sigma_0 \left(\frac{r}{r_0}\right)^{-1} \exp(-r/r_c), \tag{1.11}$$

where Σ_0 and r_0 are the normalization values of the profile, and r_c is the cut-off radius. This expression assumes that the disk has an outer edge, while the power-law profile assumes that the disk extends to infinity.
The viscous evolution of this profile retains the same shape of Equation 1.11, while the parameters $\Sigma_0(t)$ and $r_c(t)$ change with time. Because of this property, this profile is called the self-similar solution (Lynden-Bell & Pringle, 1974). In Equation 1.11 we show the particular solution valid for $\nu \propto r$ (which is consistent disk with an α-viscosity profile, and a $q = 0.5$ temperature profile, Equation 1.4).

1.1.2 Photo-evaporation dispersal

Besides the viscous diffusion of material, the protoplanetary disk can also lose gas through photo-evaporative winds (Alexander et al., 2006a). This is the case when the radiation emitted by the central star (or neighboring stars) in the high energy range (Far UV, Extreme UV, and X-Ray) is intense enough to unbound the gas from the surface layers of the protoplanetary disk.
The outer regions of the disk, where the material is loosely bound to the star, are more susceptible to photo-evaporation than the inner regions. The gravitational radius, for which the thermal energy of the excited material exceeds the gravitational energy (Alexander et al., 2006b), is given by:

$$r_g = \frac{GM_*}{c_s^2}. \tag{1.12}$$

This can be modeled as a loss term $\dot{\Sigma}_{\rm wind}$, that acts on the regions where $r \geq r_g$. This approach assumes that only the angular momentum of the ejected material is removed from the disk, without accelerating the remaining material.
A consequence of the mass loss through photo-evaporation is the opening of a gap at the

gravitational radius, since the material in the inner regions continues to evolve through viscous accretion, while the material in the outer regions is dispersed (Alexander et al., 2006a), disconnecting the inner and outer regions in terms of mass accretion, and leading to an inside-out dispersal of the disk mass (Koepferl et al., 2013).
After the cavity is opened, we expect to find different observational signatures. First, the depletion of the inner regions should lead to a reduced NIR emission, characteristic of "transition disks" objects, though it is worth noting that photo-evaporation is not the only mechanism that can lead to transition disk signatures. Planets, for example can also clear the inner regions (for a review on transition disks, see Espaillat et al., 2014).
Another consequence of the gap opening, is the creation of a pressure maximum in the gas and the outer boundary of the cavity. As we will see in the following sections, this region can become a dust trap, and present itself as a dust ring in the observations.

1.1.3 Wind-Driven dispersal

Another method that has been proposed to explain disk dispersal is the presence of magnetic driven winds (Suzuki & Inutsuka, 2009). In a disk with a vertical magnetic field component, the surface of the disk experiences an additional torque that can accelerate and launch the material away (Blandford & Payne, 1982). The escaped material carries part of the disk angular momentum, which in turn, causes the remaining gas to drift inwards.
However, recent simulations show that the magnetic winds can only drive a minor fraction of the total angular momentum transport and the accretion rate onto the star, and therefore would not contribute to the disk dispersal. (Zhu & Stone, 2018).
From the reviews of Turner et al. (2014); Ercolano & Pascucci (2017) it seems that the net effect of magnetic winds onto the disk evolution is not yet understood.
For this reason, among others, we will leave this component of the disk evolution outside the scope of this work, as it is not clear what the interaction between magnetic winds and dust evolution might be.
In the future, once we can determine a reliable mass loss rate profile, we extend our implementation of disk dispersal through photo-evaporation (see Chapter 6), by adjusting it to the magnetic winds mechanism.

1.2 Gas orbital motion

A test particle in a protoplanetary disk is subject to the stellar gravity and orbits the star at keplerian speed $v_K = \Omega_K r$. However, a parcel of gas also experiences a pressure force that can aid or oppose the stellar gravity in the radial direction:

$$f_P = -\frac{1}{\rho_{g,0}} \frac{\partial P}{\partial r}, \tag{1.13}$$

where $\rho_{g,0}$ is the gas volume density at the midplane, $P = \rho_{g,0}\, c_s^2$ is the isothermal gas pressure.
Approximating to first order, the resulting difference between the keplerian velocity and the gas orbital velocity is:

$$v_P = -\frac{1}{2}\left(\frac{h_g}{r}\right)^2 \frac{\partial \log P}{\partial \log r} v_K, \tag{1.14}$$

where h_g is the gas scale height given by:

$$h_g = c_s\, \Omega_K^{-1}. \tag{1.15}$$

Through this work we call v_P the "pressure velocity", though in the literature it can also be found as $v_P = \eta v_K$ (Nakagawa et al., 1986), with η the corresponding pre-factor from Equation 1.14. For a smooth disk, the pressure gradient is negative, meaning that the gas orbits at sub-keplerian speed, however, if the disk presents any pressure maximum, the regions with positive pressure gradient will orbit at super-keplerian speed.
Though the pressure velocity is only a small fraction of the keplerian orbital speed (typically $v_P \sim 10^{-3} v_K$), this difference dominates the drag force between gas and dust, as we will see in the following sections.

1.3 Dust dynamics

The dust component of protoplanetary disks comes in a wide range of sizes, from micron-sized grains to millimeter pebbles. Near and far infrared observations from Spitzer, Herschel and other telescopes trace the hot emission from small particles, while interferometric observations from ALMA reveal the structures made by large millimeter particles.
Both theory and observations agree that the gas and dust components behave different, and that different particle species behave in a different manner. The observations of the TW Hya disk are a good example of how the line emission from the gas (Huang et al., 2018), the scattered-light from small micrometer dust grains (van Boekel et al., 2017), and the continuum emission from millimeter large grains show a different radial extend, and different sub-structures (Andrews et al., 2016). Observable quantities, like the spectral index, also suggest that large grains drift towards the inner regions (Tazzari et al., 2016; Tripathi et al., 2018).
Finally, observations of different types of sub-structures (spirals, gaps, etc) indicate underlying dust and gas interactions (see section 5.3.1 of Andrews, 2020).
The radial transport of dust particles across the disk can be modeled with a continuity equation, as in Equation 1.1, with the addition of a dust diffusivity term:

$$\frac{\partial}{\partial t}\left(r\, \Sigma_{\rm d}(m)\right) + \frac{\partial}{\partial r}\left(r\, \Sigma_{\rm d}(m)\, v_{\rm d,r}(m)\right) - \frac{\partial}{\partial r}\left(r D_{\rm d}(m) \Sigma_{\rm g} \frac{\partial}{\partial r}\left(\frac{\Sigma_{\rm d}(m)}{\Sigma_{\rm g}}\right)\right) = 0, \tag{1.16}$$

where $\Sigma_{\rm d}$, $v_{\rm d,r}$, and $D_{\rm d}$ correspond to the surface density, radial velocity, and diffusivity of a particular dust species of mass m.

The dynamics of a dust grain depends on its interaction with the gas through the drag force, which in turn depends on the particle size and the difference between gas and dust velocities. The drag force exerted by the gas onto the dust (per mass) is:

$$f_{D,\mathrm{d}} = -\frac{(\mathbf{v}_\mathrm{d} - \mathbf{v}_\mathrm{g})}{t_\mathrm{stop}}, \tag{1.17}$$

where t_stop is the stopping time, defined as the time required for a dust particle to couple to the gas motion.
The value of the stopping time depends on the particle size and the drag force regime. For our work we consider only the Epstein and the Stokes I drag regimes (Weidenschilling, 1977; Birnstiel et al., 2010), for small and large particles respectively, and it is defined as:

$$t_\mathrm{stop} = \begin{cases} \sqrt{\frac{\pi}{8}}\frac{\rho_s}{\rho_\mathrm{g}}\frac{a}{c_s} & \lambda_\mathrm{mfp}/a \geq 4/9 \\ \frac{4}{9}\sqrt{\frac{\pi}{8}}\frac{\rho_s}{\rho_\mathrm{g}}\frac{a^2}{c_s}\frac{1}{\lambda_\mathrm{mfp}} & \lambda_\mathrm{mfp}/a < 4/9. \end{cases} \tag{1.18}$$

Here a is the particle size, ρ_s is the material density for a dust particle, and λ_mfp is the gas mean free path:

$$\lambda_\mathrm{mfp} = \frac{\mu\, m_\mathrm{H}}{\rho_g\, \sigma_{\mathrm{H}_2}}, \tag{1.19}$$

with $\sigma_{\mathrm{H}_2} = 2 \times 10^{-15}\,\mathrm{cm}^2$ the cross section of molecular hydrogen. Assuming a constant internal density, the mass of a dust grain relates to its size through:

$$m = \frac{4\pi}{3}\rho_s a^3. \tag{1.20}$$

Another useful quantity to characterize the dust motion is the Stokes number, or dimensionless stopping time:

$$\mathrm{St} = t_\mathrm{stop}\,\Omega_K, \tag{1.21}$$

which defines the coupling time in function of the local orbital frequency. At the midplane, the Stokes number can be written as:

$$\mathrm{St} = \begin{cases} \frac{\pi}{2}\frac{a\rho_s}{\Sigma_\mathrm{g}} & \lambda_\mathrm{mfp}/a \geq 4/9 \\ \frac{2\pi}{9}\frac{a^2\rho_s}{\lambda_\mathrm{mfp}\Sigma_\mathrm{g}} & \lambda_\mathrm{mfp}/a < 4/9. \end{cases} \tag{1.22}$$

The dust velocity can be obtained by assuming that the solid particles only experience the stellar gravity and the drag force (Equation 1.17). The radial dust motion is then a function of the gas velocity and the Stokes number (Nakagawa et al., 1986; Takeuchi & Lin, 2002):

$$v_\mathrm{d,r} = \frac{1}{1+\mathrm{St}^2}v_\nu - \frac{2\mathrm{St}}{1+\mathrm{St}^2}v_P. \tag{1.23}$$

From this equation we notice how the dust motion depends on the particle size. Small particles ($\mathrm{St} \ll 1$) move along with the gas at viscous speed, large particles ($\mathrm{St} \gg 1$) are decoupled from the gas and stay in a fixed orbit, and mid-size particles ($\mathrm{St} \approx 1$) drift towards the pressure maximum with a speed of $v_\mathrm{d,r} \approx -v_P$ (Whipple, 1972; Weidenschilling, 1977; Nakagawa et al., 1986, considering that typically $|v_P| \gg |v_\nu|$).

1.3.1 Dust drifting and trapping

From the dust radial velocity (Equation 1.23) we notice that in a smooth disk with a pressure profile that decreases with radii, solids with St ~ 1 drift inwards.
Drifting can be understood as a consequence of the angular momentum exchange between gas and dust. Since the gas is pressure supported it tends to orbit more slowly than the dust. This difference in velocities causes the dust to feel the gas motion as a head-wind, and to lose angular momentum. The loss of angular momentum in a protoplantary disk results then in inward drifting (Whipple, 1972; Weidenschilling, 1977; Nakagawa et al., 1986).
To first order, we can approximate the time required for a dust particle fall into the central star as:

$$t_{\rm drift} \approx \frac{r}{\mathrm{St}\, v_P}. \tag{1.24}$$

For a simple model of the solar nebula, a particle of 1 m at 1 AU has a St $= 1$, and a would drift in $t_{\rm drift} = 100$ yrs into the star (Weidenschilling, 1977). However, drifting only limits the particle growth in the outer regions of the disk, since other mechanisms prevent solids from large particles sizes in the inner regions.
A consequence of dust drifting is that pebble sized particles can be trapped at local pressure maximums in the disk, since the drifting velocity is $v_P = 0$ in regions where $\partial_{\rm r} P = 0$ (Whipple, 1972; Pinilla et al., 2012).
Pressure maximums can be caused by different mechanisms, such as the accumulation of gas in a dead zone (Kretke et al., 2009), or the opening of a gap due to the gravity of a planet (Pinilla et al., 2012), or due to photo-evaporation (Alexander & Armitage, 2007).
Observations of ALMA reveal that millimeter size particles accumulate at different radii through the disk, forming ring like structures (ALMA Partnership et al., 2015; Andrews et al., 2016, 2018). The most popular explanation is that a planet is causing the gap opening and ring formation, however other mechanisms may also cause these structures, and one planet may form multiple structures (Gonzalez et al., 2015).
Simultaneously, these regions where dust accumulate become ideal candidates for subsequent planet formation Chatterjee & Tan (2014).
Besides dust trapping, dust particles can also accumulate if there are radial changes in the size of the dust population (Birnstiel et al., 2010, 2012; Pinilla et al., 2017; Drążkowska & Alibert, 2017). For example, if the particles in the inner regions are smaller than the particles in the outer regions, the former will move slowly (following the viscous speed of the gas), while the later will drift faster towards the inner regions. Difference in the particle velocity would cause the accumulation of dust in the inner regions due to a traffic jam effect.

1.3.2 Dust diffusivity

The diffusion term of dust particles included in Equation 1.16, acts by diffusing the concentration of dust particles, relative to the gas content (Birnstiel et al., 2010).

The dust diffusivity is modeled as:

$$D_{\rm d} = \frac{\nu}{1+{\rm St}^2}, \tag{1.25}$$

which considers that larger particles are less affected by the gas turbulence (Youdin & Lithwick, 2007).
This particular treatment for the dust diffusion does not take into account high dust-to-gas ratios, though we describe a possible correction for the total dust content in Chapter 2.
Though a more appropriate diffusion approach for the dust would be to use the expression $\partial_r \Sigma_{\rm d}$ instead of $\Sigma_{\rm g}\partial_r(\Sigma_{\rm d}/\Sigma_{\rm g})$ in the diffusion term of Equation 1.16, since the latter accounts for a constant gas surface density, we do not expect a major difference in the net outcome of the simulations.

1.3.3 Motivation for dust back-reaction.

So far we have assumed that the gas radial velocity corresponds to the viscous velocity ($v_{\rm g,r} = v_\nu$), and that the gas orbital velocity differs from the keplerian only by the effect of the pressure gradient ($v_{{\rm g},\theta} = v_K - v_P$). This assumption is only valid if the dust back-reaction does not perturb the gas motion, or in other words, if the drag force $f_{D,{\rm g}}$ onto the gas is negligible, with:

$$f_{D,{\rm g}} = \sum_m \frac{(\mathbf{v}_{\rm d} - \mathbf{v}_{\rm g})}{t_{\rm stop}} \epsilon_m, \tag{1.26}$$

where m is the mass of each dust species mixed with the gas, and ϵ_m is the dust-to-gas ratio of each of these species (Tanaka et al., 2005; Dipierro et al., 2018).
In a disk where the total dust-to-gas ratio ϵ is uniform and low ($\epsilon \approx 1\%$) the back-reaction has little impact on the gas motion.
However, since dust grains can accumulate in pressure maximums and traffic jams, the local dust-to-gas ratio can increase to the point where the dust back-reaction becomes important for the collective disk dynamics.
Furthermore, the perturbation of the gas velocities also affects back the dust motion, modifying the expression given in Equation 1.23 and making it dependant on the local dust concentration.
In Chapter 2 we recalculate the gas and dust velocities from the momentum equation, and present a general expression including the back-reaction effects.

1.4 Dust growth

In the early stages of the protoplanetary disk formation, the dust grains originated from the ISM are typically micron sized (Bohlin et al., 1978). Laboratory and numerical experiments indicate these grains grow through collision and sticking, reaching millimeter and centimeter sizes (Blum & Wurm, 2008; Birnstiel et al., 2010; Windmark et al., 2012). After this point, the collisions result either in bouncing or fragmentation, stopping the particle

growth.
Due to the disk turbulence, characterized by the α parameter (Ormel & Cuzzi, 2007), the impact speed between equal size particles is:

$$\Delta v_\alpha \approx \sqrt{\frac{3\alpha}{\mathrm{St} + \mathrm{St}^{-1}}} c_s. \tag{1.27}$$

If the maximum impact speed that a particle can withstand is v_{frag} (Brauer et al., 2008a; Birnstiel et al., 2009), then the fragmentation limit (for particles with $\mathrm{St} < 1$) is given by:

$$\mathrm{St}_{\mathrm{frag}} = \frac{1}{3} \frac{v_{\mathrm{frag}}^2}{\alpha c_s^2}. \tag{1.28}$$

The value of v_{frag} depends on the material properties. A silicate grain in a protoplanetary disk can withstand a collision of only $v_{\mathrm{frag}} = 1\,\mathrm{m\,s^{-1}}$ (Blum & Wurm, 2000; Poppe et al., 2000; Güttler et al., 2010). Ices were thought to be much stickier than silicates with fragmentations velocities of $v_{\mathrm{frag}} = 10\,\mathrm{m\,s^{-1}}$ (Wada et al., 2011; Gundlach et al., 2011; Gundlach & Blum, 2015), which means that they could grow two orders of magnitude more than silicates under the same disk conditions. However, new laboratory experiments suggest that ices could actually be only as sticky as silicates in the end (Gundlach et al., 2018; Musiolik & Wurm, 2019; Steinpilz et al., 2019).
Other mechanisms could influence the dust stickiness, such as a coating of organic material (Homma et al., 2019) which would allow particles to grow to larger sizes, or the grain porosity, that allows for further growth(Kataoka et al., 2013).
Besides the fragmentation limit, we also mentioned that large particles can drift inwards due to the interaction with the gas. If the drift timescale (Equation 1.24) of a particle is shorter than the growth timescale, then we expect the dust to move inwards before it can continue growing.
Comparing the growth timescale, which can be estimated as:

$$t_{\mathrm{growth}} = (\epsilon\, \Omega_K)^{-1}, \tag{1.29}$$

with the drift timescale, we obtain a drift limit condition for dust growth (Birnstiel et al., 2012):

$$\mathrm{St}_{\mathrm{drift}} = \left| \frac{\mathrm{dln}\, P}{\mathrm{dln}\, r} \right|^{-1} \frac{v_K^2}{c_s^2} \epsilon. \tag{1.30}$$

The current protoplanetary disk models indicate that dust growth in the inner regions tends to be limited by fragmentation, while in the outer regions it is limited by drift (Birnstiel et al., 2012), since the growth timescales are longer.

1.5 Vertical structure

For our model we consider that both the gas and the dust are in vertical hydro-static equilibrium, and therefore that any changes in the vertical direction occur faster than in

the radial direction.
In this section we describe the vertical density profile, that in Chapter 2 will be used to calculate the net radial mass flux.
In hydro-static equilibrium, the pressure force from the gas balances the vertical component of the stellar gravity, and spreads the material over the vertical direction with the following profile:

$$\rho_{\rm g}(z) = \frac{\Sigma_{\rm g}}{\sqrt{2\pi}h_{\rm g}} \exp\left(-\frac{z^2}{2h_{\rm g}^2}\right), \tag{1.31}$$

where z corresponds to the vertical coordinate. The dust vertical structure follows (approximately) a gaussian profile (Fromang & Nelson, 2009), in which the dust scale height $h_{\rm d}(m)$ depends on the particle size:

$$\rho_{\rm d}(z,m) = \frac{\Sigma_{\rm d}(m)}{\sqrt{2\pi}h_{\rm d}(m)} \exp\left(-\frac{z^2}{2h_{\rm d}^2(m)}\right). \tag{1.32}$$

Because the drag force between gas and dust depends on the particle size, different dust species settle with different scale heights when exposed to the gas turbulence (Dubrulle et al., 1995; Fromang & Nelson, 2009).
Large particles settle closer to the midplane, while small particles follow the gas structure. The dust scale height, given in Birnstiel et al. (2010), is:

$$h_{\rm d}(m) = h_{\rm g} \cdot \min\left(1, \sqrt{\frac{\alpha}{\min({\rm St}, 1/2)(1+{\rm St}^2)}}\right), \tag{1.33}$$

which for small particles can be approximated to:

$$h_{\rm d}(m) = h_{\rm g} \cdot \min\left(1, \sqrt{\frac{\alpha}{\rm St}}\right). \tag{1.34}$$

The difference in the settling for small and large grains can be observed in the disk J1608 (Villenave et al., 2019), for which the models show a grater vertical extend in the small micrometer grain component, than in the millimeter component.
The settling becomes particularly important when considering dust and gas interactions. Since large particles settle more efficiently, it means that these only interact with the gas at the midplane (which is the reason why the pressure in Equation 1.14 is in this region). On the other hand, the interactions between the gas and the small particles are uniform across the vertical direction. This difference becomes important when calculating the back-reaction effects, as we will see in Chapter 2.

1.6 Paths to planet formation

The final remnant of the evolution of a protoplanetary disk are the planets and the debris disk. Since collision and sticking only allow to form pebble size particles, another process

must be responsible to form gravitationally bound planetesimals, which then can grow into planets.

So far, one of the best candidates is the streaming instability, which is triggered by the dust and gas interactions in high-dust-to-gas ratio environments (Youdin & Goodman, 2005; Johansen et al., 2007). In small scales, the streaming instability leads to the formation of over-dense filaments of dust, which then reach densities high enough to become gravitationally unstable and collapse into planetesimals (Johansen et al., 2009).

The planetesimals then continue to grow through gravitational interactions, planetesimal capture, and pebble accretion (Lambrechts & Johansen, 2012), until reaching a mass high enough to retain an atmosphere (Pollack et al., 1996).

The dust traps discussed in Section 1.3 are ideal hot-spots for the streaming instability to occur, since large amounts of dusts are concentrated in narrow regions (Dullemond et al., 2018; Stammler et al., 2019).

An alternative way to form planets, that is independent of the particle growth, is through the gravitational instability, which is occurs when the gaseous material in a self-gravitating disk collapses into directly into a gaseous planet (Boss, 1997). This path to planet formation is more likely to occur at larger radii, contribution of the gas self-gravity to the disk dynamics increases as the sound speed and the orbital frequency decrease.

The tidal down-sizing scenario expands this last scenario, and proposes that a clump of material formed in the outer regions can migrate to the inner regions, where the envelope is stripped through tidal disruption, leaving behind the solid core which becomes then a terrestrial planet (Nayakshin, 2017).

Chapter 2

Coupled Gas and Dust Dynamics

In this chapter we derive the equations of motion for the gas and dust components in a protoplanetary disks, while accounting for the drag force exerted between the gas and dust.
We propose a formalism to characterize the dust back-reaction using a "damping" and a "pushing" coefficient (Gárate et al., 2019, 2020), that depend on the dust distribution properties. Then, we extend this definition to account for the vertical structure of the dust particles.
Here we also compare the corrected gas and dust velocities with the previous formula described in Chapter 1 for different dust-to-gas ratios and particle sizes.

2.1 Momentum Equations

As mentioned in Chapter 1, the gas is subject to the viscous force (Equation 1.7), the pressure force (Equation 1.13), the stellar gravity responsible for the orbital motion (Equation 1.2), and the drag force from the multiple dust species (Equation 1.26). Instead, the dust is only subject to the stellar gravity, and the drag force from the gas (Equation 1.17). The momentum equations for dust and gas, as given in (Kanagawa et al., 2017; Dipierro et al., 2018; Gárate et al., 2019) are:

$$\frac{\mathrm{d}\mathbf{v}_\mathrm{g}}{\mathrm{d}t} = \sum_m \frac{(\mathbf{v}_\mathrm{d} - \mathbf{v}_\mathrm{g})}{t_\mathrm{stop}} \epsilon_m - \Omega_K^2 r\, \hat{\mathbf{r}} + f_P\, \hat{\mathbf{r}} + f_\nu\, \hat{\theta}, \tag{2.1}$$

$$\frac{\mathrm{d}\mathbf{v}_\mathrm{d}}{\mathrm{d}t} = -\frac{(\mathbf{v}_\mathrm{d} - \mathbf{v}_\mathrm{g})}{t_\mathrm{stop}} - \Omega_K^2 r\, \hat{\mathbf{r}}. \tag{2.2}$$

Solving the for the gas and dust velocities in the radial and azimuthal components (assuming hydrostatic equilibrium), gives a system of four coupled equations. At this point it is convenient to define the difference between the azimuthal and keplerian velocity orbital

velocities as $\Delta v_{\mathrm{g},\theta} = v_{\mathrm{g},\theta} - v_K$, and $\Delta v_{\mathrm{d},\theta} = v_{\mathrm{d},\theta} - v_K$, for both the gas and dust respectively. The solution for the gas velocity is then:

$$v_{\mathrm{g},r} = A v_\nu + 2B v_P, \tag{2.3}$$

$$\Delta v_{\mathrm{g},\theta} = \frac{1}{2} B v_\nu - A v_P, \tag{2.4}$$

where v_ν is the viscous velocity (Equation 1.6), v_P is the pressure velocity (Equation 1.14), and A and B are the back-reaction coefficients which depend on the dust distribution (Gárate et al., 2019, 2020). We provide a formal definition for the back-reaction coefficients in the following section. For now, we only want to remark that in the dust-free limit ($\lim \epsilon \to 0$), these have values of $A = 1$, and $B = 0$, which recover the traditional gas velocities ($v_{\mathrm{g},r} = v_\nu$, $\Delta v_{\mathrm{g},\theta} = -v_P$), as given in Chapter 1.
The solution for the dust velocity, in terms of the gas velocity, is:

$$v_{\mathrm{d},r} = \frac{1}{1+\mathrm{St}^2} v_{\mathrm{g},r} + \frac{2\mathrm{St}}{1+\mathrm{St}^2} \Delta v_{\mathrm{g},\theta}, \tag{2.5}$$

$$\Delta v_{\mathrm{d},\theta} = \frac{1}{1+\mathrm{St}^2} \Delta v_{\mathrm{g},\theta} - \frac{\mathrm{St}}{2(1+\mathrm{St}^2)} v_{\mathrm{g},r}. \tag{2.6}$$

In this expression, the information about the dust distribution is included implicitly in the gas velocities. In the dust free case, the dust velocity becomes the traditional expression described in Equation 1.23 (Weidenschilling, 1977; Nakagawa et al., 1986; Takeuchi & Lin, 2002).
For completeness, the expanded expression for the dust velocity, in terms of the viscous and pressure velocity, is:

$$v_{\mathrm{d},r} = \frac{A + B\,\mathrm{St}}{1+\mathrm{St}^2} v_\nu - \frac{2(A\,\mathrm{St} - B)}{1+\mathrm{St}^2} v_P, \tag{2.7}$$

$$\Delta v_{\mathrm{d},\theta} = -\frac{A\,\mathrm{St} - B}{2(1+\mathrm{St}^2)} v_\nu - \frac{A + B\,\mathrm{St}}{1+\mathrm{St}^2} v_P. \tag{2.8}$$

The complete derivation of the gas and dust velocities from the momentum conservation equation (Equation 2.1 and 2.2), and the origin of the back-reaction coefficients, can be found in Appendix A. In Chapter 6 we extend our derivation of the gas and dust velocities by including the azimuthally averaged torque exerted by a planet.

2.2 Back-Reaction Coefficients

The back-reaction coefficients that appear in the expression for the gas velocity (Equation 2.3 and 2.4) are a function of the dust size distribution:

$$A = \frac{X+1}{Y^2 + (X+1)^2}, \tag{2.9}$$

$$B = \frac{Y}{Y^2 + (X+1)^2}, \tag{2.10}$$

where X and Y are a weighted sum of the dust distribution defined in Tanaka et al. (2005); Okuzumi et al. (2012); Dipierro et al. (2018) as:

$$X = \sum_m \frac{1}{1 + \mathrm{St}(m)^2} \epsilon(m), \tag{2.11}$$

$$Y = \sum_m \frac{\mathrm{St}(m)}{1 + \mathrm{St}(m)^2} \epsilon(m). \tag{2.12}$$

These terms appear naturally while solving the momentum equations Equation 2.1 and Equation 2.2. From these equations we can infer two properties of the back-reaction coefficients Gárate et al. (2019):

- $0 < A, B < 1$
- The limit without particles (i.e. $\epsilon \to 0$), recovers the traditional gas velocities:
  - $A \to 1$
  - $B \to 0$

From here we can interpret them based on their effect on the gas velocity. The coefficient A acts as a "damping" factor, that reduces the viscous speed in the radial direction, and reduces the effect of the pressure gradient in the azimuthal direction. This means that in the presence of dust the viscous evolution is slower, and the orbital motion is closer to the keplerian speed.
The coefficient B acts as a "pushing" factor, that in the radial direction the dust tries to push the gas in the direction opposite to the pressure gradient, with a speed of $2Bv_P$. This is a result of the exchange of angular momentum between the gas and dust. In Section 1.3 we saw that the dust drifts towards the pressure maximum because it losses angular momentum due to the drag force of the gas. Considering the back-reaction effects, the gas must gain this angular momentum and move away from the pressure maximum.
The advantage of using the back-reaction coefficients, is that all the information of the dust size distribution is contained in here, separated from the actual velocity terms. These coefficients can be calculated according to the model and easily implemented into a code to include the back-reaction effects.

2.2.1 Single size approximation

To extend our interpretation of the back-reaction coefficients, we will now study the limit case with a single dust species mixed with the gas, with a dust-to-gas ratio ϵ and Stokes

number St.
In this case the back-reaction coefficients become:

$$A_{\text{single}} = \frac{\epsilon + 1 + \text{St}^2}{(\epsilon + 1)^2 + \text{St}^2}, \tag{2.13}$$

$$B_{\text{single}} = \frac{\epsilon \text{St}}{(\epsilon + 1)^2 + \text{St}^2}, \tag{2.14}$$

which can then be further approximated in the limit of small particles ($\text{St} \ll 1$) by:

$$A_{\text{single}} \approx \frac{1}{\epsilon + 1}, \tag{2.15}$$

$$B_{\text{single}} \approx \frac{\epsilon \text{St}}{(\epsilon + 1)^2}. \tag{2.16}$$

From here we notice that the damping coefficient is approximately a correction for the additional dust mass that the gas has to carry, and that pushing coefficient is proportional to the particle size and the dust-to-gas ratio.
Other approach to obtain the back-reaction coefficients is to assume a distribution for which the X and Y sums have an analytical solution, such as the MRN power law distribution for ISM grains (Mathis et al., 1977), as shown in Garaud (2007); Kretke et al. (2009).
A simpler approximation however, it is obtain a representative particle size using the mass weighted averaged Stokes number of the dust size distribution, and use this to compute the back-reaction coefficients, as given by the single size approximation in Equation 2.13 and 2.14.

2.2.2 Correction for the dust diffusivity

From the back-reaction effects on the gas dynamics, we can infer that the dust damps the diffusivity of the gas by a factor of approximately $\sim (\epsilon+1)^{-1}$, which accounts for the extra mass.
We can correct the dust diffusive term of Equation 1.16 by replacing the dust diffusivity with:

$$D_{\text{d}} = \frac{\nu}{(\epsilon + 1)\,(\text{St}^2 + 1)}. \tag{2.17}$$

2.3 Accounting for the vertical structure

In Section 1.5 we described that the dust settles towards the midplane in comparison with the gas, resulting in a higher dust-to-gas ratio at lower heights.
This means that the back-reaction perturbations are stronger near the midplane than in the surface layers Kanagawa et al. (2017); Dipierro et al. (2018).

To account for the gas and dust vertical distribution, we must derive the radial velocity of both components from the net mass flux:

$$\Sigma_{\rm g}\bar{v}_{{\rm g},r} = \int_{-\infty}^{+\infty} \rho_{\rm g}(z)\, v_{{\rm g},r}(z)\, {\rm d}z, \tag{2.18}$$

$$\Sigma_{\rm d}(m)\bar{v}_{{\rm d},r}(m) = \int_{-\infty}^{+\infty} \rho_{\rm d}(z,m)\, v_{{\rm d},r}(z,m)\, {\rm d}z. \tag{2.19}$$

The volume densities of the gas and dust are defined by the gaussian profiles given in Equation 1.31 and 1.32. Notice that the argument of the integral in Equation 2.19 is weighted more heavily around the midplane for the larger particles than for smaller ones. Also, notice that small particles and the gas component present a similar vertical weight, since they have similar vertical structures.
We model the gas velocity at every height:

$$v_{{\rm g},r}(z) = A(z)v_\nu + 2B(z)v_P, \tag{2.20}$$

where the back-reaction coefficients are now a function of the dust distribution at every height, with the local dust-to-gas ratio defined as $\epsilon_m(z) = \rho_{\rm d}(m,z)/\rho_{\rm g}(z)$.
Using this expression we can rewrite Equation 2.18 as:

$$\bar{v}_{{\rm g},r} = \frac{1}{\Sigma_{\rm g}} \int_{-\infty}^{+\infty} \rho_{\rm g}(z)\ \left(A(z)\, v_\nu + 2B(z)\, v_P\right)\, {\rm d}z = \bar{A}\, v_\nu + 2\bar{B}\, v_P, \tag{2.21}$$

following (Gárate et al., 2020). Now the information about the vertical distribution of gas and dust is included in the coefficients $\bar{A}$ and $\bar{B}$, which are the mass weighted and vertically averaged back-reaction coefficients.
This process can be repeated for the dust mass flux in order to obtain the dust velocity while accounting for the vertical structure.
A more rigorous approach would be to also include the vertical structure of the viscous and pressure velocity as described in Kanagawa et al. (2017); Dipierro et al. (2018), however in our work we showed that the net flux does not change by considering this step (Gárate et al., 2020).
For reference, the viscous and pressure velocities can be modeled as:

$$v_\nu(z) = \frac{\nu}{2r}\left(6p + q - 3 + (5q-9)\left(\frac{z}{h_{\rm g}}\right)^2\right), \tag{2.22}$$

$$v_P(z) = v_K\left(\frac{h_{\rm g}}{r}\right)^2\left(p + \frac{q+3}{2} + \frac{q-3}{2}\left(\frac{z}{h_{\rm g}}\right)^2\right), \tag{2.23}$$

following the Takeuchi & Lin (2002); Dipierro et al. (2018) model, with p and q the exponents of the gas surface density and temperature profiles respectively.

2.4 Relevance of dust back-reaction

2.4.1 An analytical back-reaction condition

We now have the ingredients to assess how important is the back-reaction for the collective disk evolution.
As in Dipierro et al. (2018); Gárate et al. (2020), we notice that the viscous and pressure velocity can be rewritten as:

$$v_\nu = -3\alpha_\nu \frac{c_s^2}{v_K}\gamma_\nu, \tag{2.24}$$

$$v_P = -\frac{1}{2}\frac{c_s^2}{v_K}\gamma_P, \tag{2.25}$$

with $\gamma_\nu = \mathrm{dln}(\nu\,\Sigma_\mathrm{g}\sqrt{r})/\mathrm{dln}\,r$ and $\gamma_P = \mathrm{dln}P/\mathrm{dln}\,r$ the power law exponents, which are on the order of the unity in a smooth disk.
To first order, the back-reaction is locally important for the gas dynamics if the pushing term is comparable to the viscous term in the radial velocity ($|2Bv_P| \gtrsim |Av_\nu|$, Equation 2.3). Using the single size approximation for the back-reaction coefficients, and the rewritten expressions for the viscous and pressure velocities (Equation 2.15, 2.16, 2.24, and 2.25) we rewrite this condition as:

$$\frac{\mathrm{St}\,\epsilon}{\alpha} \gtrsim 1. \tag{2.26}$$

As would be expected, the most important parameters to determine the importance of the dust back-reaction are the Stokes number, the dust-to-gas ratio, and the turbulent viscosity.

2.4.2 Parameter space tests

To study the effect of the dust back-reaction on the disk velocity profiles, we construct a simple disk model in steady state with:

$$\Sigma_\mathrm{g}(r) = 1000\,\mathrm{g\,cm^{-2}}\left(\frac{r}{1\,\mathrm{AU}}\right)^{-1}, \tag{2.27}$$

$$T(r) = 300\,\mathrm{K}\left(\frac{r}{1\,\mathrm{AU}}\right)^{-1/2}. \tag{2.28}$$

We assume a mean molecular weight of $\mu = 2.3$ for the gas. For the dust growth we assume that the particle size corresponds to the minimum between the fragmentation and drift limits (Equation 1.28, 1.30), therefore we have a single particle size at each radius.
Now we show the velocity profile for different dust-to-gas ratios, turbulence, and fragmentation velocity values. A detailed comparison between the gas velocity with back-reaction and the viscous velocity for static disk model can also be found in Dipierro et al. (2018).
For now we calculate only a static solution with our toy model. In Chapter 3 we show the

effects of dust back-reaction on disk evolution, including gas and dust advection, multiple dust species and coagulation.

Fiducial Model

Parameter	Value
ϵ	0.01
α	10^{-3}
$v_{\rm frag}$	$1000\,{\rm cm\,s^{-1}}$

Table 2.1: Fiducial parameters for the analytical model.

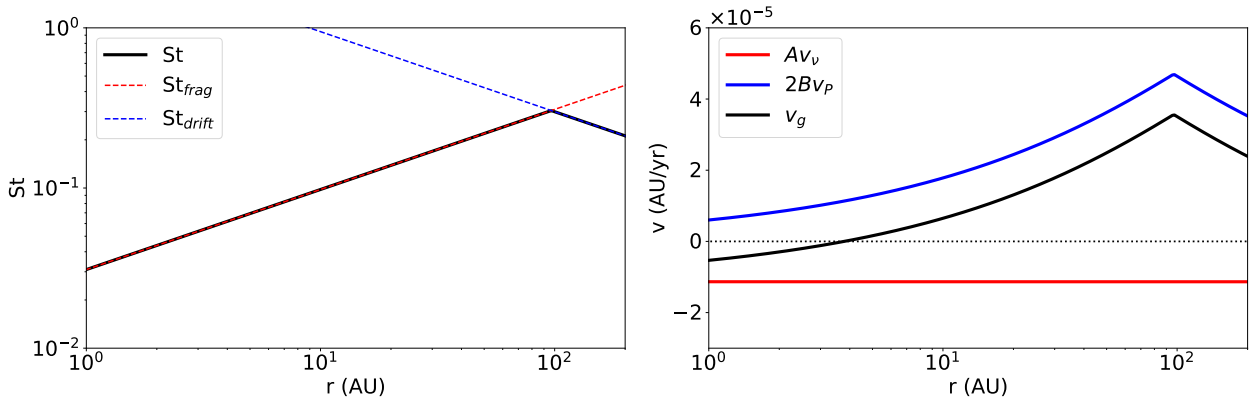

Figure 2.1: *Left*: Stokes number profile for the fiducial analytical model (black). The fragmentation and drift limits are marked with red and blue dotted lines, respectively. *Right*: Gas velocity profile for the fiducial model considering the back-reaction effect (black). The damped viscous component, and the pushing component are marked in red and blue, respectively.

For our fiducial model we use the parameters of Table 2.1. Figure 2.1 shows the Stokes number profile for our analytical disk model, in which the particle growth at inner regions (inside 100 AU) is limited by fragmentation, while at the outer regions is limited by drift. The gas velocity profile shows that, as the Stokes number increases, the back-reaction push becomes dominant for larger radii. Due to the back-reaction effect, the gas accretion is reversed beyond 3 AU, where the term $2Bv_P > Av_\nu$. These results indicate that even in a smooth disk (which under viscous evolution would flow inward), the back-reaction push can cause it to flow outwards if the particle sizes are large enough. From the velocity profile we can expect the gas accretion onto the star to decrease, as the dust flow pushes the gas outwards.
We must notice however, that the back-reaction effects will stop as soon as the dust reservoir

is depleted. In other words, the back-reaction perturbation are more likely to be effective during early stages of disk evolution, while the dust content is high. After the dust drifts towards the star, the gas should retake the standard viscous evolution (Gárate et al., 2020), if we do not consider the influence of dust traps. In Section 3.2 we will also show that the time evolution and coagulation play a major role in reducing the effect of the back-reaction.

The effect of the dust-to-gas ratio

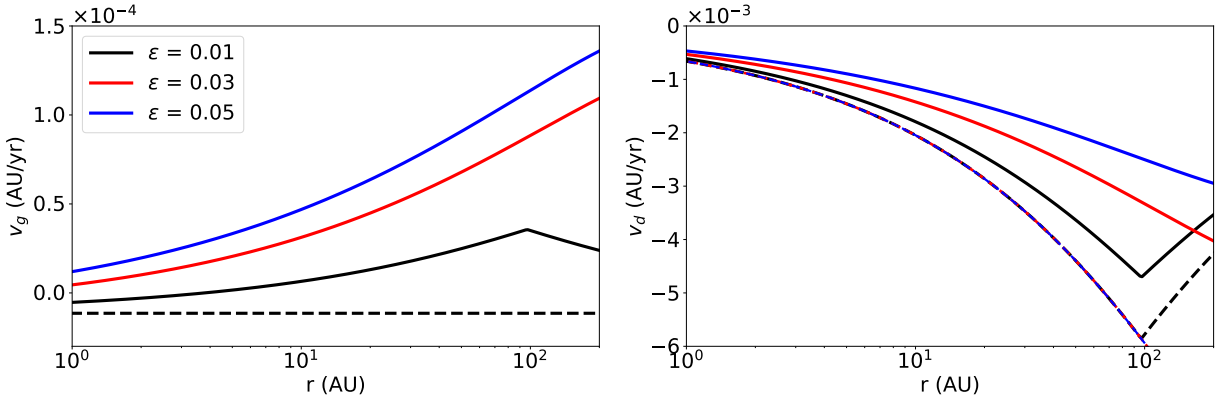

Figure 2.2: Gas (left) and dust (right) velocity profiles for disks with different dust-to-gas ratios. The solid lines show the velocity profiles considering the back-reaction effects. The dashed lines show the velocity profiles ignoring the back-reaction contribution.

The dust-to-gas ratio has two effects on the collective gas and dust dynamics. First, there is the direct dependency with the back-reaction coefficients (Equation 2.13 and 2.14), for which higher dust-to-gas ratios cause stronger damping and pushing. The second effect is to increase the growth limit by drift (Equation 1.30) which results in higher Stokes numbers, and therefore in a stronger back-reaction push.
Figure 2.2 shows that for dust-to-gas ratios higher by a factor of a few to that of the ISM, the back-reaction push can cause the disk to flow outward even in the regions around 1 AU. The dust flow is not reversed, but it is slowed down by a factor of a few across the whole disk. This is sometimes called "collective drift" in the literature (Drążkowska & Alibert, 2017), and refers to how a group of particles drift slower than a single grain.

The effect of turbulence

The turbulence affects both the viscous velocity, and the growth limit by fragmentation. For a high turbulence value of $\alpha = 10^{-2}$, we have that the viscous velocity is stronger by an order of magnitude, and the fragmentation limit (and therefore the back-reaction pushing term) is lower also by an order of magnitude (Equation 1.6, 1.28, 2.14). This results in the

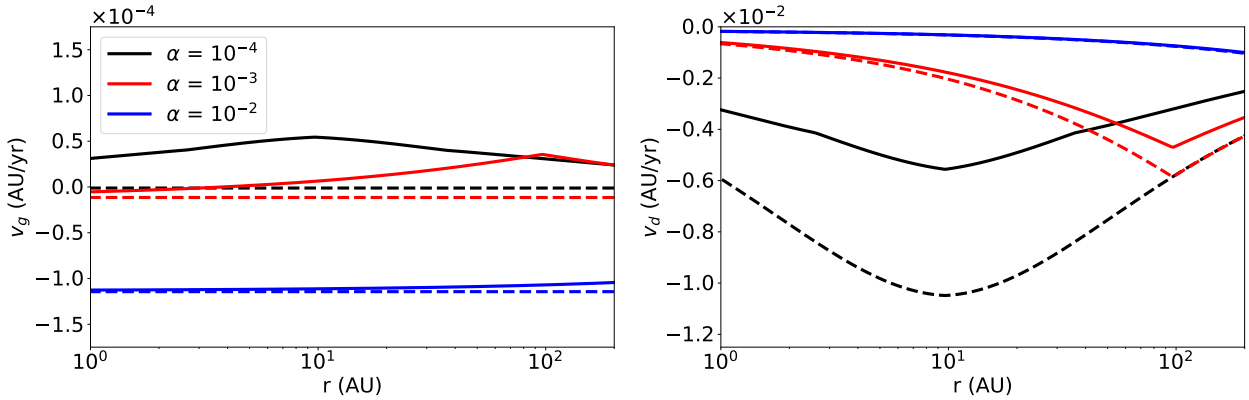

Figure 2.3: Same as Figure 2.2 for different turbulent α values.

back-reaction effect to be almost negligible for high turbulence values.
In contrast, for low turbulence values ($\alpha = 10^{-4}$) we have that the viscous accretion is practically negligible, and the pushing term is dominant. As a result the gas flow is completely reversed, while the dust accretion is slowed reduced approximately by a factor of 2 (in comparison to the case when the back-reaction is ignored).
From here we can conclude that disks that present high turbulent values (and therefore high accretion rates) are unlikely to be affected by the dust back-reaction, while disk with low turbulence could be dominated by it.

The effect of the fragmentation velocity

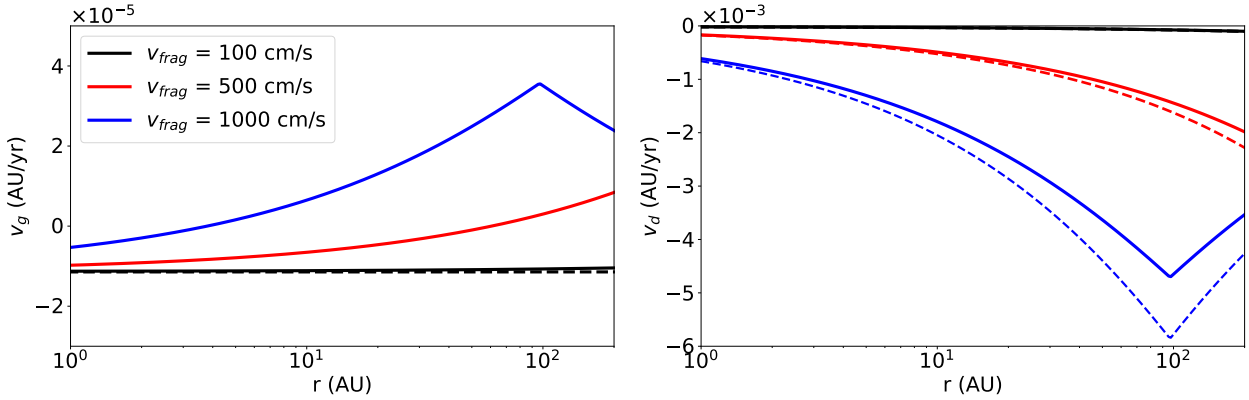

Figure 2.4: Same as Figure 2.2 for different dust fragmentation velocity values.

The fragmentation velocity affects the maximum grain size, and therefore the back-reaction pushing term. Figure 2.4 shows that for the fragmentation velocity of silicates

($v_{\mathrm{frag}} = 100\,\mathrm{cm\,s^{-1}}$) the back-reaction has almost no impact on the gas and dust velocities, since the Stokes number is of the order of 10^{-4} and 10^{-3}.
For higher fragmentation velocities of $v_{\mathrm{frag}} = 500\,\mathrm{cm\,s^{-1}}$ the back-reaction becomes comparable to the viscous velocity in the outer regions ($r \sim 100\,\mathrm{AU}$), and becomes dominant in the inner regions for values of $v_{\mathrm{frag}} = 1000\,\mathrm{cm\,s^{-1}}$.
We should consider however, that in our toy model we assumed that the dust grains grow all the way until the fragmentation and drift limits, while Birnstiel et al. (2012) showed that when solving the coagulation the particles are better represented by sizes smaller by a factor of a few. In the next chapter we solve the full coagulation and get a more accurate prediction of the back-reaction effects.

Chapter 3

Effects of Dust Back-reaction in Disk Evolution

In this chapter we present different effects of the dust back-reaction on the evolution of a protoplanetary disk, using numerical simulations to evolve gas and dust. We study the evolution of the following disks:

- A smooth self-similar disk (see Equation 1.11).
- A disk with a radial change in the fragmentation velocity, which causes a dust traffic jam (see Section 1.3, and Equation 1.28).
- A disk with a local pressure maximum, where dust accumulates (see Section 1.3).

This chapter is intended to serve as a general overview of the dust back-reaction effects, and as motivation for more complex models where the back-reaction might play an important role (see Gárate et al., 2019, 2020, and Chapter 4, 5, and 6).

3.1 General setup in DustPy

We use the code `DustPy` (Stammler & Birnstiel, in prep.), which solves the gas and dust transport in the radial direction following Equation 1.1 and 1.16, along with the Smoluchowski coagulation equation for multiple dust species, as in Birnstiel et al. (2010).
We include the dust back-reaction by modifying the gas and dust velocities using the back-reaction coefficients, as described in Section 2.1, 2.2 and 2.3.
We use the parameters described in Table 3.1 for our numerical setup.
Notice that here we distinguish between the turbulent viscosity α_ν, which affects the gas global viscous evolution, and the dust turbulence α_t, which affects the small scale dust dynamics, such as fragmentation, diffusion, and settling.
We use an initial dust-to-gas ratio of $\varepsilon_0 = 0.03$ as fiducial value, and but also compare the time evolution of the accretion rate to disks with other initial dust-to-gas ratios. We pick a higher dust-to-gas ratio than the canonical $\varepsilon_0 = 0.01$ of the ISM, as otherwise the

back-reaction effects are unnoticeable without including several dust trapping mechanism at the same time.
The simulation grid is set according to Table 3.2.

Parameter	Value	Description
M_*	$1\,M_\odot$	Stellar mass
Σ_0	1000 g cm^{-2}	Surface density at r_0
T_0	300 K	Temperature at r_0
r_0	1 AU	Normalization radius
α_ν	10^{-3}	turbulent viscosity
α_t	10^{-3}	Dust turbulence
v_{frag}	$1000\,\text{cm}\,\text{s}^{-1}$	Fragmentation velocity
μ	2.3	Gas mean molecular weight
a_0	1 μm	Dust initial size
ρ_s	1.6 g cm^{-3}	Dust material density
ε_0	0.03	Initial dust-to-gas ratio

Table 3.1: Fiducial parameters for the numerical model.

Parameter	Value	Description
n_r	250	Number of radial grid cells
n_m	120	Number of mass grid cells
r_{in}	5 AU	Radial inner boundary
r_{out}	300 AU	Radial outer boundary
m_{min}	10^{-12} g	Dust mass lower limit
m_{max}	10^5 g	Dust mass upper limit

Table 3.2: Grid parameters for the numerical model.

3.2 Slowing viscous evolution

In this section we study the effects of dust back-reaction on the evolution of a disk following the Lynden-Bell & Pringle (1974) self-similar profile (Equation 1.11), using a cut-off radius of 100 AU, and an initial dust-to-gas ratio of $\varepsilon_0 = 0.03$.
From Figure 3.1 we see that the back-reaction has little effect on the global disk evolution over the first 0.15 Myrs. The only appreciable difference from the surface density profiles is that the dust-to-gas ratio is slightly higher in the inner regions when the back-reaction is considered, but the increment is basically negligible.
From Figure 3.2 we see that the particles have a Stokes number of St $\sim 10^{-2}$. Since the dust-to-gas ratio is also of the order of $\epsilon \sim 10^{-2}$, we have that the disk evolution should still be mostly viscous dominated, since $\alpha \gtrsim \text{St}\epsilon$ (see Equation 2.26).

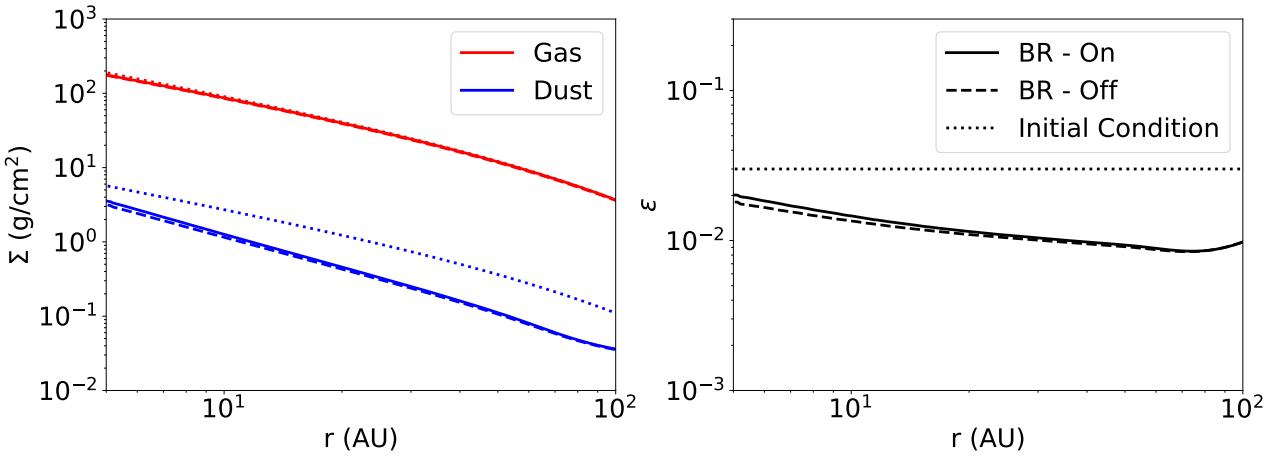

Figure 3.1: *Left:* Surface density of gas (red) and dust (blue) for a disk with a self-similar profile, at 0.15 Myrs, considering the back-reaction effects (solid lines) and ignoring them (dashed lines). The difference between both is only a factor of a few percents. *Right:* Dust-to-gas ratio profiles. The initial condition is plotted in dotted lines for comparison.

The effect of the back-reaction on the disk dynamics is more evident by looking at the stellocentric accretion rate, and the gas radial velocity profile (see Figure 3.3). During the first 0.1 Myrs of the disk evolution (for the fiducial simulation with initial dust-to-gas ratio $\varepsilon_0 = 0.03$), the dust reaches its maximum size by sticking, and is able to reverse the gas accretion during this phase. Without the dust back-reaction, the gas accretion rate should be approximately $\dot{M}_g \approx 5.0 \times 10^{-8}\,M_\odot/\mathrm{yr}$, instead, when the back-reaction is considered the flux is reversed to $\dot{M}_g \approx -1.0 \times 10^{-9}\,M_\odot/\mathrm{yr}$.

After a small fraction of the dust drifts inward following the pressure gradient the back-reaction effects decrease and the regular viscous accretion is resumed. For our disk model the back-reaction effects become negligible after 0.4 Myrs. From the velocity profiles we notice that in the inner regions the back-reaction push opposes the viscous accretion (which points inward), while in the outer regions the back-reaction push enhances the outward viscous spreading. We find that at $r \approx 100$ AU the back-reaction push is comparable to the viscous spreading velocity, however we find unlikely that this contribution will affect the overall disk size, as the viscous speed grows faster with radii than the back-reaction push, and also because the latter will decrease within a drift timescale.

Our results agree with the reduced the net mass accretion described in Kanagawa et al. (2017), though their results show a stronger back-reaction effect, since the fragmentation barrier was not considered. We do not find the self-induced dust traps in the outer disk described by Gonzalez et al. (2017).

From this simulation we learn that the back-reaction by itself cannot perturb the global disk evolution, as the dust is quickly depleted by radial drift, and other mechanisms to collect dust should be present in order to affect the gas and dust distributions.

We find that the net effect of the back-reaction is less efficient when considering multiple

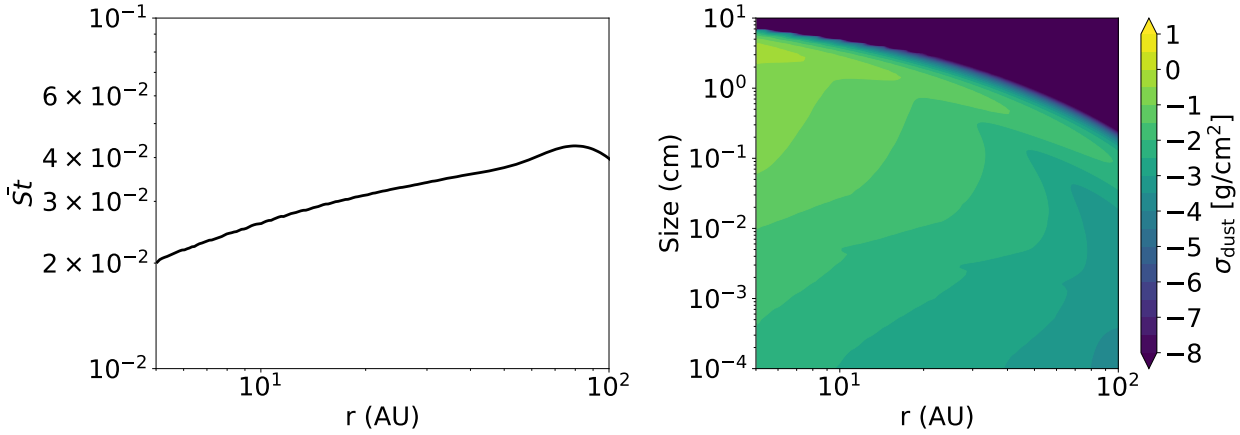

Figure 3.2: *Left:* Mass weighted stokes number profile for a disk with a self-similar profile. *Right:* Dust surface density distribution. Both plots are taken at 0.15 Myr, when dust is still abundant in the disk, for the simulation when the back-reaction is considered.

species and solving the coagulation equation, than for the toy model presented in Section 2.4, both due to the difference between the maximum particle size calculated with the simple growth limits (see Equation 1.30 and 1.28) and the real representative size showed in Figure 3.2, and also due to the time evolution of the dust density distribution.
However, we can infer that accretion events might be heavily influenced by the back-reaction, as this can lead to a reduced, or even reversed gas flow.
This experiment served as motivation to study the back-reaction effects on the accretion of gas and dust of RW Aur (Günther et al., 2018), where the high dust content might slow down the gas accretion rate in the event of a dead zone reactivation (see Chapter 4 and Gárate et al., 2019).

3.3 Dust accumulation at traffic jams

In this section we study the back-reaction effects in the case of a disk with a traffic jam. We set up our disk as described in Section 3.1. For the initial conditions we assume that the surface density follows a power law profile, and is in viscous steady state as described in Section 1.1.1 and Equation 1.9.
To create the traffic jam we consider a disk that presents a change in the fragmentation velocity of the dust particles at a certain radius, such that:

$$v_{\text{frag}} = \begin{cases} 1000\,\text{cm}\,\text{s}^{-1} & r \geq 20\,\text{AU} \\ 100\,\text{cm}\,\text{s}^{-1} & r < 20\,\text{AU} \end{cases} \tag{3.1}$$

As described in Section 1.3 and in Birnstiel et al. (2010), a change in the fragmentation velocity (as in Equation 3.1) is expected to increase the concentration of small dust grains

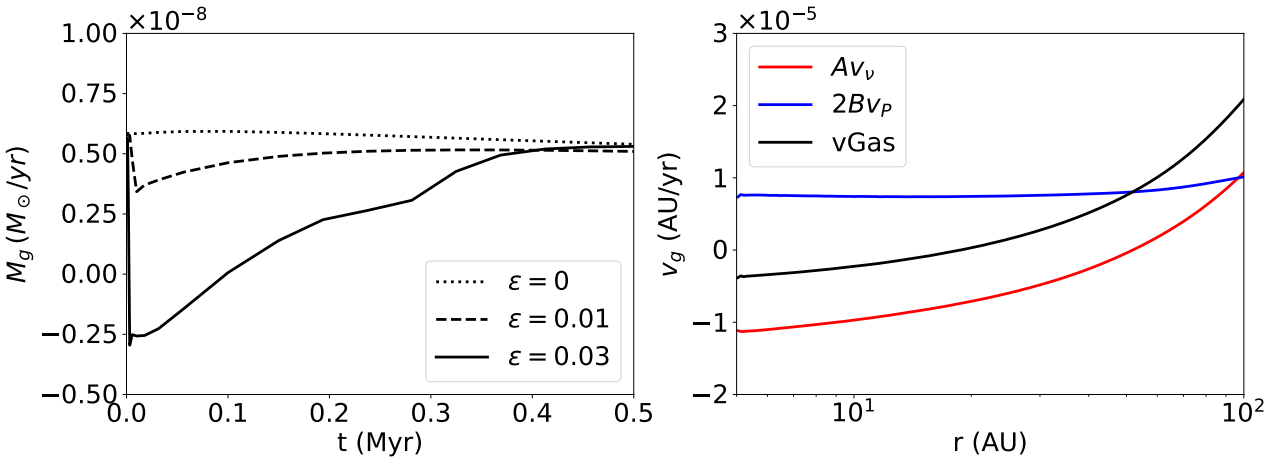

Figure 3.3: *Left:* Accretion rate evolution (measured at 10 AU for different initial dust-to-gas ratios, for a disk with a self-similar profile. *Right:* Gas velocity profile (black) at 0.15 Myrs, considering the back-reaction effects. The red and blue lines show respectively the damped accretion, and the pushing components.

in the inner regions, since the particles in the outer disk grow to larger sizes and drift faster than the particles in the inner disk.

Figure 3.4 shows that at the fragmentation velocity transition the dust effectively accumulates towards the inner regions. After 0.36 Myr, the inner boundary ($r_{in} = 5$ AU) presents a dust-to-gas ratio between $\epsilon = 0.1$ and $\epsilon = 0.2$. At the transition ($r = 20$ AU) the dust-to-gas ratio reaches values of $\epsilon = 0.45$ when the back-reaction is ignored, and $\epsilon = 0.75$ when the back-reaction is considered. After this point the outer disk has exhausted the dust supply, and the back-reaction effects will slowly decay with time(see more on Gárate et al., 2020).

The gas surface density in the inner regions is also reduced to a $\sim 75\%$ of its initial value. This occurs of the radial variation of the back-reaction pushing term, due to the radial dependency of the particle size. From Figure 3.5 we see that the particles in the inner regions grow to smaller sizes (St $\sim 10^{-4}$, meaning that the back-reaction push is weak), while in the outer disk the particles grow to larger sizes (St $\sim 10^{-2}$), where the back-reaction push can slow down the gas flow. This causes the inner disk to get slowly depleted as the dust particles accumulate. The effect is smoothed down once the dust has moved from the outer regions to the inner regions, and the back-reaction push should vanish once the dust supply is exhausted.

In terms of the accretion rate we see how the back-reaction reduces the accretion flow into the star (Figure 3.6). Without the dust back-reaction the disk should remain in steady state, however due to the decrease in the gas density, and the damping due to the accumulation of dust in the inner regions, the accretion rate is reduced to a $\sim 66\%$ of its initial value, for an initial dust-to-gas ratio of $\varepsilon_0 = 0.03$, and to a $\sim 33\%$ of its initial value for an initial dust-to-gas ratio of $\varepsilon_0 = 0.05$.

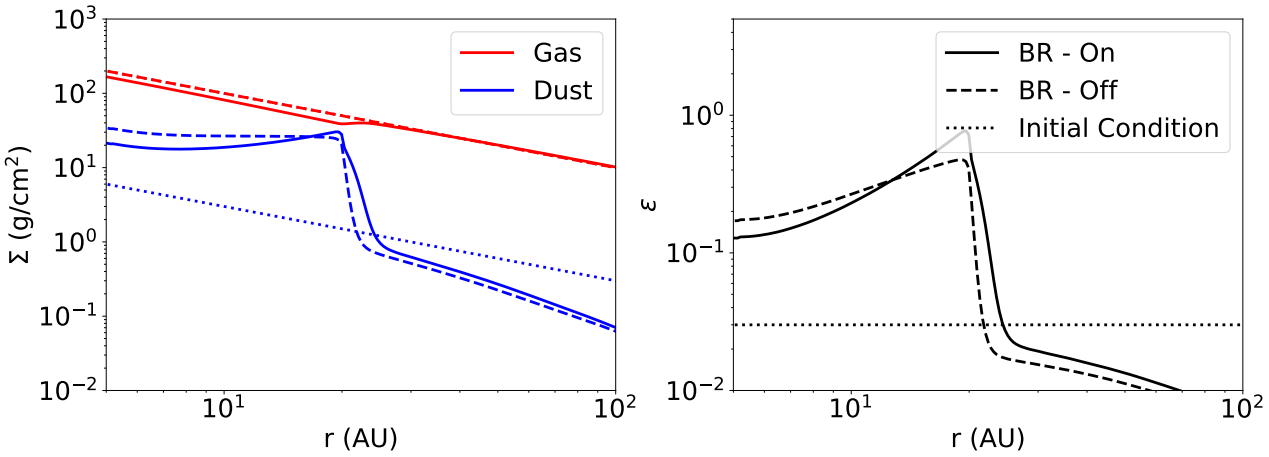

Figure 3.4: Same as Figure 3.1, for the simulation with a traffic jam, at 0.36 Myr

Because the traffic jam and the associated back-reaction effects depend on the change in the fragmentation velocity, we expect a similar outcome at the disk icelines (Vericel & Gonzalez, 2020), where the composition of the dust grains change due to the sublimation and recondensation of volatiles.
Drążkowska & Alibert (2017) and Schoonenberg & Ormel (2017) showed that due to water vapor diffusion, the dust-to-gas ratio can also be further enhanced at the outer edge of the water snowline, where particles are large. The dust back-reaction could further increase this effect and provide ideal conditions for the formation of planetesimals. This idea was further explored in Chapter 5 and Gárate et al. (2020) , where we characterized the back-reaction effects at the water snowline.

3.4 Spreading of a dust ring

In this section we study the effect of the dust back-reaction in a disk with a dust trap. As mentioned in Section 1.3, a dust trap can be any region with a local pressure maximum, where the drift speed of large particles becomes zero (Equation 1.23, assuming that the gas speed is low enough to allow for the particles to accumulate).
To create a pressure maximum in the disk, we consider that the turbulent viscosity α_ν is not uniform, and that the disk is in viscous steady state following Equation 1.9, such that:

$$\Sigma_g = \Sigma_0 \left(\frac{r}{r_0}\right)^{-1} \frac{\alpha_{\nu,0}}{\alpha_\nu(r)}, \tag{3.2}$$

where $\alpha_{\nu,0} = 10^{-3}$, and $\alpha_\nu(r)$ corresponds to a variable turbulent viscosity profile. For the temperature profile we assume a simple power law profile with exponent $q = 0.5$.
We want to study the cases of a dust ring formed by the presence of a gap and a bump in

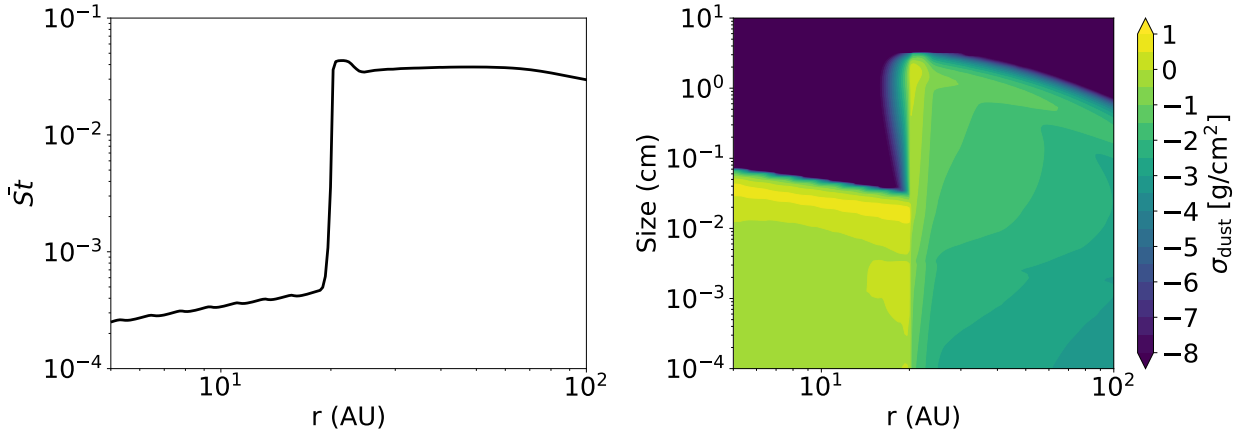

Figure 3.5: Same as Figure 3.2, for the simulation with a traffic jam, at 0.36 Myr.

the gas surface density, since both cases form a pressure maximum in the disk. To form a gap in the gas surface density we use the following α_ν profile:

$$\alpha_{\nu,\mathrm{gap}}(r) = \alpha_{\nu,0} \times \left(1 + A_\nu \exp\left(-\frac{1}{2}\left(\frac{r - r_\nu}{w_\nu}\right)^2\right)\right), \tag{3.3}$$

where r_ν, A_ν, and w_ν are respectively the location, the amplitude, and the standard deviation of the gaussian factor.
Similarly, to create a bump in the gas surface density, we use the following α_ν profile.

$$\alpha_{\nu,\mathrm{bump}}(r) = \alpha_{\nu,0} \times \left(1 + (1 - A_\nu) \exp\left(-\frac{1}{2}\left(\frac{r - r_\nu}{w_\nu}\right)^2\right)\right). \tag{3.4}$$

For both the gap and the bump we set the location to $r_\nu = 20\,\mathrm{AU}$, the amplitude to $A_\nu = 0.5$, and the width to $w_\nu = 1.5\,\mathrm{AU}$.
Figure 3.7 shows the surface densities, dust-to-gas ratio, and gas velocity profiles for both setups, and Figure 3.9 shows the dust size distribution for the case when the back-reaction is considered.
For the "local gap" simulation, the dust ring is formed at the outer edge of the gap (at $r = 22\,\mathrm{AU}$, where the pressure maximum is located), while for the "local bump" simulation the dust ring is at $r_\nu = 20\,\mathrm{AU}$, right at the center of the bump.
Because the pressure maximum location and the steepness of the pressure gradient differs between the two scenarios, we can the properties of the dust trap do be quantitatively different, as well as the back-reaction effects.
The most evident effect of the back-reaction is that the dust ring is spread over a wider radii, and the maximum dust-to-gas ratio is lower. For the "local gap" simulation the maximum dust-to-gas ratio decreases from $\epsilon = 0.35$ to $\epsilon = 0.20$ when the back-reaction

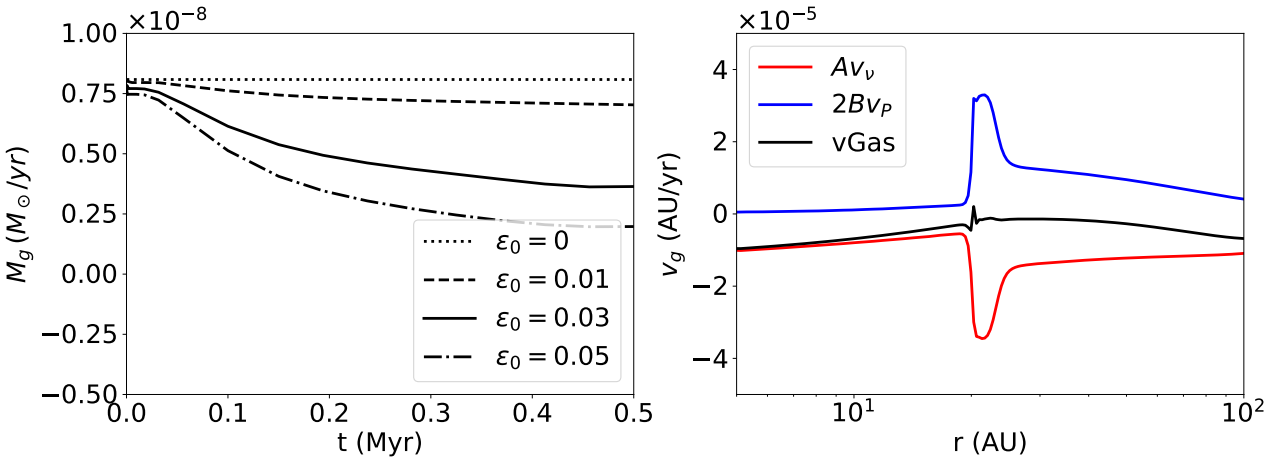

Figure 3.6: Same as Figure 3.3, for the simulation with a traffic jam, at 0.36 Myr

is considered. Similarly, for the "local bump" simulation the dust-to-gas ratio at the trap decreases from $\epsilon = 1.0$ to $\epsilon = 0.35$.

The decrease in the dust-to-gas ratio is caused by the back-reaction effect on the gap profile (see Figure 3.8 for a zoom in of the gas surface density profiles). Because the back-reaction push on he gas points in the opposite direction of the pressure gradient, the gas is spread over a wider radii, which then results in a less efficient dust trap.

For the "local gap" simulation, this causes the location of the dust ring to shift by approximately 0.5 AU. For the "local bump" simulation, the smoothing of the pressure bump allows the dust to keep flowing towards the inner regions (notice that when the back-reaction is ignored, the regions inside r_ν become comparatively dust depleted.

Finally, a common effect of the back-reaction, is to smooth out the gas velocity profile, as the viscous component (Av_ν) and the pushing component ($2Bv_P$) cancel each other, forcing the gas into a new steady state. This last part depends however on the parameters used, and for lower fragmentation velocities or higher alpha values the viscous flow would remain dominant.

Our results agree with the simulations of Kanagawa et al. (2018) that showed that the dust back-reaction can spread a dust ring, however the effect is not as evident when the growth limits are considered. Similarly, our results agree with Onishi & Sekiya (2017), who showed that the back-reaction is not strong enough to completely disrupt the pressure bump that formed the dust trap in the first place.

The results of this section indicate that we should consider the back-reaction effects when modeling dust rings in protoplanetary disks. In a disk with a gap opening planet, or in a disk with a photo-evaporative gap, where the dust concentrates at the gap outer edge, we could use our knowledge of the dust dynamics to improve our estimations of the disk properties, as done in Dullemond et al. (2018) for disks of the DSHARP sample (Andrews et al., 2018), where the ring width was used to estimate the gas turbulence.

We explore these two scenarios and show our preliminary results in Chapter 6.

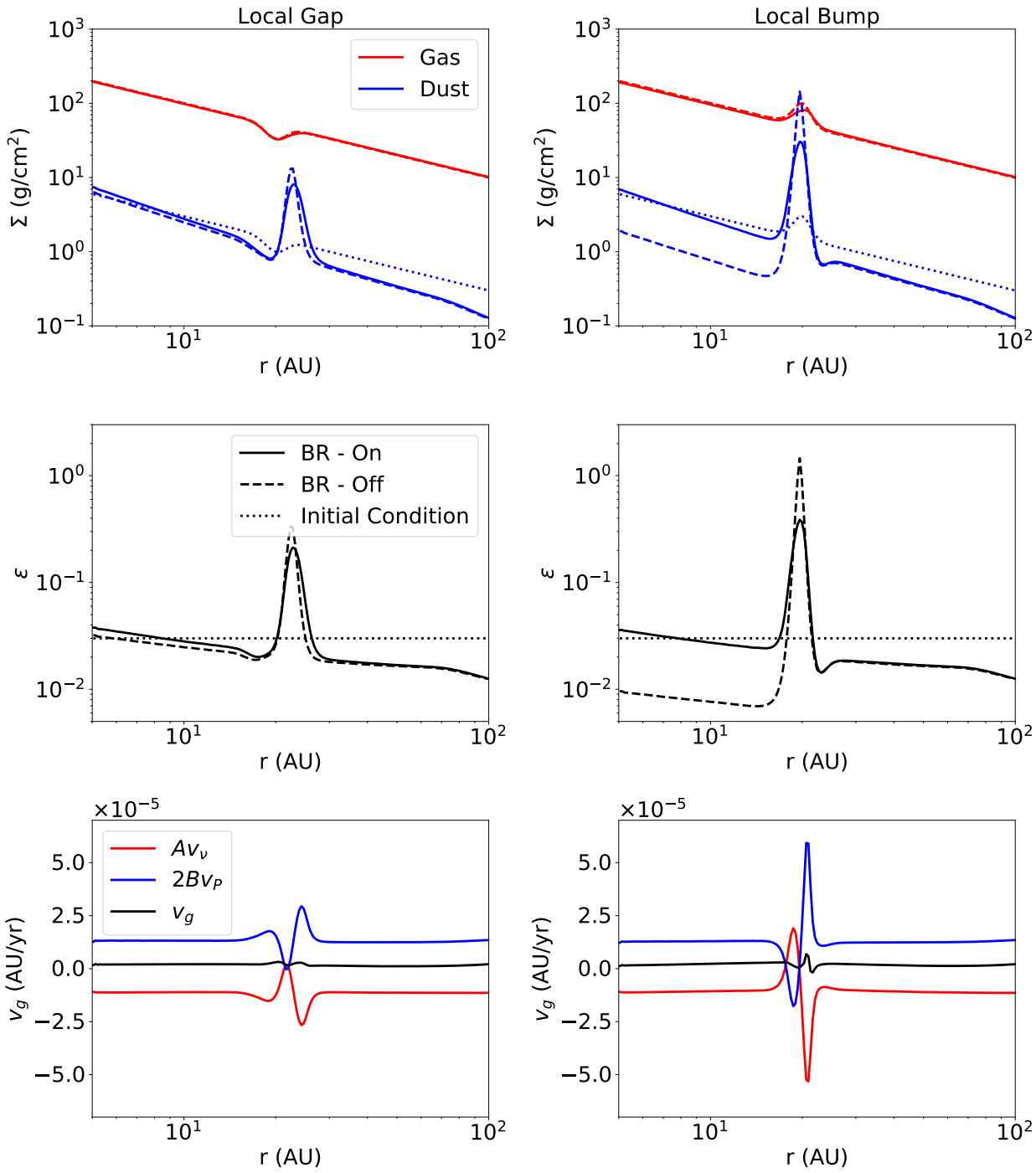

Figure 3.7: Surface density profiles (*top panel*), dust-to-gas ratio profiles (*middle panel*), and gas velocity profiles along with the back-reaction components (*bottom panel*), for the simulation with a dust ring formed by a density gap (*left column*), and by a density bump (*right column*). The profiles are taken at 0.15 Myr.

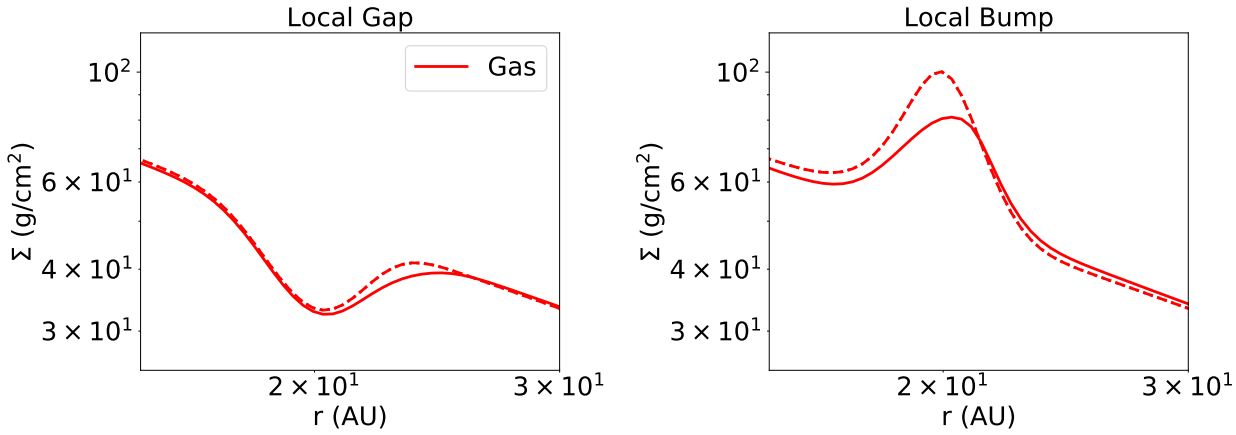

Figure 3.8: Zoom in of the gas surface density profiles in Figure 3.7 top panel. The solid line shows the profiles considering the back-reaction effects, while the dashed lines ignore it.

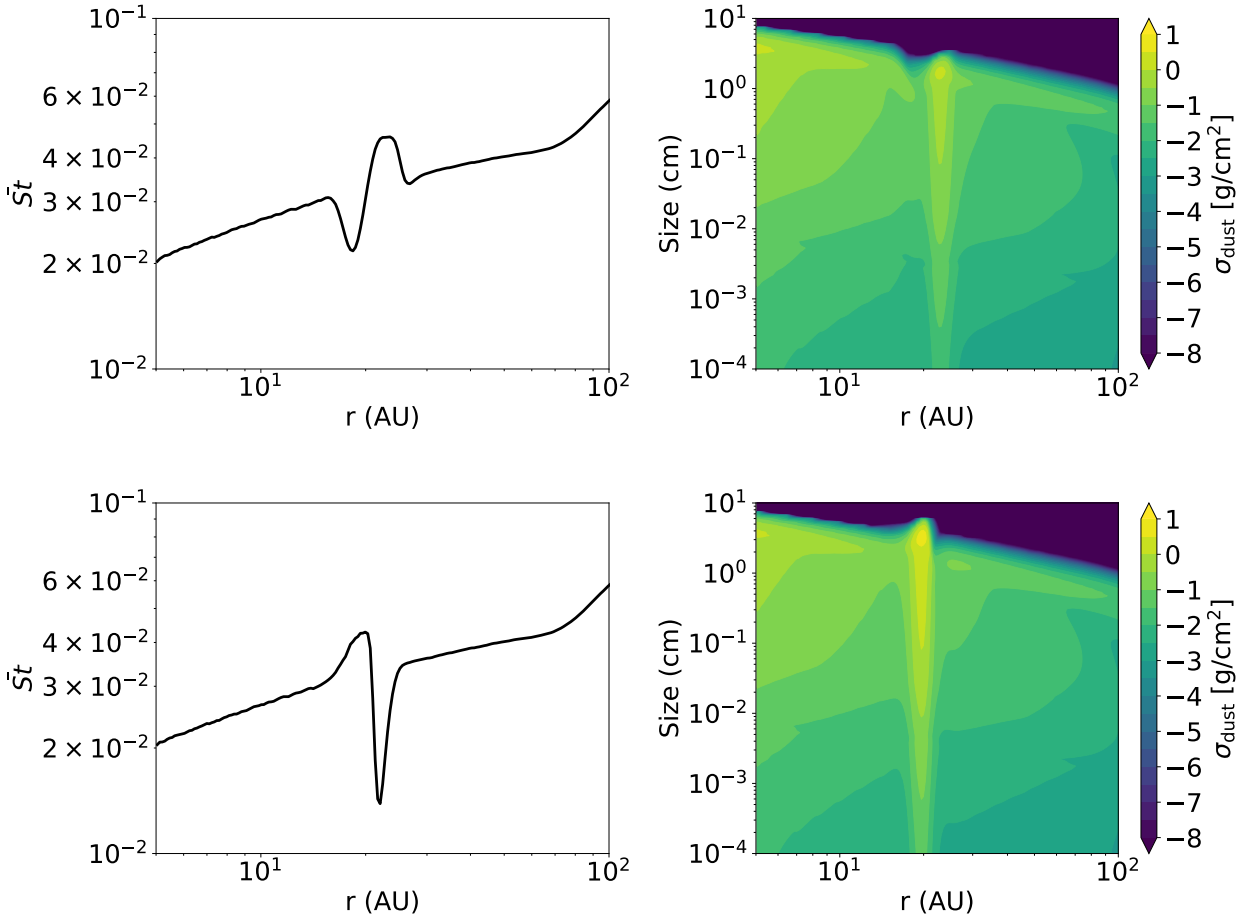

Figure 3.9: Mass weigthed stokes number profile (*left column*), and dust size distribution (*right column*) for the simulation with a dust ring formed by a density gap (*top panel*), and by a density bump (*bottom panel*). The profiles are taken at 0.15 Myr, for the case when the back-reaction is considered.

Chapter 4

An accretion event in RW Auriga?

The contents of this chapter where published in the Astrophysical Journal.
Credit: The Dimming of RW Auriga: Is Dust Accretion Preceding an Outburst?, Gárate et al., ApJ, 871, 53, 2019.

4.1 Introduction

RW Aur A is a young star that in the last decade presented unusual variations in its luminosity. The star has about a solar mass, it is part of a binary system, and is surrounded by a protoplanetary disk showing signatures of tidal interaction (Cabrit et al., 2006; Rodriguez et al., 2018). The star had an almost constant luminosity for around a century, interrupted only by a few short and isolated dimmings (see Berdnikov et al. (2017) for a historical summary) until 2010, when its brightness suddenly dropped by 2 mag in the V band for 6 months (Rodriguez et al., 2013). Since 2010, a total of five dimming events have been recorded (see Rodriguez et al., 2013, 2016; Petrov et al., 2015; Lamzin et al., 2017; Berdnikov et al., 2017, among others). The dimmings can last from a few months to two years, and reduce the brightness of the star up to 3 mag in the visual. Moreover, there is no obvious periodicity in their occurrence, and their origin is not yet clear (a summary of the events can be found in Rodriguez et al., 2018).

4.1.1 Observations of RW Aur Dimmings

Some observations in the recent years have shed light on the nature of RW Aur A dimmings:
During the event in 2014-2015 (Petrov et al., 2015), observations by Shenavrin et al. (2015) show a increase in IR luminosity at bands L and M. The authors infer that hot dust from the inner regions is emitting the infrared excess, while occluding the starlight and causing the dimming in the other bands.
Observations by Antipin et al. (2015); Schneider et al. (2015) found that the absorption

from optical to NIR wavelengths is gray, which could indicate the presence of large particles causing the dimming ($\gtrsim 1\,\mu$m), and measured a dust column density of $2 \times 10^{-4}\,\mathrm{g/cm^2}$, although a similar absorption may be produced if an optically thick disk of gas and small grains partially covers the star (Schneider et al., 2018).
Then, the study of RW Aur A spectra by Facchini et al. (2016) also found that the inner accretion regions of the disk are being occluded, and therefore the dimmings should come from perturbations at small radii.
Finally, during the dimming in 2016, X-Ray observations from Günther et al. (2018) indicate super-Solar Fe abundances, along with a higher column density of gas in the line of sight. The high $N_\mathrm{H}/A_\mathrm{V}$ found by the authors is interpreted as gas rich concentrations in the occluding material, or as a sign of dust growth. Also, gray absorption was found again during this event.
Given this information, several authors have discussed what mechanism would put the dust from the innermost regions of the protoplanetary disk, into the line of sight. Among the possible explanations are: a warped inner disk (Facchini et al., 2016; Bozhinova et al., 2016), stellar winds carrying the dust (Petrov et al., 2015; Shenavrin et al., 2015), planetesimal collision (Günther et al., 2018), and a puffed up inner disk rim (Facchini et al., 2016; Günther et al., 2018).
Most of the proposed mechanisms rely on having enough dust close to the star to cause the dimmings. So the focus of this study is to propose a mechanism that can deliver large amounts of dust to the inner regions of the protoplanetary disk, by raising the dust accretion rate through the release of a dust trap.
An increased dust concentration can explain some aspects of the dimmings, such as the high metallicity (Günther et al., 2018), the emission of hot dust (Shenavrin et al., 2015), and cause the dimmings provided that another mechanism transports it into the line of sight.

4.1.2 A Fast Mechanism for Dust Accretion

A sudden rise in the dust accretion can occur in the early stages of stellar evolution, when the stars are still surrounded by their protoplanetary disk composed of gas and dust. The dynamics of the gas component of the disk is governed by the viscous evolution, which drives the accretion into the star (Lynden-Bell & Pringle, 1974), and the pressure support, that produces the sub-keplerian motion. On the other hand, the dust particles are not affected by pressure forces, but suffer the drag force from the gas. This interaction extracts angular momentum from the particles and causes them to drift towards the pressure maximum, with the drift rate depending on the coupling between the dust and gas motion (Whipple, 1972; Weidenschilling, 1977; Nakagawa et al., 1986). This means that any bumps in the gas pressure act as concentration points for the dust. In these dust traps the grains accumulate, grow to larger sizes, and reach high dust-to-gas ratios (Whipple, 1972; Pinilla et al., 2012).
One of the proposed mechanisms to generate a pressure bump is through a dead zone (Gammie, 1996), a region with low turbulent viscosity (the main driver of accretion), due

to a low ionization fraction which turns off the magneto-rotational instability (Balbus & Hawley, 1991), that allows the gas to accumulate until a steady state is reached.
The presence of a dead zone would allow the dust to drift and accumulate at its inner border (Kretke et al., 2009), which can be located at the inner regions of the protoplanetary disk ($r \lesssim 1\,\mathrm{au}$). Assuming that these conditions are met, the reactivation of the dead zone turbulent viscosity through thermal, gravitational or magnetic instabilities (Martin & Lubow, 2011) would break the steady state and allow all the accumulated material (both gas and dust), to be flushed towards the star. This mechanism has been invoked already in the context of FU Ori objects to explain the variability in their accretion rate through outbursts (Audard et al., 2014).
Since the dust is drifting faster than the gas, because of hydrodynamic drag and dust diffusion, it will arrive at the inner boundary of the disk first, where it may generate the observed hot dust signatures, Fe abundances, and the dimmings if it enters into the line of sight through either a puffed up inner rim, or a stellar wind (among the explanations mentioned above). Therefore, the accretion of large amounts of dust could be actually followed by an increase in the gas accretion rate.
In this study we use 1D simulations of gas and dust, including dust coagulation and fragmentation, to model the concentration of dust at the inner edge of a dead zone. Subsequent reactivation of the turbulent viscosity lets the accumulated material rapidly drift towards the star. We measure the timescale required for the dust drifting, how much dust can be concentrated into the inner regions by this mechanism, and put it into the context of the observed features during the dimmings along with the possible explanations listed.

4.2 Model Description

For our disk model we evolve the gas and dust according to the advection equations described in Chapter 1, assuming that the disk evolves through viscous evolution, and that the dust and gas interact through the drag force. In the simulations where we consider the dust back-reaction, we do so as described in Chapter 2.
Here we present the description of our dead zone model, and its reactivation.

4.2.1 Dead Zone Model

Magneto-hydrodynamical models have predicted the presence of a region with low turbulence at the inner regions of protoplanetary disks, commonly called “Dead Zone”, caused when the ionization fraction is too low for the magneto-rotational instability (MRI) to operate (Gammie, 1996).
We parametrize the dead zone by using a variable α parameter over radius, while remaining agnostic to the underlying physics, similar to previous research (Kretke et al., 2009; Pinilla

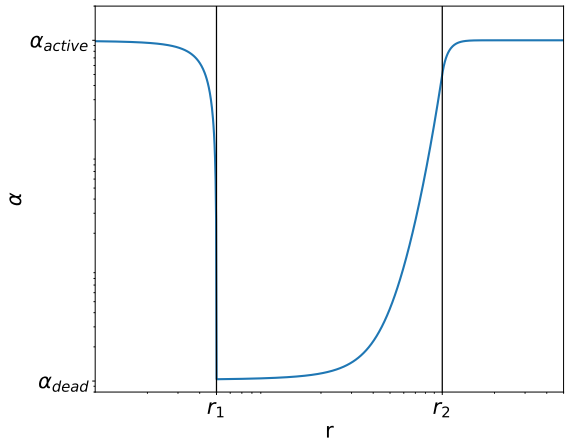

Figure 4.1: The diagram shows the shape of the α radial profile for our dead zone model (in logarithmic scale). This consists on three regions, the active inner zone limited by a sharp decay at r_1, the dead zone with a smooth rise towards its outer edge around r_2, and the outer active zone extending until the outer boundary of the simulation.

et al., 2016). Our profile is defined as:

$$\alpha(r) = \begin{cases} \alpha_{\text{active}} - \Delta\alpha \cdot e^{5(\frac{r}{r_1}-1)} & r < r_1 \\ \alpha_{\text{dead}} + \Delta\alpha \cdot \frac{1}{2} e^{10(\frac{r}{r_2}-1)} & r_1 < r < r_2 \\ \alpha_{\text{dead}} + \Delta\alpha \cdot (1 - \frac{1}{2} e^{-10(\frac{r}{r_2}-1)}) & r_2 < r, \end{cases} \tag{4.1}$$

where α_{dead} and α_{active} are the characteristic values of the α parameter inside and outside the dead zone, r_1 and r_2 are its inner and outer edges, and $\Delta\alpha = \alpha_{\text{active}} - \alpha_{\text{dead}}$. Although the dead zone shape is rather arbitrary, it was chosen to have a smoother outer border than the one of (Kretke et al., 2009), but retaining a sharp inner edge where the dust accumulates. Figure 4.1 shows a diagram of the α profile, illustrating the shape of the different intervals and its main components to guide the reader with Equation 4.1.

In order to maintain the steady state from Equation 1.9 we define the initial surface density and temperature profiles as follow:

$$\Sigma_{\text{g}}(r) = \Sigma_{\text{g},0} \left(\frac{r}{r_0}\right)^{-1} \frac{\alpha_{\text{active}}}{\alpha(r)}, \tag{4.2}$$

$$T(r) = T_0 \left(\frac{r}{r_0}\right)^{-1/2}, \tag{4.3}$$

where Σ_0 and T_0 are the values of the density and temperature at $r_0 = 1\,\text{au}$.

4.2.2 Dead Zone Reactivation

While the dead zone is present the gas will remain in steady state and the dust will accumulate at its inner boundary. Yet, different processes can reactivate the turbulence in the dead zone, allowing the accumulated material to flush towards the star. In the Gravo-Magneto instability (Martin & Lubow, 2011) for example, the gas in the dead zone becomes gravitationally unstable, raising the temperature to the point of triggering the MRI, and finally producing an accretion outburst.
In our simulations we remain agnostic about the mechanism that causes the reactivation, and only set the reactivation time t_r arbitrarily, such that:

$$\alpha(r,\, t > t_\mathrm{r}) = \alpha_\mathrm{active}. \tag{4.4}$$

4.3 Simulation Setup

In this section we describe the observational constrains relevant for RW Aur A, the free parameters of our model, and the setup of our 1D simulations using the `twopoppy` (Birnstiel et al., 2012) and `DustPy`[1] (Stammler & Birnstiel, in prep.) codes.
Our setup consists of three phases, the first phase simulates the dust accumulation at the dead zone, using a global disk simulation over long timescales ($\sim 10^5$ yr), but with a simplified and fast computational model for the dust distribution using only two representative populations. As the first phase only tracks the evolution of the surface density, in a second phase we recover the quasi-stationary particle size distribution at the inner disk ($r \leq 5$ au) by simulating the dust growth and fragmentation of multiple dust species. Finally, the third phase simulates evolution of gas and dust (including coagulation, fragmentation, and transport) in the inner disk after the dead zone is reactivated, to study the accretion of the accumulated material towards the star over short timescales, and delivering the final results.
This setup is useful to save computational time, as we are interested only in the inner disk after the dead zone reactivation, but require the conditions given by the global simulation.

4.3.1 Observational Constrains

RW Aur A is a young star with a stellar mass of $M_* = 1.4\,\mathrm{M}_\odot$ (Ghez et al., 1997; Woitas et al., 2001). The circumstellar disk has an estimated mass around $M_\mathrm{disk} \approx 4 \times 10^{-3}\,\mathrm{M}_\odot$ (Andrews & Williams, 2005), presents a high accretion rate of $\dot{M} \approx 4 \times 10^{-8} - 2 \times 10^{-7}\,\mathrm{M}_\odot/\mathrm{yr}$ (Hartigan et al., 1995; Ingleby et al., 2013; Facchini et al., 2016), and extends from a distance of ~ 0.1 au (Akeson et al., 2005; Eisner et al., 2007) until 58 au (Rodriguez et al., 2018).
For the temperature profile we use $T_0 = 250\,\mathrm{K}$, which gives similar values to the Osterloh & Beckwith (1995) profile in the inner regions of the disk for our choice of slope.

[1] DustPy is a new Python code that solves the diffusion-advection of gas and dust, and the coagulation-fragmentation of dust, based on the Birnstiel et al. (2010) algorithm.

Using these parameters, Equation 1.4 and Equation 1.9, we can constraint the values for the density and turbulence. From the disk accretion rate, mass and size we infer the value for the density $\Sigma_0 = 50\,\mathrm{g/cm^2}$ at $r_0 = 1\,\mathrm{au}$, and the turbulent viscosity $\alpha_{\mathrm{active}} = 0.1$. These parameters yield values of $\dot{M}_{\mathrm{g}} = 5 \times 10^{-8}\,\mathrm{M_\odot/yr}$ for the accretion rate, and $M_{\mathrm{disk}} = 2 \times 10^{-3}\,\mathrm{M_\odot}$ for the disk mass (without considering the accumulation excess in the dead zone). The turbulence parameter α_{active} used in our simulations is high, but necessary in order to account for the high accretion rates measured.

4.3.2 Phase 1: Dust Concentration at the Dead Zone

In the first phase of our simulations we model the accumulation of dust in a disk with a dead zone, to obtain the dust-to-gas ratio radial profile.
We use the TwoPopPy code to simulate a global protoplanetary disk with two representative populations of the dust species (details of the model can be found in Birnstiel et al., 2012). We initialize our simulations using Equation 4.1, Equation 4.2 and Equation 4.3 for the α parameter, surface gas density and temperature profiles, with the values provided by the observational constrains. For the dust-to-gas ratio we assume an uniform initial value of $\epsilon = 0.01$.
For this phase, the simulation domain goes from $r_{\mathrm{in}} = 0.01\,\mathrm{au}$ to $r_{\mathrm{out}} = 100\,\mathrm{au}$, using $n_r = 500$ radial grid cells with logarithmic spacing. In the fiducial model, the inner and outer boundaries of the dead zone are $r_1 = 0.51\,\mathrm{au}$, $r_2 = 10\,\mathrm{au}$, with a depth of $\alpha_{\mathrm{dead}} = 10^{-4}$. The simulation is evolved with this setup until the reactivation time $t_{\mathrm{r}} = 10^5$yrs. Approximately at this point the dust reaches its maximum accumulation at the inner boundary of the dead zone, which will yield the maximum dust accretion rate in the next phase. Since the gas is in steady state, we only evolve the dust in order to minimize possible numerical errors. Inside the dead zone, the gas phase is (marginally) gravitationally stable, with a Toomre parameter $Q = c_s\Omega_K/(\pi G\Sigma_{\mathrm{g}}) \gtrsim 1.5$ (Toomre, 1964). A low Q value in this region does not conflict with the model, since the gravitational instability is one of the mechanisms that can eventually reactivate the dead zone.
The initial and final states of phase 1 are shown in Figure 4.2. During this phase the dust drifts towards the dead zone inner edge reaching values of $\epsilon = 0.24$, and concentrating $110\,\mathrm{M_\oplus}$ between 0.51 - 0.6 au. Due to diffusion, the dust concentration at the innermost part of the disk also increases to values up to $\epsilon \approx 0.16$.

4.3.3 Phase 2: Dust Size Distribution at the Inner Disk

In the second phase we want to recover the dust size distribution for multiple species, based on the dust-to-gas ratio and disk conditions obtained in the previous section.
We take the outcome of the TwoPopPy simulation as the new initial conditions, and use the DustPy code to solve the dust coagulation and fragmentation (following the study of Birnstiel et al., 2010) at the inner disk, while "freezing" the simulation exactly at the reactivation time $t = t_r$, while the dead zone is still present (i.e. still using Equation 4.1). The mass grid consists of $n_m = 141$ logarithmic-spaced cells, between $m = 10^{-15} - 10^5\,\mathrm{g}$,

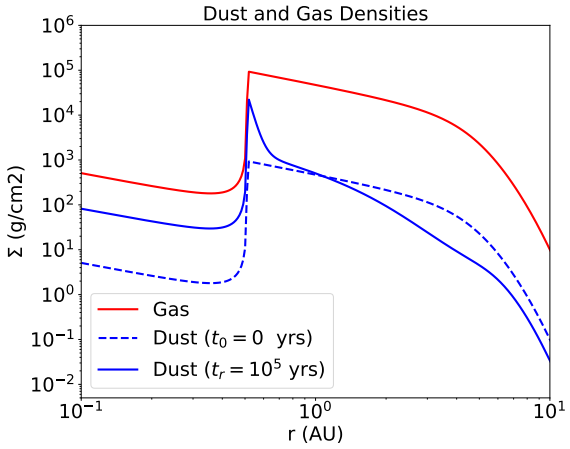

Figure 4.2: Gas and dust surface density obtained from TwoPopPy, at the beginning and at the end of the dust concentration phase. The gas (red) remains in steady state during this phase. The dust is initialized with a dust-to gas ratio of $\epsilon = 0.01$ (dashed blue line). The dust component is evolved for 10^5 yrs (solid blue line) in which the dust concentrates at the inner disk, reaching $\epsilon \approx 0.24$ at the inner boundary of the dead zone, and $\epsilon \approx 0.16$ inside this region $r < r_1 = 0.51$ au.

at every radius. Since in this phase we only care about the inner disk, we adjust our simulation radial domain to be from $r_{\rm in} = 0.05$ au to $r_{\rm out} = 5$ au. The radial grid is defined as follow:

- 25 linear-spaced grid cells at $r = 0.05 - 0.09$ au,
- 120 logarithmic-spaced grid cells at $r = 0.09 - 1.0$ au,
- 20 logarithmic-spaced grid cells at $r = 1.0 - 5.0$ au.

The innermost region is necessary to avoid numerical problems with the inner boundary conditions. For optimization purposes we also turn off coagulation for $r < 0.09$ au, since the growth and fragmentation timescales are so short in this region that the simulation becomes computationally unfeasible. Moreover, according to Akeson et al. (2005); Eisner et al. (2007) the inner boundary of RW Aur A disk should be around $r \sim 0.1 - 0.2$ au. For these reasons all our analysis will only focus on the region of interest between $r = 0.1 - 1.0$ au. We interpolate the gas and dust surface densities from the TwoPopPy simulation into the new grid, and use the coagulation model of DustPy to obtain the corresponding size distribution of the particles at $t = t_{\rm r}$ for every radius. The dust distribution obtained at this phase is shown in Figure 4.3, where the grains adjust to the fragmentation limit in the dead and active zones.

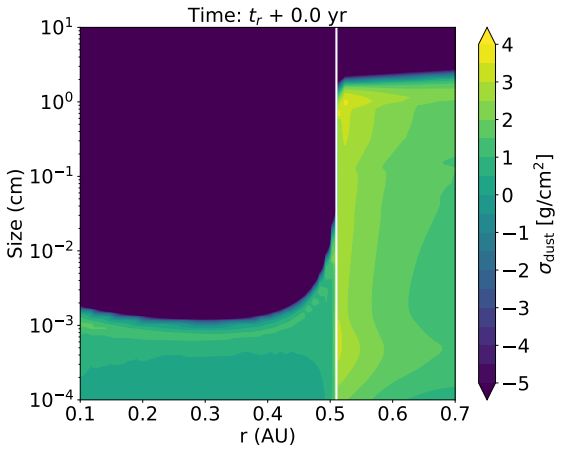

Figure 4.3: Dust distribution in the inner region of the protoplanetary disk immediately before the dead zone reactivation ($t = t_r$). In the dead zone, where the turbulence and the collision speed of solids are lower, the dust particles can grow to larger sizes ($a_{max} \sim 1\,cm$) before reaching the fragmentation limit. At the active zone, the particles are respectively smaller ($a_{max} \sim 10\,\mu m$). The inner edge of the dead zone (marked by the white line) presents a high concentration of large dust grains.

4.3.4 Phase 3: Dead Zone Reactivation

For the final phase we simulate the evolution of dust and gas in the inner disk, after the reactivation of the dead zone ($t > t_r$).
Once again we use the DustPy code, this time to solve the advection of gas and dust, along with the dust coagulation-fragmentation. We start this phase from the conditions given at Section 4.3.3, using the same grid for mass and radius, but now with the reactivated turbulence following Equation 4.4. We let the simulation evolve for 15 yrs, in which we expect that the material accumulated at the inner boundary of the dead zone will drift towards the star. The results of this phase on the accretion rate of gas and dust, as well as the final dust distribution, will be shown in Section 4.4.[2]

4.3.5 Parameter Space

In Table 4.1 we summarize the parameters used for the disk setup of our fiducial simulation. As the properties of the dead zone are free parameters, chosen to be in a relevant range for the RW Aur dimming problem, we also require to explore (even briefly) the parameter space for these properties, and see how they affect the final outcome of the simulations. We present five additional simulations, changing one parameter of the fiducial model at a time, this way we explore the effect of having: no initial dust accumulation at reactivation,

[2]The simulation data files and a plotting script are available in zenodo: doi.org/10.5281/zenodo.1495061.

Table 4.1: Fiducial simulation parameters.

Parameter	Value
Σ_0	$50\,\mathrm{g/cm^2}$
T_0	$250\,\mathrm{K}$
r_0	$1\,\mathrm{au}$
α_{active}	10^{-1}
α_{dead}	10^{-4}
r_1	$0.51\,\mathrm{au}$
r_2	$10\,\mathrm{au}$
t_{r}	$10^5\,\mathrm{yrs}$
Back-reaction	Off

Table 4.2: Parameter variations.

Simulation	Parameter Changed
Control Simulation	$t_{\mathrm{r}} = 0\,\mathrm{yrs}$
Shallow Dead zone	$\alpha_{\mathrm{dead}} = 10^{-3}$
Closer Inner Edge	$r_1 = 0.25\,\mathrm{au}$
Closer Outer Edge	$r_2 = 4\,\mathrm{au}$
Back-reaction	On

different dead zone properties, and the expected effects of back-reaction in the final result. The parameter changes are described in Table 4.2.

4.4 Dead Zone Reactivation Results

In this section we show the results obtained on the dust and gas dynamics after the "dead zone reactivation phase" (Section 4.3.4), including the final dust distribution, the dust-to-gas ratio at the inner boundary, and accretion rates of dust and gas. We also study the impact of the dead zone parameters on the final outcome, to see if these results follow the expected behavior.

The gas and dust surface densities before and after the reactivation are shown in Figure 4.4. The initial surface density obtained from the first accumulation phase shows a dust-to-gas ratio of $\epsilon = 0.24$ at the dead zone inner edge, and $\epsilon = 0.16$ in the inner disk ($r \lesssim 0.5\,\mathrm{au}$). After the reactivation ($t > t_r$) the dust accumulated at the dead zone is transported towards the inner regions faster than the gas, reaching the inner boundary of the disk ($r_{\mathrm{in}} \sim 0.1 - 0.2\,\mathrm{au}$ (Akeson et al., 2005; Eisner et al., 2007)) in only 15 years.

Given that the surface density of dust at the dead zone edge was higher than the gas surface density at the inner regions, this leads to higher concentrations of dust than gas after the reactivation ($\epsilon > 1$). This should obviously make the dust dynamically important

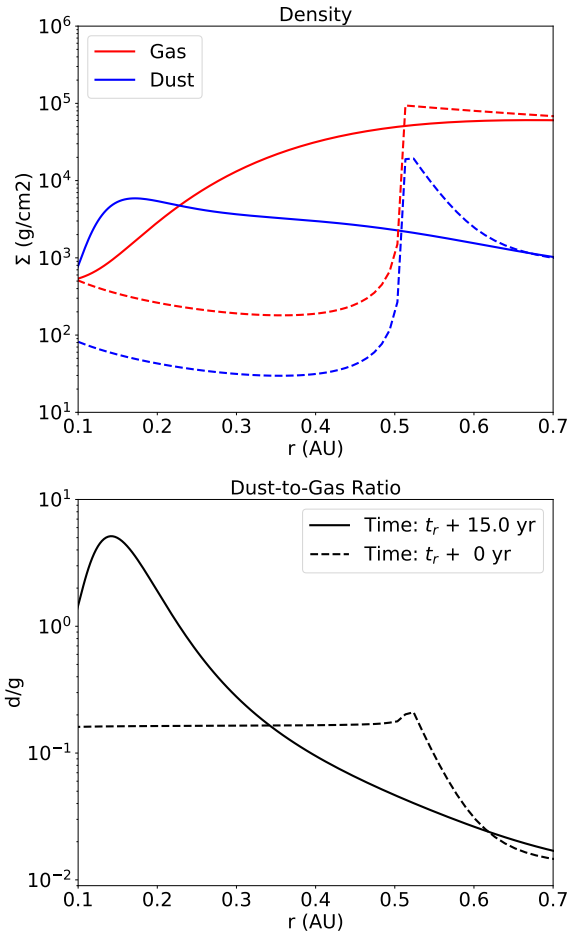

Figure 4.4: The plots show the simulation state immediately before the dead zone reactivation at $t = t_{\rm r}$ (dashed lines), and 15 yrs after it (solid lines). *Top*: Evolution of the gas (red) and dust (blue) surface densities. The initial state shows the gas steady state profile and the accumulation of dust at the inner boundary of the dead zone. After reactivation the accumulation of dust flushes towards the star faster than the gas. *Bottom*: Dust-to-gas ratio evolution. At the initial state the inner region presents an already high solid concentration thanks to mixing at the dead zone boundary. During the flushing the dust-to-gas ratio reaches values of $\epsilon = 5$ at some of the regions where the dust concentration arrived before the gas.

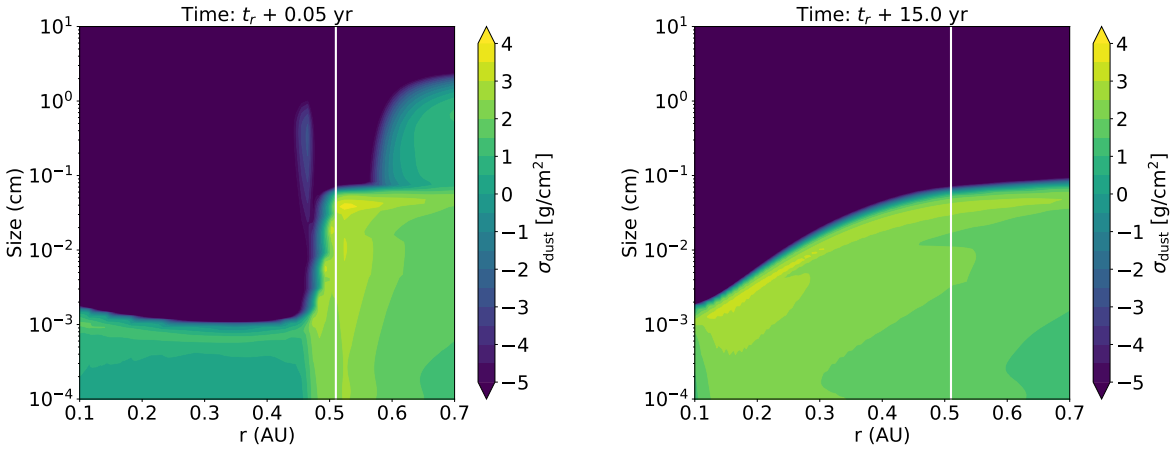

Figure 4.5: Dust distribution in the inner region of the protoplanetary disk after 0.05 and 15 yrs of the dead zone reactivation. *Top*: The dust that was accumulated at the dead zone diffuses to the inner region within ~ 10 collisional times, generating high dust-to-gas concentrations. The original edge of the dead zone is marked in white. *Bottom*: Afterwards, the dust drifts towards the inner disk regions ($r \sim 0.1 - 0.2$ au) within ~ 15 yrs, while adjusting to the new fragmentation limit.

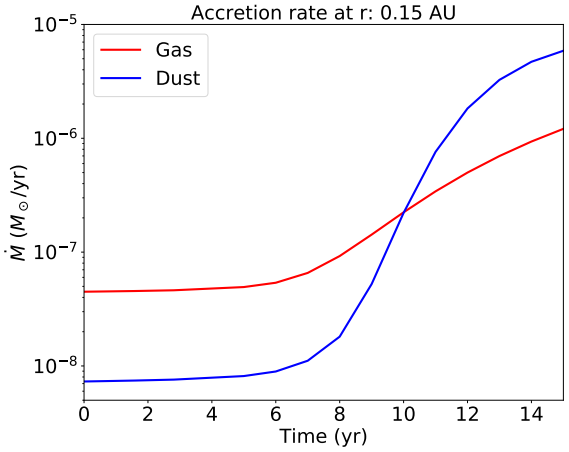

Figure 4.6: Accretion rate of gas (red) and dust (blue) at $r = 0.15$ au for 15 yrs after the dead zone reactivation. The initial gas accretion rate is $\dot{M}_g = 5 \times 10^{-8}\,M_\odot/\mathrm{yr}$, in agreement with the observations of RW Aur A, while the dust accretion rate is $\dot{M}_d = 7 \times 10^{-9}\,M_\odot/\mathrm{yr}$. Upon reactivation the dust accretion rate increases faster than the gas, eventually surpassing it after 10 yrs, and reaching a high value of $\dot{M}_d = 6 \times 10^{-6}\,M_\odot/\mathrm{yr}$.

to the gas motion, however we shall see later in this section that as the particles are too small ($\mathrm{St} < 10^{-3}$), the only impact of dust back-reaction is to slow down the dust and gas evolution. Therefore no instabilities are generated and we can proceed with our analysis.
Upon entering the active zone the particles fragment due to the high turbulence and adjust to their fragmentation limit (see Equation 1.28) in a few collisional timescales t_{coll}, which can be approximated by:

$$t_{\mathrm{coll}} = (n_{\mathrm{d}} \sigma \Delta v_{\mathrm{turb}})^{-1}, \tag{4.5}$$

where n_{d} is the number density of dust particles, $\sigma \approx 4\pi a^2$ is the collisional cross section, and $\Delta v_{\mathrm{turb}} \approx \sqrt{3\alpha \mathrm{St}} c_s$ is the turbulent collision speed (Ormel & Cuzzi, 2007).
We find that during 10 collisional timescales ($t \sim 0.05\,\mathrm{yrs}$) after the dead zone reactivation the dust grains diffuse inward faster than the gas, gaining a head start that leads to high dust-to-gas ratio concentrations. We attribute this feature to the sudden rise in the turbulence α at the dead zone inner edge, that increases the dust diffusivity and spreads the particles towards the inner regions (see Equation 1.25 and Figure 4.5). After the dust has adjusted to the new fragmentation limit, it drifts roughly with the viscous velocity of the gas v_ν towards the inner boundary of the disk. The particles reaching the inner boundary reach maximum sizes between $a_{\mathrm{max}} = 10 - 100\,\mu\mathrm{m}$ (see Figure 4.5).
The accretion rate (measured at $r = 0.15\,\mathrm{au}$) of both dust and gas increases after the reactivation of the dead zone, as the accumulated material arrives at the inner boundary of the disk (see Figure 4.6). Before the dead zone reactivation, the gas accretion rate is given by the steady state solution with $\dot{M}_{\mathrm{g}} = 5 \times 10^{-8}\,\mathrm{M}_\odot/\mathrm{yr}$, similar to the observational value of (Facchini et al., 2016; Ingleby et al., 2013), and the dust accretion rate is $\dot{M}_{\mathrm{d}} = 7 \times 10^{-9}\,\mathrm{M}_\odot/\mathrm{yr}$, this value comes from the dust diffusing into the inner disk during the concentration phase.
After the dead zone reactivation the dust concentration moves inwards, and the accretion rate at the inner boundary of the disk becomes dominated by the dust, to the point of surpassing that of the gas. This high supply of solid material, with $\dot{M}_{\mathrm{d}} = 6 \times 10^{-6}\,\mathrm{M}_\odot/\mathrm{yr}$ could cause hot dust and metallicity features of RW Aur A (Shenavrin et al., 2015; Günther et al., 2018), and provide an ideal environment for the dimmings to occur (see Section 4.5.1). At this point we also note that the accretion rate of gas has increased up to $\dot{M}_{\mathrm{g}} = 10^{-6}\,\mathrm{M}_\odot/\mathrm{yr}$.
In Section 4.5 we will discuss how the high accretion of solids could cause the dimmings in the context of previous proposed mechanisms (dusty winds, puffed-up inner disk rim, etc), and if we can expect future accretion signatures from the gas. In the following subsections, we study the effect of the simulation parameters on the dust dynamics.

4.4.1 Simulation without Dust Concentration

In our model we remained agnostic to the reactivation process of the dead zone, and allowed the dust to accumulate for long enough time to reach concentrations as high as $\epsilon = 0.24$ at its inner edge. Depending on the mechanism that reactivates turbulence, the flushing of solid material towards the star may occur earlier with lower dust concentrations, reducing

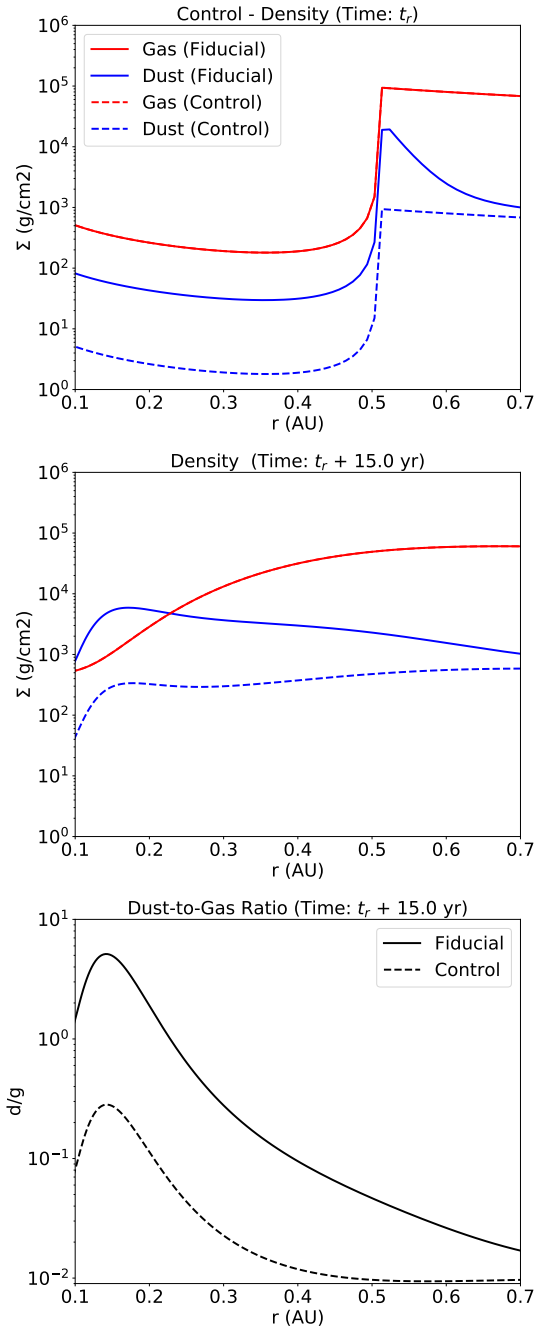

Figure 4.7: Comparison between the "fiducial" simulation ($t_r = 10^5$ yrs, solid lines) and the "control" simulation ($t_r = 0$ yrs, dashed lines). *Top*: Gas and dust densities at the reactivation time ($t = t_r$). In both cases the gas is in steady state, but in the control simulation the dust did not had the time to accumulate at the inner edge of the dead zone, in this case the reactivation occurs with a uniform dust-to-gas ratio $\epsilon = 0.01$. *Mid*: Gas and dust densities after the dead zone reactivation ($t = t_r + 15$ yrs). The dust that was at the dead zone in steady state still arrives faster than the gas to the inner boundary of the disk. *Bottom*: Dust-to-gas ratio after the reactivation. The maximum dust concentration in the "control" simulation is now $\epsilon = 0.28$.

the total accretion of solids. To model the limit case in which no dust concentration occurs, we repeat our setup with a control simulation, but now setting the reactivation time to $t_r = 0\,\mathrm{yrs}$.
In Figure 4.7 we show the initial and final state of both simulations. Here the control simulation has an uniform $\epsilon = 0.01$ in the beginning, since no additional dust concentration has occurred. Notice that we still assume that the gas has reached the steady state density profile.
After the reactivation the gas and dust excess at the dead zone drift towards the star. As in the fiducial case, the dust that was located at the dead zone inner edge arrives at the inner boundary of the disk before the gas, also in a time of $\sim 15\,\mathrm{yrs}$. The only difference is that now the material being accreted has a dust-to-gas ratio of $\epsilon = 0.28$, which is still higher than the initial $\epsilon = 0.01$, although not as extreme as the $\epsilon = 5$ found in the fiducial case. Here the dust accretion rate at the inner boundary of the disk ($r \approx 0.15\,\mathrm{au}$) can reach up to $\dot{M}_\mathrm{d} = 3 \times 10^{-7}\,\mathrm{M}_\odot/\mathrm{yr}$.
From here we learn that the dust arrival time at the inner boundary does not depend on the amount of solids accumulated at the dead zone inner edge, and that upon reactivation the accreted material will still carry a high concentration of solids.

4.4.2 Simulations for Different Dead Zone Properties

The dead zone shape is parametrized by its edges r_1 and r_2, and the turbulence parameter α_dead following Equation 4.1, and altering these parameters also changes arrival time and dust-to-gas ratio of the accreted material.
By shifting the inner edge of the dead zone to smaller radii ($r_1 = 0.51\,\mathrm{au} \rightarrow 0.25\,\mathrm{au}$) the dust concentration during the first phase will also be located closer to the inner boundary of the disk (see Figure 4.8). Now it only takes the dust between $3-5\,\mathrm{yrs}$ to reach the inner boundary of the protoplanetary disk. Therefore the inner edge of the dead zone regulates the time required between the reactivation and the accretion of the dusty material.
A dead zone with a closer outer boundary ($r_2 = 10\,\mathrm{au} \rightarrow 4\,\mathrm{au}$) will be smaller and concentrate less dust at its inner boundary (see Figure 4.9). This also reduces the total amount of solid material that it is accreted towards the star, although this is still a considerable amount with a dust-to-gas ratio of $\epsilon = 2.1$.
Finally, the most significant parameter is the turbulence α_dead of the dead zone. Our fiducial simulation considered an $\alpha_\mathrm{dead} = 10^{-4}$, which in contrast with the active zone $\alpha_\mathrm{active} = 10^{-1}$ leads to an accumulation of material in the dead zone with a factor of 1000 relative to the steady state of a fully active disk, this of course favors the accretion of massive amounts of gas and solids upon reactivation. By taking a shallower dead zone ($\alpha_\mathrm{dead} = 10^{-4} \rightarrow 10^{-3}$) there is less gas and dust accumulated, so upon reactivation the flushing of material is slower by a factor of a few (see Figure 4.10). We also find that for $\alpha_\mathrm{dead} = 10^{-3}$ there is no significant concentration at the dead zone inner edge, after $10^5\,\mathrm{yrs}$ the dust-to-gas ratio rises only up to $\epsilon = 0.012$. This happens because the higher turbulence lowers the fragmentation limit (see Equation 1.28), producing particles that

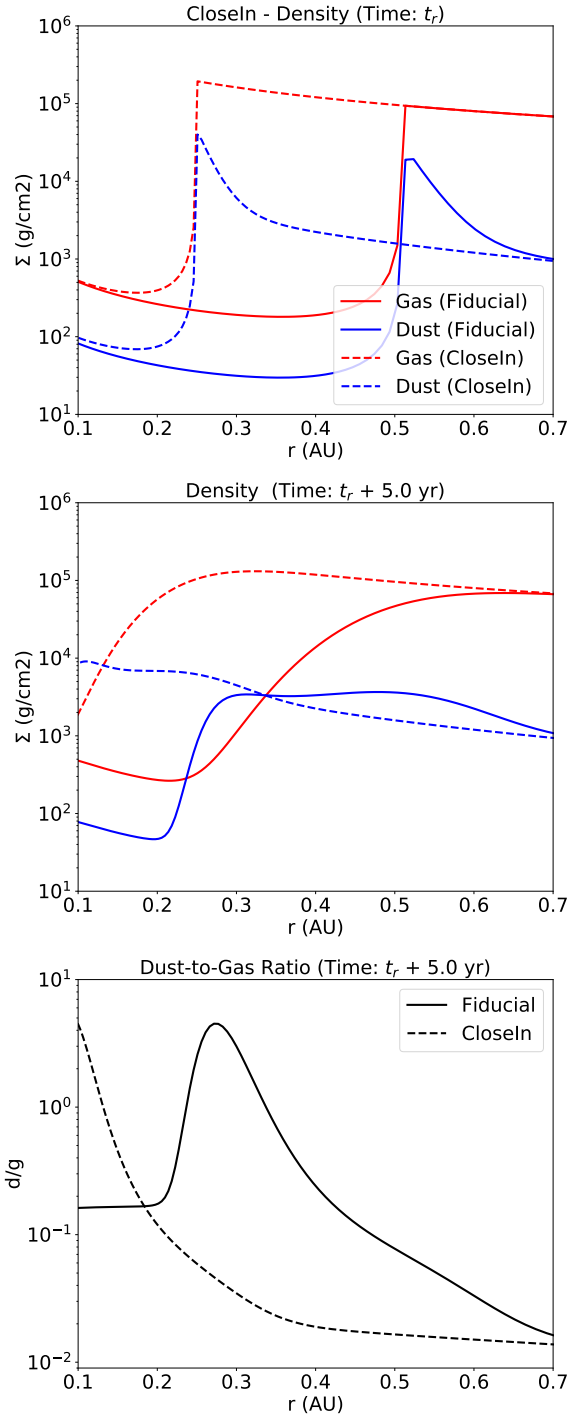

Figure 4.8: Same as Figure 4.7, but comparing the "fiducial" simulation ($r_1 = 0.51\,\mathrm{au}$) with the "closer inner edge" simulation ($r_1 = 0.25\,\mathrm{au}$). *Top*: Initially, the dead zone is more extended toward the inner boundary of the disk. *Mid*: After reactivation, the dust concentration arrives in only 5 yrs to the inner edge of the disk, also moving faster than the gas. *Bottom*: The maximum dust-to-gas ratio for the "closer inner edge" is similar to the "fiducial" value with $\epsilon \approx 5$.

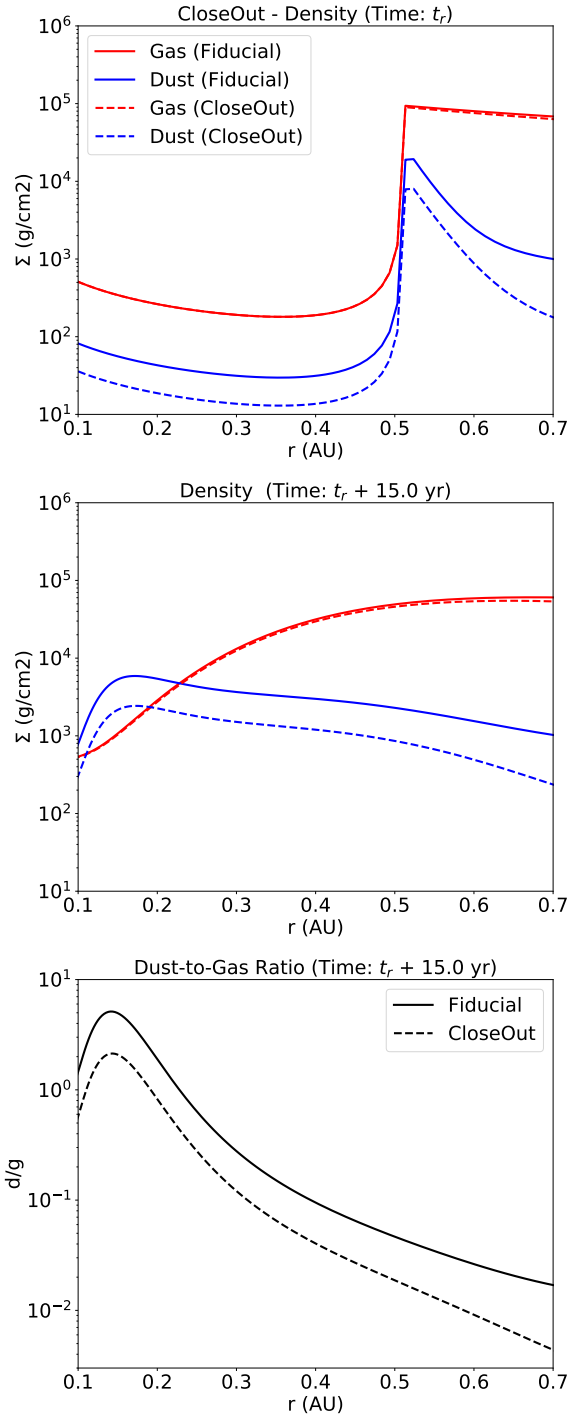

Figure 4.9: Same as Figure 4.7, but comparing the "fiducial" simulation ($r_2 = 10\,\mathrm{au}$) and the "closer outer edge" simulation ($r_2 = 4\,\mathrm{au}$). *Top*: Initially the dead zone is smaller and has less material, leading to a lower dust concentration at its inner edge of $\epsilon = 0.1$. *Mid*: The dust excess once again arrives to the inner boundary of the disk before the gas in 15 yrs, but in a lower concentration. *Bottom*: The maximum dust-to-gas ratio for the "closer outer edge" simulation is now $\epsilon \approx 2$.

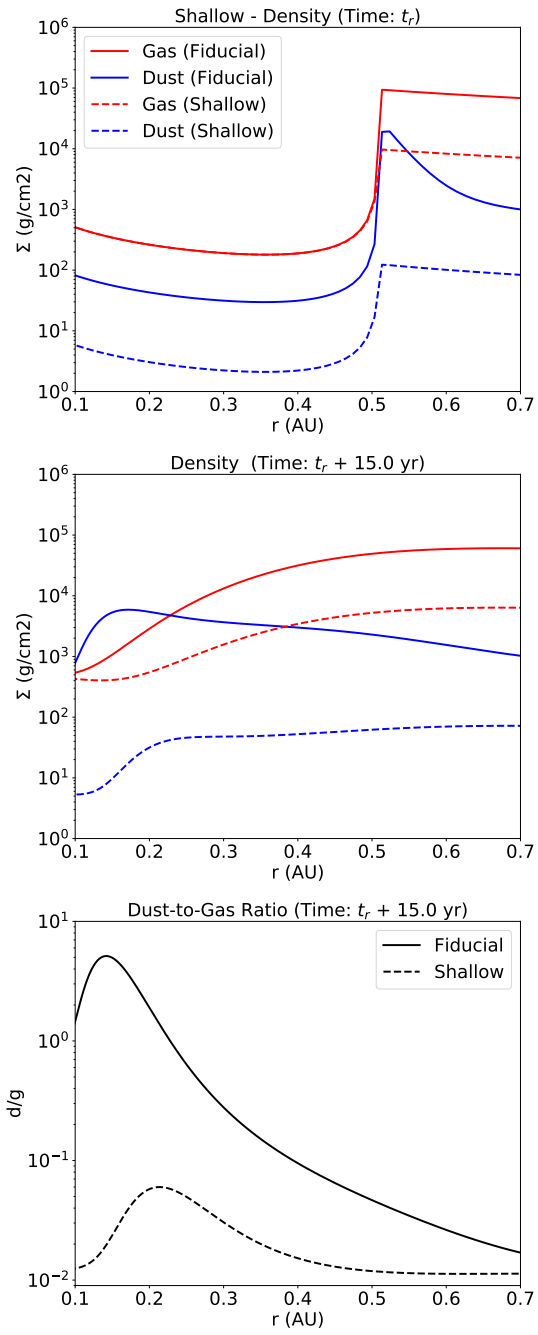

Figure 4.10: Same as Figure 4.7, but comparing the "fiducial" simulation ($\alpha_{\rm dead} = 10^{-4}$) and the "shallower dead zone" simulation ($\alpha_{\rm dead} = 10^{-3}$). *Top*: There is no notable accumulation of material at the inner edge of the dead zone during the accumulation phase, with $\epsilon = 0.012$ at most. Probably because the particles are too small to get trapped, and diffuse more easily to the inner region. *Mid*: After 15 yrs there is only a little dust excess traveling towards the inner region, a small bump can still be appreciated in the dust surface density profile. *Bottom*: The final dust-to-gas ratio in the inner boundary is only $\epsilon = 0.06$, just a factor of a few above the original $\epsilon = 0.01$. This is because the lack of more material in the entire dead zone.

drift slower towards the pressure maximum (which now is also shallower).
The final results is that the accreted material after the dead zone reactivation only has a dust-to-gas ratio of $\epsilon = 0.06$. Therefore we find that the turbulence parameter $\alpha_{\rm dead}$ of the dead zone is the main determinant of the total amount of material being accreted, and that deeper dead zones are necessary to produce the dust dominated accretion seen in our fiducial simulation.

4.4.3 Simulation with Dust Back-reaction

In all our results until this point we have neglected the back-reaction of dust to the gas, however for the dust-to-gas ratios presented during the dead zone reactivation ($\epsilon \gtrsim 1$) this effect should be relevant. In this section we study its impact to see if our previous results remain valid.
First, we should mention that in this setup we only consider the back-reaction in the "re-activation phase", and assume that the dust will still accumulate at the inner edge of the dead zone even if back-reactions are considered. This is still justified since our particles are too small ($\mathrm{St} < 10^{-3}$) to cause any perturbation beyond slowing down the concentration process and we can be infer it also by studying the single dust species scenario described in the Section 2.2. Studies of Onishi & Sekiya (2017) also showed that the back-reaction still allows the dust to accumulate at pressure maxima, and that the dust traps do not self-destruct by this effect when taking into account the vertical distribution of solids.
For the reactivation phase we implement the gas velocities as described by equations Equation 2.3 and Equation 2.4. In the radial direction, the gas velocity now consist of two terms modulated by the back-reaction coefficients $0 < A, B < 1$, the term Av_ν is slowing down the viscous evolution of the gas respect to the default value v_ν, and the term $2B\eta v_{\rm K}$ is pushing the gas in the direction opposite to the pressure gradient.
Since the vertical distribution of particles is not exactly the same as the gas, the effect of the back-reaction is also not uniform in the vertical direction, the importance of this point is shown in Dipierro et al. (2018); Onishi & Sekiya (2017). To account for the vertical effect of back-reactions in our 1D simulations we take the vertically averaged velocity for the dust and gas, weighted by the mass density to conserve the total flux. The details for this implementation can also be found in Section 2.3.
In Figure 4.11 we show a comparison between the "fiducial" and "back-reaction" simulations 15 years after the dead zone reactivation. When the back-reaction is considered the most notable effect is the slowing down of the accretion of material by a factor of ~ 2. While the dust particles in the "fiducial" simulation take 15 years to reach the inner boundary of the disk, in the "back-reaction" simulation they need 30 years instead.
The reason why no further effects are observed is that the high turbulence causes fragmentation of the particles to smaller sizes (as seen in Figure 4.5), where they are unable to "push" the gas backwards (i.e. the term $B \to 0$), and are only able to reduce the gas viscous velocity by a factor of $A \leq 1$.
Another effect of the back-reaction is that the maximum dust-to-gas ratio has also decreased to a value of $\epsilon = 2.5$ because of the dust and gas redistribution by their coupled

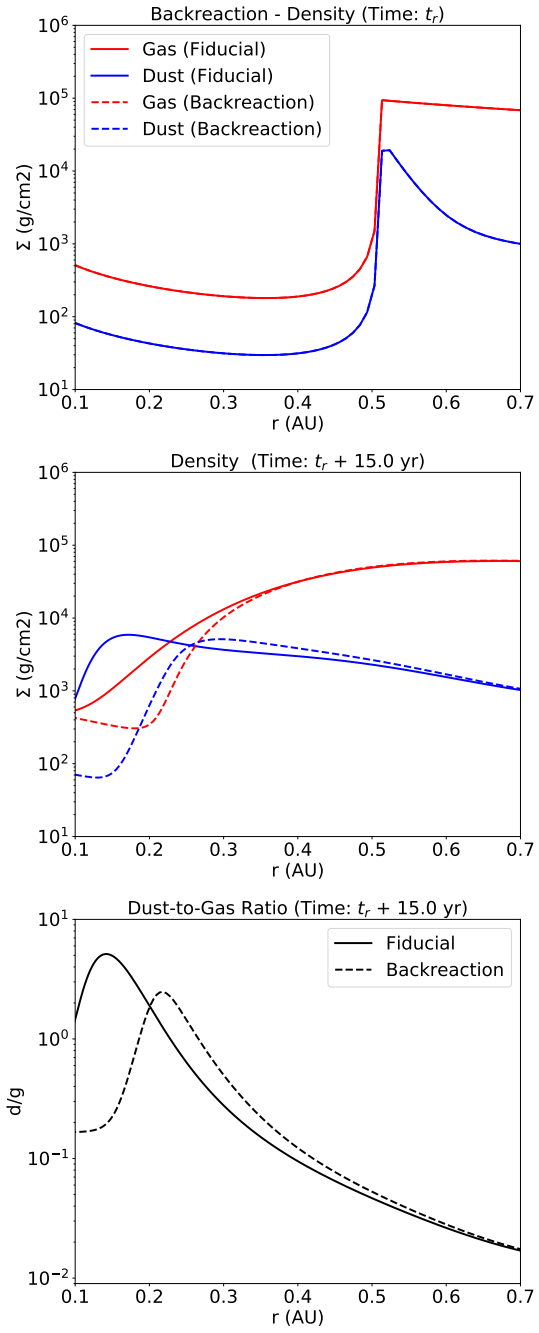

Figure 4.11: Same as Figure 4.7, but comparing the "fiducial" simulation and the "back-reaction" simulation. *Top*: Both simulations start at the reactivation time with the same initial conditions. *Mid*: When back-reaction is considered, the evolution of the dust and gas component is slower than in the fiducial case. This is because the high dust concentrations slow down the viscous evolution of the gas, which in turn also slows down the drifting of the dust towards the inner disk. *Bottom*: Both the simulation with and without back-reaction present a high concentration of dust in the accreted material, yet in the case with back-reaction the bulk of dust reaches a radii of only $r = 0.22\,\mathrm{au}$ in 15 years, while the dust in the fiducial simulation is already at $r = 0.15\,\mathrm{au}$.

interaction (the dust concentration does not increase with time to the fiducial $\epsilon = 5$ value). This means that in all our previous results we should consider that the accreted material will take more time (a factor ~ 2, if the dust-to-gas ratio is high enough) to reach the inner boundary of the protoplanetary disk, and as consequence that the accretion rate will also be reduced.
An order of magnitude estimate for the back-reaction coefficients can be obtained by approximating the particle distribution to a single size population (see Section 2.2, Equation 2.13 and 2.14), in which $A \approx (\epsilon + 1)^{-1}$ and $B \approx \mathrm{St}\ \epsilon\ (\epsilon + 1)^{-2}$, however to have an overall estimate for the entire disk the dust-to-gas distribution should be taken into account.

4.5 Discussion

We have seen that through the reactivation of a dead zone, located in the inner regions of RW Aur A circumstellar disk, large amounts of dust can be flushed towards the star in timescales that can go between $5 - 30$ years. In this section we compare our results on dust accretion with the properties of the dimmings, speculate upon the future accretion signatures of RW Aur, and discuss which ingredients of our model may be improved to better match the observations.

4.5.1 The Fast Accretion Mechanism in the Context of RW Aur A Dimmings

Multiple observations during the dimmings of RW Aur A reveal the presence of large amounts of dust at small radii, in the line of sight, and in the material accreted by the star (see Section 4.1.1). Our model with dead zone reactivation provides a way to increase the dust at the inner rim of the protoplanetary disk by 2 orders of magnitude from its original value (from $\Sigma_\mathrm{d} = 50\,\mathrm{g/cm^2}$ to $5 \times 10^3\,\mathrm{g/cm^2}$ at $0.15\,\mathrm{au}$). Although this alone does not explain the dimmings, as a significant amount of material still needs to be moved towards the line of sight, it relaxes the conditions of other mechanisms that can do so.
In the case that the dimmings are caused by a dusty wind coming from the inner regions (Petrov et al., 2015; Shenavrin et al., 2015), the dead zone reactivation increases the amount of dust entangled with the gas, and then the particles would be dragged into the line of sight by the wind if they are small enough to be coupled to the gas.
Similarly, if the dimmings are caused by a puffed up inner rim of the disk (Facchini et al., 2016; Günther et al., 2018), the reactivation of the dead zone not only increases the amount of solid material in the line of sight (since our particles are small they should be well mixed with the gas in the vertical direction), but also can increase the scale height of these regions with the rise in temperature due to accretion heating. If our model is correct, in the following decade(s) the gas accretion rate should also increase by more than one order of magnitude, up to $\dot{M}_\mathrm{g} = 10^{-6}\,\mathrm{M_\odot/yr}$, as the gas excess from the dead zones adjusts to a new steady state.

4.5.2 A Single Reactivation Event, or Multiple Short Reactivation Spikes?

The dimmings of RW Aur A last from a few months up to two years (see the list in Rodriguez et al., 2018), repeatedly moving from the dimmed state to the bright state. The accretion process described in our model last from several years to a few decades (depending on the simulation parameters), which is clearly longer than the typical dimming duration, and without presenting any decrease in the dust accretion rate over the process. Yet, we can think of a few ways to reconcile the timescales of our simulations with the dimmings.
The first possibility is that the reactivation of the dead zone, and the subsequent increment in the accretion rate (see Figure 4.6), can also raise the temperature of the inner disk through viscous heating, resulting in a puffed-up inner rim. In this case, the dimmings will occur in the time required to drag the dusty material into the line of sight as the scale height of the inner disk increases, and will finish once the material settles back down or is completely accreted.
In a similar way, if the dead zone reactivation is accompanied by stronger stellar winds, these will determine the timescale of the dimmings within the accretion event described by our model.
Also, the accretion process described in our model does not need to increase smoothly, and can present variability in shorter timescales. Instabilities that are not resolved by our model during the accretion process may produce a bumpy surface density profile in dust and gas, for example through the ring instability (Wünsch et al., 2005) for dead zones in layered disks. In this case the dimming events would correspond to the local maximums in the accretion of dust.
Another possibility is that the dead zone reactivation is not instantaneous. In the case that only inner edge becomes active, a fraction of the accumulated dust will start drifting towards the star, leaving most of the gaseous and solid material still trapped in the dead zone. If multiple reactivation events like this take place, the corresponding dust excess will also arrive in intervals, with a frequency depending on the reactivation mechanism. In this case the dimmings would start when a spike of dust accretion arrives to the inner edge, and end once it decreases back to its steady state value. To improve our model we would need to resolve the thermal and gravitational instabilities that can reactivate the dead zone (Martin & Lubow, 2011).
Finally, azimuthal asymmetries in the inner disk (such as vortices) may also add variability to the accretion process, but these are not considered by our model.
A further monitoring of the metallicity of the accreted material would help understand the nature of the dust accretion process and the mechanism that drags the dust into the line of sight. If the dust accretion continues delivering material to the star, independently of the dimmings, then the metallicity should remain high even after the luminosity returns to the bright state. Otherwise, if the rise in metallicity keeps correlating with the dimmings (as in Günther et al., 2018), the dimmings could be an outcome of the sudden increase in the dust accretion (although of course, correlation does not imply causality).

4.5.3 Validity of the Dead Zone Model

Our results showed that the exact values of dust accretion rate and timescales depend sensitively on the parameters used for the dead zone. A dead zone inner edge closer to the inner boundary of the disk reduces the timescale of the process, a closer outer edge reduces the total mass of the dead zone, and the turbulence parameter $\alpha_{\rm dead}$ and the reactivation time determine the amount of dust that can be trapped and flushed towards the star. In addition, the shape of the dead zone profile also affects dust and gas surface density profiles, and a proper modeling of the gas turbulence would be required to obtain their final distributions after the dead zone reactivation.
With this amount of free parameters, our simulations provide more a qualitative scenario than quantitative predictions. Further constrains are necessary to determine how relevant the reactivation of a dead zone can be for RW Aur A dimmings. The first step is of course to find the mechanism that puts the required amounts of dust in the line of sight, and obtain an estimate of the required dust surface density at the inner disk (not only in the line of sight) to produce this phenomena.
In parallel, any signature of enhanced gas accretion rate in the following years would speak in favor of the dead zone reactivation mechanism as one of the drivers of the dimmings.
Additionally, constrains on the properties of the inner disk would limit the parameter space described. In particular, the mass in the inner 10 au of RW Aur A disk would be useful to constrain the outer edge and turbulence parameter of the dead zone, and with them the amount of material that can be thrown to the star.

The Dead Zone as an Accretion Reservoir

One point that speaks in favor of our model is its potential to sustain the large accretion rates of RW Aur for extended periods of time. Considering only the observed values for the disk mass and the accretion rate, the maximum lifetime of RW Aur would be of $M_{\rm g}/\dot{M}_{\rm g} \sim 10^4$ - 10^5 yrs which is too short for a T Tauri star.
Rosotti et al. (2017) defined the dimensionless accretion parameter:

$$\eta_{\rm acc} = \tau_* \dot{M}/M_{\rm disk}, \tag{4.6}$$

with τ_* the age of the star, that indicates if the properties of a disk are consistent the steady state accretion, in which case it follows $\eta_{\rm acc} \lesssim 1$. The RW Aur A is around 5 Myr old (Ghez et al., 1997) and presents an accretion parameter of $\eta_{\rm acc} \approx 60$, indicating either that the disk is not in steady state, or that the observed disk mass is underestimated.
In our model, the dead zone provides a reservoir of material able to sustain the detected accretion rates for around 2Myrs (considering the parameters of our fiducial simulation), which is close to the estimated age of the star. At the same time, at high densities the dusty material would be optically thick, remaining hidden from the mm observations used to measure the disk mass.

Another Free Parameter for Dust Growth?

In our model we considered that the turbulent α that limits dust growth by fragmentation (Equation 1.28), is the same that drives the viscous evolution of the gas (Equation 1.4), yet recent models explore the case with two independent α values for each process (e.g., Carrera et al., 2017). For our model, using a single α value means that particles reach bigger sizes while they remain in the dead zone, and fragment to smaller sizes in the active region.
Allowing two independent alpha values would allow the formation of large particles in the active region. These larger particles drift faster, but also exert a stronger back-reaction on the gas. The "pushing" back-reaction coefficient B is roughly proportional to the particle size (see Section 2.2, Equation 2.13 and 2.14), and at the high dust-to-gas ratios found during the dead zone reactivation, it could be strong enough to generate density bumps in the gas, or even trigger the streaming instability for particles with large enough Stokes number (Youdin & Goodman, 2005).

4.6 Summary

In this work we studied a new mechanism that can increase the concentration of solids in the inner regions of a protoplanetary disk in timescales of ~ 10 years, through the reactivation of a dead zone.
This study was motivated by the recent dimmings of RW Aur A, which present a high concentration dust in the line of sight (Antipin et al., 2015; Schneider et al., 2015), and an increased emission from hot grains coming from the inner regions of the protoplanetary disk(Shenavrin et al., 2015), and subsequently observed super-solar metallicity of the accreted material(Günther et al., 2018).
Using 1D simulations to model the circumstellar disk of RW Aur A, we find that the dust grains accumulate at the inner edge of the dead zone, which acts as a dust trap, reaching concentrations of $\epsilon \approx 0.25$. When the turbulence in this region is reactivated, the excess of gas and dust is released from the dead zone and advected towards the star. By effect of dust diffusion and gas drag, the dust component can reach the inner boundary of the protoplanetary disk before the gas component, producing high dust concentrations of $\epsilon \approx 5$. The accretion rate of solids increases from $\dot{M}_{\rm d} = 7 \times 10^{-9}\,{\rm M}_\odot/{\rm yr}$ to $6 \times 10^{-6}\,{\rm M}_\odot/{\rm yr}$ in only 15 years. This scenario can provide an ideal environment for other mechanisms, such as stellar winds (Petrov et al., 2015; Shenavrin et al., 2015) or a puffed up inner rim (e.g., Facchini et al., 2016; Günther et al., 2018), to transport the required amount of solid material into the line of sight and cause the dimmings, although further studies are required to link the surface density at the midplane with the measured dust concentrations.
Additionally, our simulations predict that in the following decade(s) the gas accretion rate should also rise by an order of magnitude, from $\dot{M}_{\rm g} = 5 \times 10^{-8}\,{\rm M}_\odot/{\rm yr}$ to $10^{-6}\,{\rm M}_\odot/{\rm yr}$ if the dead zone reactivation is the mechanism transporting dust towards the disk inner region.

Chapter 5

Gas accretion damped by the dust back-reaction at the snowline

The contents of this chapter where published in the Astronomy & Astrophysics Journal.
Credit: Gas accretion damped by dust back-reaction at the snow line,
Gárate et al., A&A, 635, A149, 2020.

5.1 Introduction

At interstellar dust-to-gas ratios of 1% the force exerted by the dust into the gas is mostly negligible. Yet, in regions such as dead zones (Kretke et al., 2009; Pinilla et al., 2016), outer edges of gaps carved by planets (Dipierro & Laibe, 2017; Kanagawa et al., 2018), snowlines (Brauer et al., 2008b; Estrada et al., 2016; Drążkowska & Alibert, 2017; Stammler et al., 2017; Hyodo et al., 2019), and pressure bumps in general (Pinilla et al., 2012), particles can accumulate and grow to larger sizes, reaching concentrations where the dust back-reaction may be strong enough to alter the dynamics of the gas (Taki et al., 2016; Onishi & Sekiya, 2017; Kanagawa et al., 2017; Gonzalez et al., 2017; Dipierro et al., 2018). In particular, the water snowline acts as a traffic jam for the dust if there is a change in the fragmentation velocity between silicates and ices (Birnstiel et al., 2010; Drążkowska & Alibert, 2017; Pinilla et al., 2017). Previous results showed that the icy particles outside the snowline can grow to larger sizes (Gundlach et al., 2011) and drift faster to the inner regions. After crossing the snowline, the ice on the solid particles evaporates, leaving only dry silicates behind. Then, the silicates in the inner regions fragment to smaller sizes and drift at lower speeds, creating a traffic jam. The traffic jam effect can concentrate enough material to trigger the formation of planetesimals through streaming instability (Schoonenberg & Ormel, 2017; Drążkowska & Alibert, 2017; Drążkowska & Dullemond, 2018).
Here, we study the dynamical effect of the snowline on the gas dynamics, by considering the effect of the dust back-reaction onto the gas. We want to find under which conditions the dust can slow down or revert the gas accretion rate, and test if further structures can

appear beyond the snowline.
We use one-dimensional simulations that consider gas and dust advection, dust growth, and the back-reaction effects. To treat the global evolution of the disk we use the model of Birnstiel et al. (2012), that includes the size evolution of solids by using representative species, and implement the modifications introduced by Drążkowska & Alibert (2017), that model the evaporation and recondensation of water at the snowline.

5.2 Model Description

For our model we use the disk evolution theory described in Chapter 1, and in Chapter 2 to include the back-reaction effects. Now we proceed to describe our model for the water iceline.

5.2.1 Evaporation and recondensation at the snowline

To include the snowline in our simulations, we follow the model given by Drążkowska & Alibert (2017), which evolves four different species: a mix of hydrogen and helium, water vapor, silicate dust, and water ice that freezes over the silicate grains.
The gas phase is the sum of both hydrogen-helium and water vapor, it is traced by the surface density Σ_g, and is advected according to Equation 1.1. The water vapor, with surface density Σ_{vap}, is advected with the same velocity as the gas, but also diffuses according to the concentration gradient. The mean molecular weight of the gas phase is then:

$$\mu = (\Sigma_{H_2} + \Sigma_{vap}) \left(\frac{\Sigma_{H_2}}{\mu_{H_2}} + \frac{\Sigma_{vap}}{\mu_{vap}} \right)^{-1}, \tag{5.1}$$

where $\mu_{H_2} = 2.3$ and $\mu_{vap} = 18$ are respectively the mean molecular weights of the hydrogen-helium mixture and the water vapor, and $\Sigma_{H_2} = \Sigma_g - \Sigma_{vap}$ is the surface density of the standard hydrogen-helium mixture.
The dust grains are assumed to be a mixture of silicates and ices traced by Σ_d, evolved according to Equation 1.16, and have a material density of:

$$\rho_s = (\Sigma_{sil} + \Sigma_{ice}) \left(\frac{\Sigma_{sil}}{\rho_{sil}} + \frac{\Sigma_{ice}}{\rho_{ice}} \right)^{-1}, \tag{5.2}$$

where $\rho_{sil} = 3\,\mathrm{g\,cm^{-3}}$ and $\rho_{ice} = 1\,\mathrm{g\,cm^{-3}}$ are the densities of the silicates and ices, respectively, and $\Sigma_{sil} = \Sigma_d - \Sigma_{ice}$ is the surface density of the silicates.
The composition of the dust grains determines the fragmentation velocity, where icy grains are stickier and can grow to larger sizes than the silicate grains. As in Drążkowska & Alibert (2017), we assume that the particles have the fragmentation velocity of ices $v_{frag} = 10\,\mathrm{m\,s^{-1}}$ (Wada et al., 2011; Gundlach et al., 2011; Gundlach & Blum, 2015) if there is more than

1% of ice in the mixture, and the fragmentation velocity of silicates $v_{\rm frag} = 1\,{\rm m\,s^{-1}}$ (Blum & Wurm, 2000; Poppe et al., 2000; Güttler et al., 2010) otherwise.
The limit between evaporation and recondensation of water is given by the equilibrium pressure:

$$P_{\rm eq} = P_{\rm eq,0} \exp(-A/T), \tag{5.3}$$

with $P_{\rm eq,0} = 1.14 \times 10^{13}\,{\rm g\,cm^{-1}s^{-2}}$ and $A = 6062\,{\rm K}$ (Lichtenegger & Komle, 1991; Drążkowska & Alibert, 2017). The evaporation and recondensation of water are set to maintain the pressure of the water vapor at the equilibrium pressure (Ciesla & Cuzzi, 2006), with:

$$P_{\rm vap} = \frac{\Sigma_{\rm vap}}{\sqrt{2\pi} h_{\rm g}} \frac{k_{\rm B} T}{\mu_{\rm vap} m_{\rm H}}. \tag{5.4}$$

When the water vapor pressure is below this threshold ($P_{\rm vap} < P_{\rm eq}$) the ice evaporates into vapor as follows:

$$\Delta\Sigma_{\rm vap} = \min\left(\sqrt{2\pi} h_{\rm g} \frac{\mu_{\rm vap} m_{\rm H}}{k_{\rm B} T}(P_{\rm eq} - P_{\rm vap}),\, \Sigma_{\rm ice}\right), \tag{5.5}$$

and vice-versa, if the vapor pressure is higher then it recondenses into ice with:

$$\Delta\Sigma_{\rm ice} = \min\left(\sqrt{2\pi} h_{\rm g} \frac{\mu_{\rm vap} m_{\rm H}}{k_{\rm B} T}(P_{\rm vap} - P_{\rm eq}),\, \Sigma_{\rm vap}\right), \tag{5.6}$$

where the factor next to $\pm(P_{\rm vap} - P_{\rm eq})$ transforms the pressure difference at the midplane into surface density.
As shown by Birnstiel et al. (2010); Drążkowska & Alibert (2017), at the snowline a traffic jam of dust is created because of the difference in the fragmentation velocities of silicates and ices. Recondensation also contributes to enhance the amount of solids when the vapor diffuses and freezes back beyond the snowline (Stammler et al., 2017).

5.3 Simulation Setup

We use the code `twopoppy` (Birnstiel et al., 2012) to study the global evolution of a protoplantary disk for 0.4 Myr around a solar mass star, advecting the gas and the dust according to the back-reaction velocities described in Chapter 2, with the snowline model of Drążkowska & Alibert (2017) summarized above in Section 5.2.1.

5.3.1 Two-Population Dust Model

In `twopoppy` the dust is modeled as a single fluid composed of two populations, an initial small particle particle population, and a large particle population with the size limited by the growth barriers (Equation 1.28 and 1.30), with a factor correction: $\mathrm{St}_{\rm max} = \min(0.37 \cdot$

$\mathrm{St}_{\mathrm{frag}}, 0.55 \cdot \mathrm{St}_{\mathrm{drift}})$.
The dust velocity and the back-reaction coefficients are then calculated considering the mass fraction of the two populations. Birnstiel et al. (2012) found that the mass fraction of the large population if $f_{\mathrm{m}} = 0.97$ for the drift limited case, and $f_{\mathrm{m}} = 0.75$ for the fragmentation limited case.

5.3.2 Disk Initial conditions

The gas surface density and temperature profile are defined by the following power laws:

$$\Sigma_{\mathrm{g}}(r) = \Sigma_0 \left(\frac{r}{r_0} \right)^{-p}, \tag{5.7}$$

$$T(r) = T_0 \left(\frac{r}{r_0} \right)^{-q}, \tag{5.8}$$

with $r_0 = 1\,\mathrm{au}$, $\Sigma_0 = 1000\,\mathrm{g\,cm^{-2}}$, $T_0 = 300\,\mathrm{K}$, $p = 1$ and $q = 1/2$.
The disk surface density initially extends until $r = 300\,\mathrm{au}$. The disk size is intentionally large to provide a continuous supply of material during the simulation, and to make the interpretation of the back-reaction effects easier. We discuss the effect of the disk size in the outcome of the dust accumulation at the snowline in section 5.4.4.
We start the simulations with an uniform dust-to-gas ratio ε_0 such that $\Sigma_{\mathrm{d}} = \varepsilon_0 \Sigma_{\mathrm{g}}$, assuming that the solid material is composed of a mixture of 50 % ice and 50 % silicate (Lodders, 2003, Table 11). The water vapor is introduced in the simulation as the ice evaporates.
The dust phase has a turbulence parameter of $\alpha_t = 10^{-3}$, and an initial size of $a_0 = 1\,\mu\mathrm{m}$.

5.3.3 Grid and Boundary Conditions

The region of interest in our simulation extends from 0.1 to 300 au, with $n_r = 482$ logarithmically spaced radial cells.
To avoid possible effects of the boundary conditions in our region of interest, we add 20 additional grid cells in the inner region between 0.05 and 0.1 au, and 58 additional grid cells in the outer region between 300 and 600 au. In total, our simulation consist on 560 grid cells from 0.05 to 600 au.
The additional cells at the inner region where added to avoid measuring the accretion rate onto the star too close to the inner boundary. The additional cells in the outer region were added to give the gas enough space to spread outwards without being affected by the outer boundary conditions.
At the inner boundary we assume a constant slope for the quantity $\Sigma_{\mathrm{g,d}} \cdot r$. At the outer boundary we have an open boundary condition for the gas and set a constant dust-to-gas ratio (but because of the additional grid cells, the gas never expands all the way to the outer boundary).
To calculate the gas and dust velocities and take into account dust settling (Equation 2.18

Table 5.1: Parameter space.

Simulation	ε_0
Low ε_0	0.01
Mid ε_0	0.03
High ε_0	0.05

and 2.19) we construct a local vertical grid at every radius with $n_z = 300$ points, logarithmically spaced between $10^{-5}\, h_g$ and $10\, h_g$.

5.3.4 Parameter Space

The two most important parameters that control the strength of the back-reaction are the global dust-to-gas ratio ε_0, and the gas turbulent viscosity α_ν.
We will focus our study in three simulations with "Low", "Mid", and "High" global dust-to-gas ratios, with the respective values for ε_0 summarized in Table 5.1.
For the sake of clarity, through the paper we will use a single value for the turbulent viscosity, with $\alpha_\nu = 10^{-3}$. This turbulence is low enough for the back-reaction effects to start affecting the gas dynamics (i.e., the term $2\bar{B}v_P$ becomes comparable to $\bar{A}v_\nu$ in the gas velocity, Equation 2.3).
For completeness, in Appendix C of (Gárate et al., 2020) we further extend our parameter space[1] to include different values for the turbulent viscosity α_ν, though for simplicity we keep the dust turbulence constant, with $\alpha_t = 10^{-3}$.

5.4 Dust accumulation and gas depletion at the snowline

The evolution of gas is initially only dominated by the viscous accretion, but as time passes and dust grows, the back-reaction effects start to become dynamically important to the gas.
At the water snowline, the Stokes number changes by 2 orders of magnitude (Figure 5.1). In the inner disk, the particles can only grow to small sizes given by the fragmentation limit of silicates, while in the outer regions the dust size is limited by the fragmentation of water ice or the drift limit.
The simulations with the higher dust-to-gas ratio show an increment in the Stokes number at the snowline location, caused by the higher concentration of water vapor which increases the fragmentation limit (by increasing the the mean molecular weight, and decreasing the sound speed, see Equation 1.5, 1.28 and 5.1).
In the "Low ε_0" simulation (Figure 5.2, top panel), the change in particle size alone causes

[1]The simulation data files, including the extended parameter space, are available in Zenodo: doi.org/10.5281/zenodo.3552597

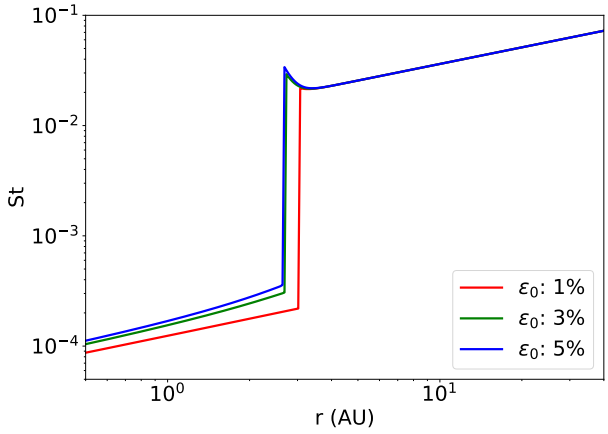

Figure 5.1: Stokes number radial profile after 0.4 Myr. Inside the water snowline (located between $2.5 - 3.0$ au) the dust can grow only up to St $\sim 10^{-4}$. Outside the snowline it can reach values of St $\sim 10^{-2} - 10^{-1}$.

a traffic jam at the snowline location, as the small dry silicates drift slower than the large icy particles, which results in a higher concentration of dust in the inner regions. Outside the snowline the dust-to-gas ratio remains low, so the back-reaction from the large particles is not strong enough to perturb the gas. In this scenario, the gas surface density remains very close to the initial steady state.

Further effects can be seen in the "Mid ε_0" simulation (Figure 5.2, middle panel). First we notice an increment in the gas density profile at the snowline location, caused by the additional water vapor delivered by the icy grains (Ciesla & Cuzzi, 2006). The water vapor and the dust are also more concentrated towards the snowline in this case, as the higher dust-to-gas ratio damps more efficiently the viscous velocity ($|\bar{A}v_\nu| < |v_\nu|$), slowing the diffusion of both gas and small particles. At the same time, the additional water vapor also increases the gas pressure, which in turn also increases the drift velocity of the large icy particles towards the snowline, resulting in higher dust concentrations.

We also observe a small decrease in the gas surface density outside the snowline, caused by the dust back-reaction that slows down the gas velocity, reducing the supply to the inner regions. This effect becomes more pronounced for higher dust-to-gas ratios.

The back-reaction of dust onto the gas causes notorious perturbations in the "High ε_0" simulation (Figure 5.2, bottom panel). As in the "Mid ε_0" simulation, the solids also accumulate at the snowline location, but now the icy dust particles outside the snowline exert a stronger push onto the gas, and reverse the gas accretion of the outer regions. This results in a depletion of gas outside the snowline (between $r > 2.5$ au), reaching a minimum density of $\sim 50\%$ of its initial value.

Furthermore, the drop in gas density outside the snowline reduces the pressure gradient. Consequently, the drift speed of the large icy particles is also slowed down, allowing for an extended accumulation of dust in the outer regions. This process of gas depletion and dust

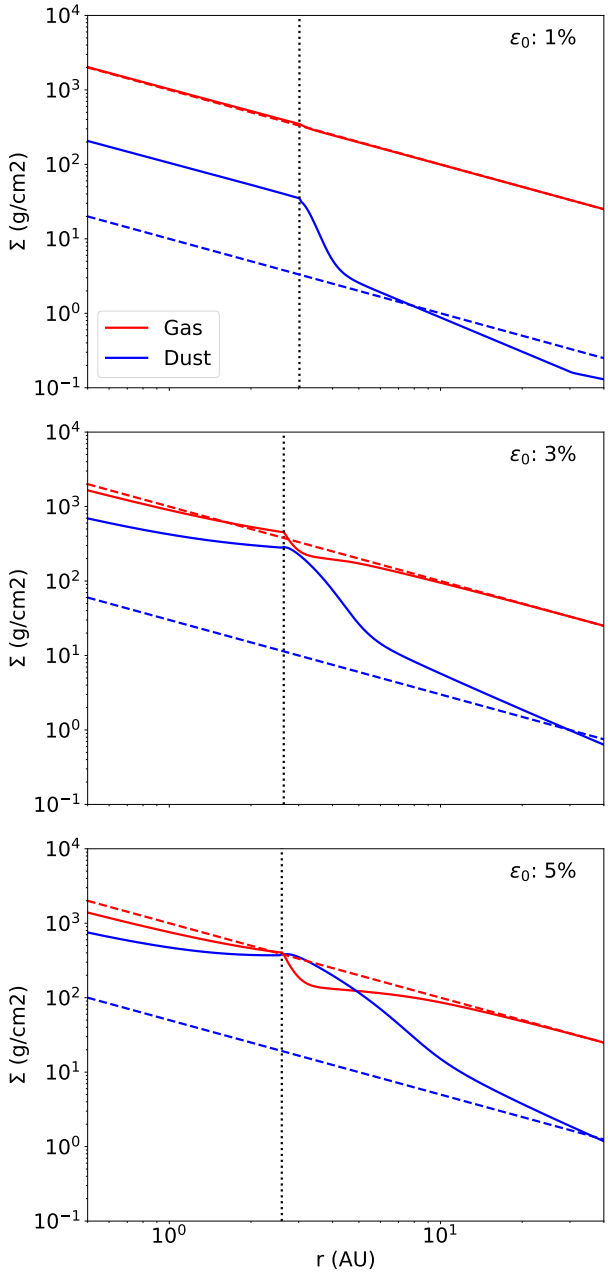

Figure 5.2: Surface density radial profiles of gas (red) and dust (blue) around the snowline. The dashed lines mark the initial conditions, and solid lines mark the simulation after 0.4 Myr. The dotted line marks the snowline at 0.4 Myr. The *top*, *middle*, and *bottom* panels correspond to the cases with "Low", "Mid", and "High" ε_0, respectively.

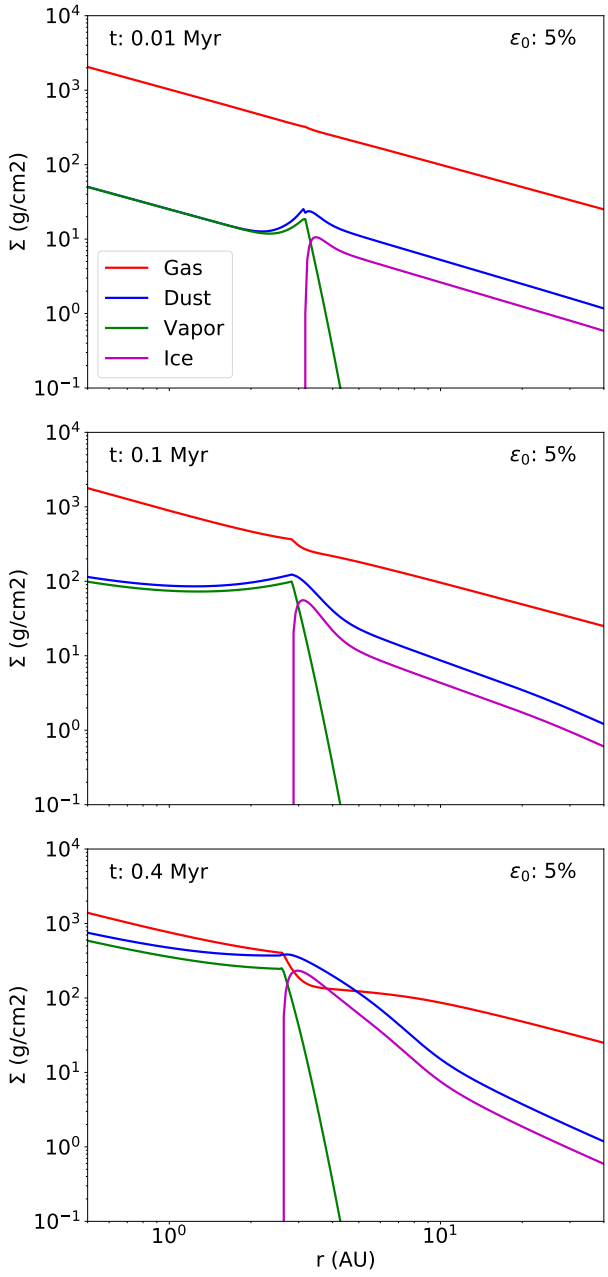

Figure 5.3: Surface densities of gas (red), dust (blue), vapor (green) and ice (purple) of the "High ε_0" simulation ($\varepsilon_0 = 0.05$), at different times. As time passes, dust accumulates around the snowline, and the gas surface density is perturbed by the back-reaction.

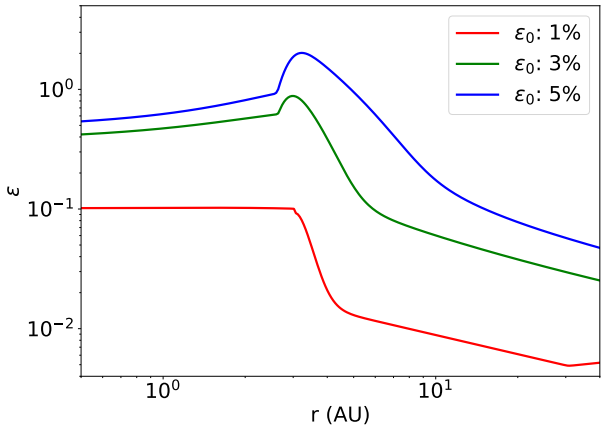

Figure 5.4: Dust-to-gas ratio radial profile for the three simulations after 0.4 Myr. The simulations with a high global dust-to-gas ratio ($\varepsilon_0 \geq 0.03$), shown an enhanced dust accumulation outside the snowline, reaching $\epsilon \approx 0.8 - 2.0$.

accumulation is expected to continue as long as dust is supplied from the outer regions. In the inner regions inside 1 au, the gas is depleted to $\sim 65\%$ of its initial value. Only the additional water vapor supplied by the dust crossing the snowline prevents a further depletion of gas. The evolution of this simulation is illustrated in Figure 5.3, where we can see the initial traffic jam caused by the change in particle size ($t = 0.01$ Myr), followed by a further concentration of solids once the vapor accumulates in snowline ($t = 0.1$ Myr), and finally the depletion of gas outside the snowline, accompanied by the extended accumulation of dust ($t = 0.4$ Myr).

From Figure 5.4 we see that the dust-to-gas ratios can reach extremely high values depending on the simulation parameters. The "Low ε_0" simulation reaches a concentration of $\epsilon \approx 0.1$ in the inner regions (where the particles are small), because of the traffic jam, but no further accumulation occurs outside the snowline.

In the "Mid ε_0" case, the dust-to-gas ratio reaches a high value of $\epsilon \approx 0.85$ at the snowline, and $\epsilon \approx 0.4$ at 1 au. The dust is more concentrated towards the snowline in this case because the back-reaction slows down the viscous diffusion (Equation 2.3), yet as time passes the dust should spread more evenly towards the inner regions.

The most extreme case is the "High ε_0" simulation, where the dust accumulates both inside and outside the snowline. The dust accumulates in the inner regions due to the traffic jam caused by the change in particle size and the pressure maximum caused by the water vapor, reaching concentrations between $\epsilon \approx 0.5 - 1.0$. Outside the snowline the dust back-reaction depletes the gas and reduces the pressure gradient, creating another concentration point between $2.5 - 4$ au where the dust-to-gas ratio reaches values of $\epsilon \approx 1.0 - 2.0$. The recondensation of vapor also contributes to enhance the concentration of solids outside the snowline (Drążkowska & Alibert, 2017; Stammler et al., 2017).

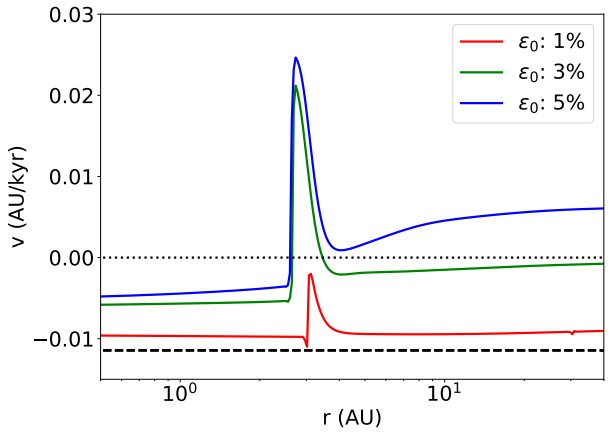

Figure 5.5: Radial gas velocities after 0.4 Myr (solid lines), and initial viscous velocity (dashed line). Outside the snowline, the dust back-reaction can stop, and even reverse the gas flux for the simulations with $\varepsilon_0 \geq 0.03$.

5.4.1 Accretion damped by the back-reaction

The radial velocity of the gas now depends not only on the viscous evolution, but also on the pressure gradient and the dust distribution (Equation 2.3 to 2.12). Therefore, for high dust-to-gas ratios and large particles sizes, the gas flow may be damped and even reversed. Figure 5.5 shows the gas velocities of the different simulations. In the "Low ε_0" simulation the dust-to-gas ratio is higher in the inner regions (where grain sizes are small), and lower at the outer regions (where particle sizes are large). This trade-off between concentration and size means that the dust back-reaction does not dominate the evolution of the gas, and that the gas velocity is only damped with respect to the steady state viscous velocity by a factor of a few.

The gas velocity is roughly $v_{\mathrm{g,r}} \approx 0.85\, v_\nu$ inside the snowline and $v_{\mathrm{g,r}} \approx 0.80\, v_\nu$ outside the snowline, where the transition is caused by the change in both particle size and dust-to-gas ratio.

This damping in the viscous velocity also leads into a similar decrease in the gas accretion rate onto the star, from $\dot{M} = 8 \times 10^{-9}\,\mathrm{M_\odot/yr}$ to $6.8 \times 10^{-9}\,\mathrm{M_\odot/yr}$ (Figure 5.6). Once the dust supply is depleted, the accretion rate should return to its steady state value.

In the "High ε_0" simulation, where the dust concentrations are high inside and outside the snowline, we can see the full effects of dust back-reaction. In the inner regions ($r < 2.5\,\mathrm{au}$) the particles are small ($\mathrm{St} \sim 10^{-4}$), so the gas velocity is dominated by the term $\bar{A} v_\nu$, which corresponds to the viscous velocity damped by a factor of $\bar{A} \approx (1+\epsilon)^{-1}$. In the outer region ($r > 2.5\,\mathrm{au}$) where the particles are large ($\mathrm{St} \gtrsim 10^{-2}$), the velocity is dominated by the pressure velocity term $2\bar{B} v_P$, which moves the gas outward, against the pressure gradient (Equation 2.3). This reversal of the gas velocity causes the observed depletion in the gas surface density. Figure 5.7 shows the damping and pushing terms of the gas velocity, to illustrate how the gas motion is affected by the dust back-reaction.

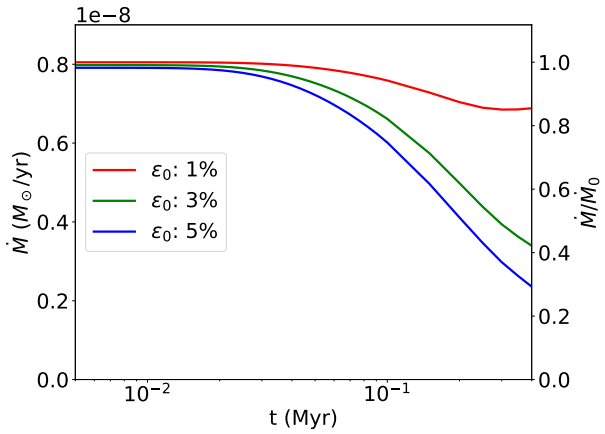

Figure 5.6: Gas accretion rate over time, measured at 0.5 au. The accretion rate decreases over time, dropping to a 85% of the initial value for the "Low ε_0" simulation, and to a $30\% - 45\%$ for the higher ε_0 cases.

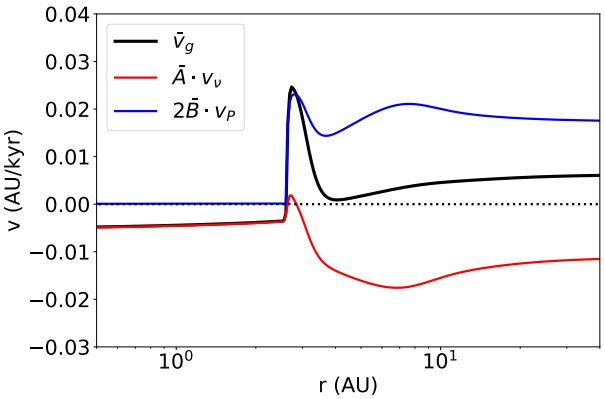

Figure 5.7: Gas velocity profile of the "High ε_0" simulation after 0.4 Myr (black), and the decomposition of the two velocity terms $\bar{A}v_\nu$ (red) and $2\bar{B}v_P$ (blue) (see Equation 2.3). In the inner regions the pushing term $2\bar{B}v_P$ is negligible, as the particles Stokes number is too small, and the total velocity is dominated by the damped viscous velocity $\bar{A}v_\nu$. In the outer regions the term $2\bar{B}v_P$ overcomes the viscous evolution, and pushes gas against the pressure gradient.

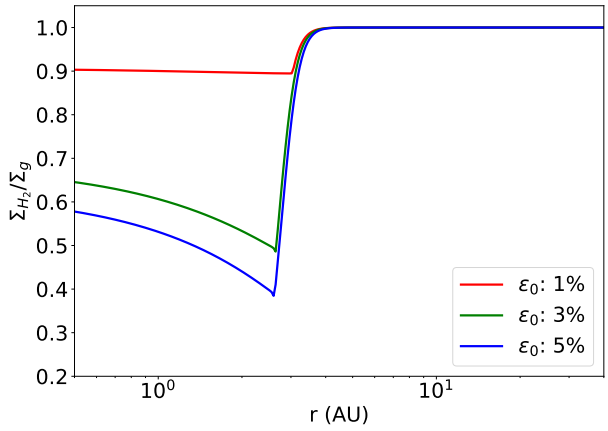

Figure 5.8: H_2, He mass fraction profile after 0.4 Myr. The mass fraction of light gases is lower inside the snowline as the dust crossing the snowline delivers water vapor. As the global dust-to-gas ratio increases, the back-reaction push outside the snowline reduces the flux of H_2, He into the inner regions.

Since the gas inner disk is disconnected from the outer disk at the snowline in terms of mass transport, the accretion rate into the star is considerably reduced. As solid particles accumulate around the snowline, and the inner regions become more and more depleted of gas, the accretion rate reaches a value as low as $\dot{M} = 2.5 \times 10^{-9}\,M_\odot/\mathrm{yr}$. The only reason why the gas is not further depleted in the inner regions is because of the water vapor delivered by the icy dust particles crossing the snowline (Ciesla & Cuzzi, 2006).
Meanwhile, the mass outside the snowline is transported outwards at a rate of $\sim 10^{-9} - 10^{-8}\,M_\odot/\mathrm{yr}$. No instabilities seem to appear in gas surface density in the outer regions, as the mass transported to the outer disk is only a small fraction of the total disk mass. Once the dust supply is exhausted the back-reaction push will stop being effective, and the gas accretion rate should retake the standard viscous evolution.
The behavior of the "Mid ε_0" simulation is consistently in between the "Low ε_0" and "High ε_0" cases, with that the gas flux is practically frozen ($v_{g,r} \approx 0$) in the outer regions ($r > 4\,\mathrm{au}$). All simulations show that the back-reaction push is particularly strong in a narrow region outside the snowline (between $r \approx 2.5 - 4\,\mathrm{au}$), where the concentration of icy particles increases because of the recondensation of water vapor.
In Section 5.5.3 we comment on the effects of dust settling on the accretion rate at different heights.

5.4.2 Depletion of H_2 and He inside the snowline.

From the gas velocities, we see that in the cases where the back-reaction is effective it can stop or reverse the accretion of gas outside the snowline, causing the inner regions to become relatively depleted of gas.

In particular, the dust back-reaction reduces the supply of the H_2, He to the inner regions, as outside the snowline this is the dominant gas component.
At the same time, the icy grains cross the snowline and deliver water vapor to the inner regions. Therefore, the gas will present a lower H_2, He mass fraction in the inner disk than in the outer disk.
The total amount of water delivered to the inner regions depends on the initial dust-to-gas ratio ϵ_0, while the dust back-reaction affects how it is distributed.
Figure 5.8 shows that even in the "Low ε_0" case, the mass fraction of H_2, He is reduced to a 90%.
For the "Mid ε_0" and "High ε_0" cases the dust back-reaction onto the gas reduces the supply of light gases to the inner regions, creating environments dominated by water vapor inside the snowline, with a H_2, He mass fraction between $40\% - 65\%$. The depletion is more concentrated towards the snowline because the damping term of the gas velocity ($\bar{A}\, v_\nu$) slows down the viscous diffusion of water vapor.
After the dust supply is exhausted, the region inside the snowline will be gradually refilled with gas from the outer regions in the viscous timescale ($t_\nu \approx 0.5\,\mathrm{Myr}$ at $4\,\mathrm{au}$), and the H_2, He mixture will be replenished to become the dominant component once more.

5.4.3 What happens without the back-reaction?

So far we have studied the impact on the dust back-reaction into the gas and dust density profiles, and in the gas velocity. So, how different is the situation when the back-reaction effect is ignored?
In Figure 5.9 we turn off the back-reaction effects ($v_{\mathrm{g,r}} = v_\nu$, $\Delta v_{\mathrm{g},\theta} = -v_P$), and ignore the collective effect of dust on its diffusivity ($D_\mathrm{d} = \nu$). The simulation with $\varepsilon_0 = 0.01$ shows only minor differences, corresponding to a faster dust accretion. This is an indication that for low dust-to-gas ratios the back-reaction onto the gas is not important.
For the simulations with $\varepsilon_0 \geq 0.03$ we observe that, without the back-reaction effect, the dust only concentrates in the inner regions due to the traffic jam caused by the change in particle sizes at the snowline. Accordingly, the water vapor delivered by the icy particles also increases the total gas content.
Figure 5.10 shows how the dust-to-gas ratio profile is affected by the dust back-reaction. Only when the back-reaction is considered the solid particles can pile up outside the water snowline, due to the perturbed pressure gradient and the slower dust motion. For the simulations with $\varepsilon_0 \geq 0.03$, the dust back-reaction increases the dust-to-gas ratio by over an order of magnitude outside the water snowline. This agrees with previous results of Drążkowska & Alibert (2017); Hyodo et al. (2019) where the dust back-reaction was incorporated as the collective drift of the dust species.

5.4.4 The importance of the disk profile and size.

How much the dust can perturb the gas surface density depends on the dust-to-gas ratio and the dust sizes, but also on how long the back-reaction is effectively acting.

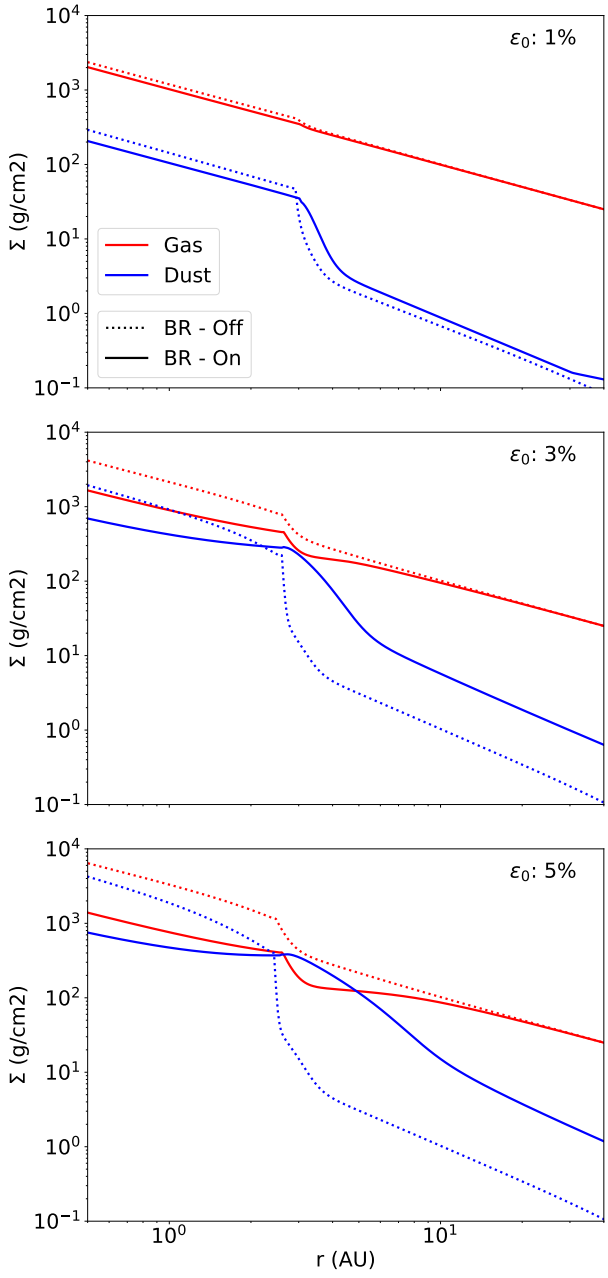

Figure 5.9: Comparison of the surface density profiles when the back-reaction is considered (solid lines) and ignored (dashed lines), after 0.4 Myr. For the cases with $\varepsilon_0 \geq 0.03$, the gas surface density is reduced when the back-reaction is considered in the inner regions, and the dust concentration is extended.

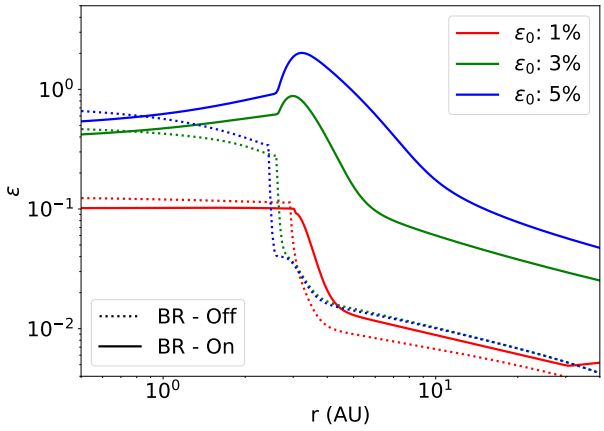

Figure 5.10: Comparison of the dust-to-gas ratio profiles when the back-reaction is considered (solid lines) and ignored (dashed lines), after 0.4 Myr. When the back-reaction is ignored, the dust accumulates only inside the snowline.

In the "High ε_0" case, the dust first creates a small depletion into the gas outside the snowline, the pressure slope changes and allows for large particles to further accumulate. Yet, this scenario assumes that icy particles are being constantly delivered towards the snowline, while in reality the supply has a limit given by the disk size.
We made a test simulation with $\varepsilon_0 = 0.05$ as in the "High ε_0" case, but this time starting with a self-similar profile (Lynden-Bell & Pringle, 1974), following:

$$\Sigma_g(r) = \Sigma_0 \left(\frac{r}{r_0}\right)^{-p} \exp(-r/r_c), \tag{5.9}$$

with a cut-off radius of $r_c = 100$ au.
From Figure 5.11 we can see the evolution of this simulation until 1 Myr. Though we still observe that dust accumulates at the snowline, reaching dust-to-gas ratios between $\epsilon = 0.7 - 0.8$, and that the back-reaction push still creates a small dip in the gas surface density outside the snowline, the supply of solids is not enough to perturb the gas over extended periods of time. In this disk of limited size, no extended dust accumulation outside the snowline is observed.
The effect that still remains present is the decrease of the accretion rate (Figure 5.12). As long as dust is delivered at the snowline, the accretion rate of gas is damped, and the mass fraction of the H_2, He mixture is decreased in the inner regions.
We find that between $0.4 - 0.5$ Myr the dust concentration reaches its maximum value at the snowline (roughly the time required for the dust in the outer regions to grow and drift through the disk), and the accretion rate reaches its minimum of $3.0 \times 10^{-9}\,M_\odot/yr$, where only 60% of the accretion flow corresponds to H_2, He.
After 1 Myr the dust is completely depleted, the disk surface density roughly recovers the self similar profile and the accretion rate rises back again.

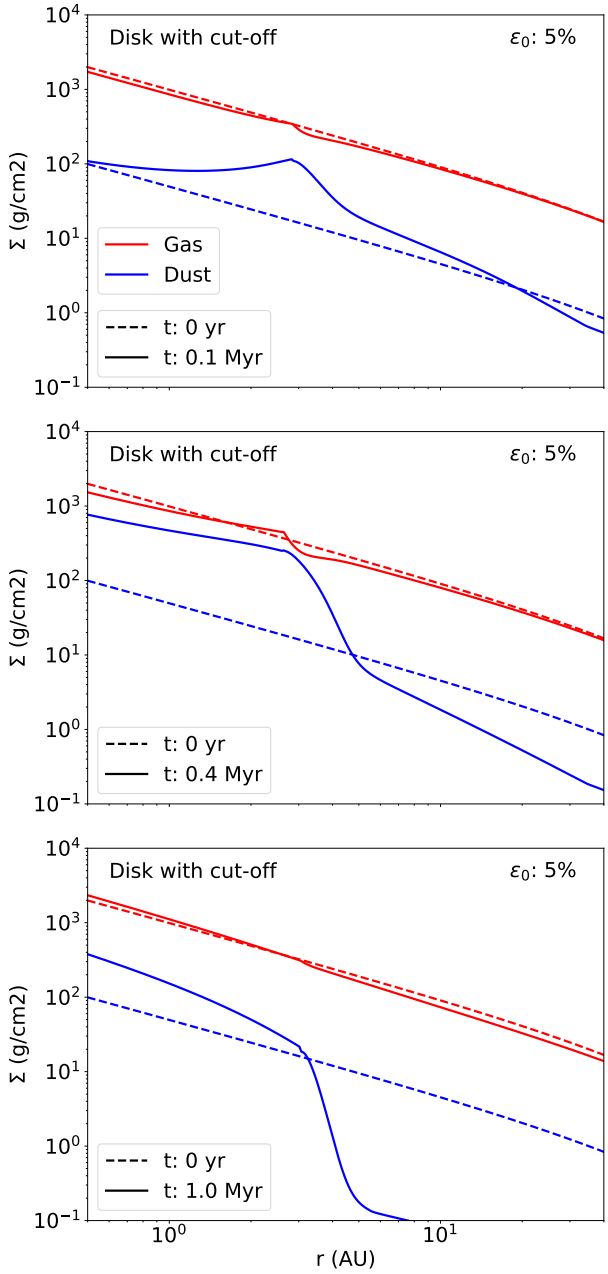

Figure 5.11: Surface density profiles of gas (red) and dust (blue) at different times (solid lines). The initial condition corresponds to the self-similar profile (dashed lines). *Top:* The simulation initially behaves in the same way as the power law profile until 0.1 Myrs. *Mid:* At 0.4 Myrs the dust supply gets exhausted before the back-reaction push can further deplete the gaseous disk. *Bottom:* After 1 Myr, the gas profile looks very similar to its initial condition, but most of the dust has been accreted.

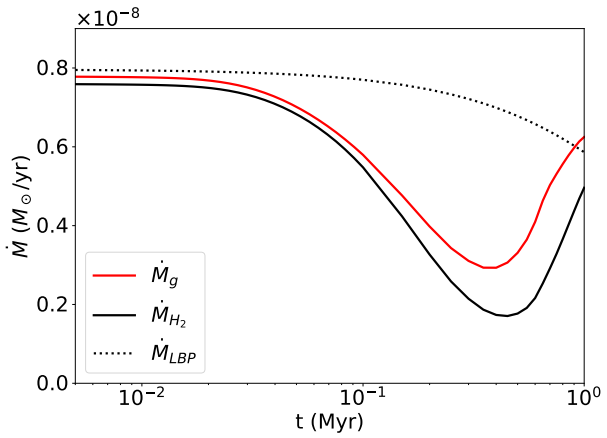

Figure 5.12: Accretion rate over time for the simulation with self-similar profile and $\varepsilon_0 = 0.05$. The gas accretion rate (red) decreases as the dust back-reaction damps gas velocity, and rises again after the dust is depleted. The accretion rate of H_2, He (black) is even lower, as the gas supply of the outer regions is reduced at the snowline. The accretion rate of the standard self-similar solution (dotted line) is plotted for comparison.

5.5 Discussion

5.5.1 When is dust back-reaction important?

So far we have seen that when the back-reaction is effective, it can enhance the dust concentration at the snowline (Figure 5.4), damp the gas accretion rate (Figure 5.6), and deplete the inner regions from hydrogen and helium (Figure 5.8).
All of these effects can be traced back to the push exerted by the dust back-reaction onto the gas (Equation 2.3), that reduces the pressure gradient (which enhances dust accumulation), and slows down the flux of material from outside the snowline to the inner regions.
As a rule of thumb, the gas dynamic is altered whenever the pressure velocity term is comparable to the damped viscous velocity ($\bar{A}v_\nu \sim 2\bar{B}v_P$, Equation 2.3), which occurs roughly when the particles have large Stokes number and high dust-to-gas ratios such that $\mathrm{St}\,\epsilon/(\epsilon+1) \sim \alpha$ (Kanagawa et al., 2017; Dipierro et al., 2018).
In an inviscid disk ($\alpha_\nu \approx 0$), the gas velocity is dominated by the term $2\bar{B}v_P$, and the gas moves against the pressure gradient (Tanaka et al., 2005). On the other side, if the disk is highly turbulent ($\alpha_\nu \gg \mathrm{St}\epsilon$), then the gas evolves with a damped viscous velocity $\bar{A}v_\nu$. In Appendix C we include an equivalent criterion to determine the effect of the back-reaction, based on the angular momentum exchange between the dust and gas.
Through this paper we found that a high global dust-to-gas ratio of $\varepsilon_0 \gtrsim 0.03$, and a low turbulent viscosity of $\alpha_\nu \lesssim 10^{-3}$ (see Appendix C of Gárate et al. (2020)), are necessary for the back-reaction push to perturb the combined evolution of gas and dust.
We also showed that the duration and magnitude of these effects depends on the disk size,

as the dust accumulation and the perturbation onto the gas stop once the solid reservoir is exhausted (Figure 5.11). In particular, for a disk with cut-off radius of $r_c = 100$ au the dust drifts from the outer regions to the snowline in 0.4 Myr. Afterwards, the back-reaction effects decay in a viscous timescale of the inner regions (roughly another 0.5 Myr).
Moreover, part of the dust accumulated at the snowline will be converted into planetesimals through streaming instability (Youdin & Goodman, 2005; Drążkowska & Alibert, 2017), which in turn will reduce the dust-to-gas ratio and smear out the back-reaction effects.
We should keep in mind however, that the results presented in this paper only occur if the snowline acts as a traffic jam for dust accretion, which is caused by the difference in the fragmentation velocities of dry silicates and icy aggregates. Yet, recent studies suggest that there is no difference between the sticking properties of silicates and ices (Gundlach et al., 2018; Musiolik & Wurm, 2019; Steinpilz et al., 2019), implying that the traffic jam should not form in the first place.

5.5.2 Other scenarios where the back-reaction might be important

Similar traffic jams and dust traps can occur in different regions of the protoplanetary disk. Given high dust concentrations and large particles sizes, the dust back-reaction may perturb the gas in locations such as dead-zones (Kretke et al., 2009; Ueda et al., 2019; Gárate et al., 2019), the outer edge of gaps carved by planets (Paardekooper & Mellema, 2004; Rice et al., 2006; Weber et al., 2018), and the edge of a photo-evaporative gap (Alexander & Armitage, 2007).
In numerical models of protoplanetary disks, the back-reaction effects should be considered when estimating the gas accretion rate (which is reduced by the interaction with the dust, Kanagawa et al., 2017), the planetesimal formation rate (which would be enhanced for higher dust concentrations, Drążkowska & Alibert, 2017), or the width of a dusty ring in the outer edge of a gap carved by a planet (Kanagawa et al., 2018; Weber et al., 2018; Drążkowska et al., 2019).
The effects of the back-reaction could actually become effective at later stages of the disk lifetime, provided that other mechanisms continue to trap the dust delivered from the outer regions, for example, if a planet forms from the planetesimal population at the water snowline (Drążkowska & Alibert, 2017), it would carve a gap that can effectively trap dust particles (Pinilla et al., 2012; Lambrechts et al., 2014), and create a new environment where the back-reaction can affect the gas and dust dynamics (Kanagawa et al., 2018).
On smaller scales the dust back-reaction triggers the streaming instability, locally enhancing the concentration of dust particles until the solids become gravitationally unstable (Youdin & Goodman, 2005), and close to the midplane the friction between layers of gas and dust results in a Kelvin-Helmholtz instability between the two components (Johansen et al., 2006).
Finally, one scenario that we did not cover in our parameter space is when the turbulence is so low ($\alpha_\nu = 0$) that the disk advection is reversed all the way to the inner boundary, which

could lead to further perturbations at the snowline location, though a proper treatment of the dust sublimation should be included to account for this scenario.
Among our results, we could not reproduce the accumulation of dust in the outer regions of the disk described by Gonzalez et al. (2017), as the dust particles drift towards the inner regions before creating any perturbation in the outer gas disk. We also find that by taking into account the growth limits, the back-reaction is less efficient than previously thought (Kanagawa et al., 2017), as the fragmentation barrier prevents the particles to grow to sizes beyond $\mathrm{St}_{\mathrm{frag}}$, and limiting the effect of the back-reaction even if the gas surface density decreases.
We do not expect our results to be significantly affected by changes in the disk mass or the stellar mass. Since particles sizes around the snowline are limited by the fragmentation barrier, the changes in any of these two parameters will only affect the physical size of the particles, but not their Stokes number (Equation 1.28) which controls the dynamical contribution of the particles to the gas motion. The timescales and the snowline location would change accordingly, but the qualitative results presented in this work should hold true.

5.5.3 Layered accretion by dust settling

Because large particles settle towards the midplane, the back-reaction push onto the gas can be stronger at the disk midplane than at the surface (Kanagawa et al., 2017), which can result in the upper layers flowing inward (unperturbed by the dust), while the inner layers flow outward (due to the dust back-reaction). Depending on the particle sizes, this might result in different accretion rates at different heights.
While our approach to treat the vertical structure traces correctly the net mass transport (Section 2.3) it does not provide information about layered accretion flow. To check if there is a substantial inflow of material at the upper layers, we calculate the accretion rate at every height (using the vertical model from Takeuchi & Lin (2002)) and measure the total mass inflow and outflow separately (Figure 5.13).
We find that inside the snowline ($r < 2.7\,\mathrm{au}$), where the dust particles are small ($\mathrm{St} \sim 10^{-4}$) and well mixed with the gas, the back-reaction damps the gas motion uniformly at all heights, and the total inflow is of $3.0 \times 10^{-9}\,\mathrm{M}_{\odot}/\mathrm{yr}$, only $6.0 \times 10^{-10}\,\mathrm{M}_{\odot}/\mathrm{yr}$ higher than the net accretion rate onto the star.
In the regions beyond the snowline dust accumulation ($r > 3.0\,\mathrm{au}$), we find that the accretion rate is layered, with the disk midplane flowing outward, while the surface layers move inward. The material inflow in this case is comparable to that of a dust free disk ($\dot{M} \sim 10^{-8}\,\mathrm{M}_{\odot}/\mathrm{yr}$), even if the net mass flux is positive. This is in agreement with the results of Kanagawa et al. (2017). For these regions, we find that the dust back-reaction can revert the gas flow up to $2h_{\mathrm{d}}$, which for the large dust particles at 3 au ($\mathrm{St} \sim 10^{-2}$) corresponds to $0.6h_{\mathrm{g}}$.
Interestingly, at the snowline location where the dust particles accumulate ($2.7\,\mathrm{au} < r < 3.0\,\mathrm{au}$), the dust back-reaction is strong enough to perturb the gas surface density. The steeper negative surface density slope found at the snowline causes the viscous accretion

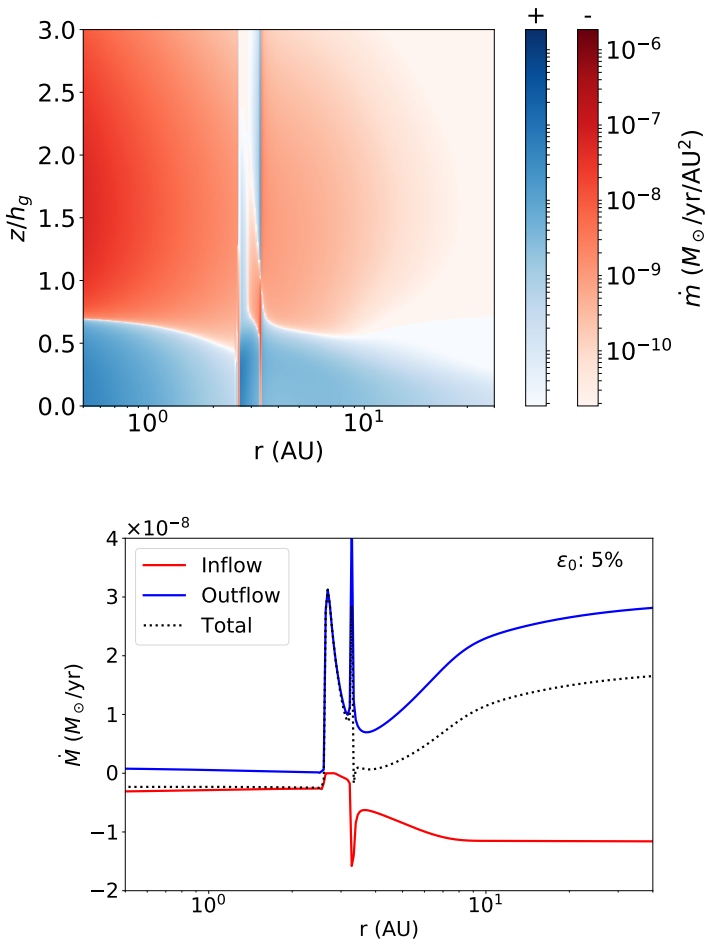

Figure 5.13: *Top:* Mass flux for the simulation with $\varepsilon_0 = 5\%$, in the radial and vertical direction, obtained using the Takeuchi & Lin (2002) vertical velocity profiles. The blue regions show the material outflow, and the red regions show the inflow. *Bottom:* Accretion inflow (red), outflow (blue), and the total mass accretion (dotted) profiles.

to be reduced or reversed at all heights (Takeuchi & Lin, 2002). The accretion inflow is then reduced to a value of $\dot{M} = 8.0 \times 10^{-10}\,\mathrm{M}_\odot/\mathrm{yr}$ for the simulation with $\varepsilon_0 = 0.03$ (in which the reduced inflow only occurs above $0.7h_\mathrm{g}$), and to $\dot{M} = 6 \times 10^{-12}\,\mathrm{M}_\odot/\mathrm{yr}$ for the simulation with $\varepsilon_0 = 0.05$, where the inflow only occurs $2.5h_\mathrm{g}$ above the midplane.
The steepening of the surface density slope at the water snowline was not observed in the previous results of Kanagawa et al. (2017) as they did not include the snowline or a dust growth and recondensation model. We find that this perturbation caused by the dust accumulation at snowline is key to reduce or stop the accretion inflow over a wide vertical range, which can be larger than the dust scale height itself.
Given that the disk mass inside the snowline is of $2.0 \times 10^{-3}\,\mathrm{M}_\odot$, the composition of the gas phase described in Section 5.4.2 should be corrected for the material flowing from the outer disk into the inner regions. For the simulation with $\varepsilon_0 = 0.03$ the $H_2 + He$ ratio should be higher by a 20%, considering that the inflow is reduced by over an order of magnitude at the snowline location (though not completely stopped). For the simulation with $\varepsilon_0 = 0.05$ all our results hold.

5.5.4 Observational Implications

The perturbation caused by the dust back-reaction at the snowline is only effective if the turbulent viscosity is low, if the dust-to-gas ratio is high, and only acts at early times of the disk evolution, while dust is supplied towards the inner regions. Given these constraints, we want to find which disk properties would fit in this parameter space, and what signatures we can expect to find if the back-reaction is effectively perturbing the gas.

Ideal targets

Young Class 0 and Class I disks seem to have typical sizes around 100 - 200 au (Najita & Bergin, 2018, Table 1), so solids can be delivered to the inner regions only until $0.5-1\,\mathrm{Myr}$, before the disk is depleted of dust (unless a pressure bump prevents particles from moving towards the star). This means that older disks ($t > 1\,\mathrm{Myr}$) are unlikely to present any perturbation from the back-reaction push.
Then, among young disks and assuming viscous accretion, only those with low accretion rates of:

$$\dot{M} \lesssim 10^{-8}\,\mathrm{M}_\odot/\mathrm{yr} \left(\frac{M_\mathrm{disk}}{0.1\,\mathrm{M}_\odot}\right) \left(\frac{r_c}{100\,\mathrm{au}}\right)^{-1} \left(\frac{M_\mathrm{star}}{\mathrm{M}_\odot}\right)^{-1/2} \left(\frac{T_0}{300\,\mathrm{K}}\right), \tag{5.10}$$

could be subject to the back-reaction damping, as a low viscous evolution ($\alpha_\nu \lesssim 10^{-3}$) is required for the dust to affect the gas. In terms of the dimensionless accretion parameter introduced by Rosotti et al. (2017), defined as:

$$\eta = \frac{\tau \dot{M}}{M_\mathrm{disk}}, \tag{5.11}$$

a disk of age τ would require $\eta \lesssim 0.1$ for the dust back-reaction to effectively perturb the gas.

On the gas orbital velocity

If the concentration of dust in any region is high, then the gas pressure support is reduced and the orbital velocity approaches to the keplerian velocity v_K (Equation 2.4).
At the midplane, where large grains concentrate, the gas motion deviates from the keplerian velocity by:

$$\Delta v_{g,\theta} \approx -\frac{v_P}{1 + \max(1, \sqrt{\mathrm{St}/\alpha_t}) \cdot \epsilon}, \tag{5.12}$$

where the $\sqrt{\mathrm{St}/\alpha_t}$ factor measures the concentration of large particles at the midplane by settling (see Section 2.3). If in our disk the initial pressure velocity around the snowline was $v_P \approx 2 \times 10^{-3} v_K$, then the dust back-reaction and the accumulation of water vapor makes the gas orbit at velocities of $\Delta v_{g,\theta} \approx 7 \times 10^{-4} v_K$. At 2.7 au, where the snowline is located in our simulations, this correspond to a difference from the keplerian velocity of approximately $\Delta v_{g,\theta} \approx 10\,\mathrm{m/s}$.
We expect that in future observations, the deviations from the keplerian velocity could be used to constrain the dust content. Teague et al. (2018) already showed that the deviations from the keplerian velocity can be used to kinematically detect a planet, reaching a precision of 2 m/s. Better characterizations of the orbital velocity profiles in dust rings may then be used to differentiate between a planet perturbation and a dust back-reaction perturbation, based on the profile shape.
Unfortunately, the spatial resolution required to observe this variation is less than 10 mas, for a disk at a distance of 100 au and a snowline at 3 au from the star, and next generation instruments would be required. The velocity deviation could be easier to detect for disks around Herbig stars where the snowline is located at larger radii.

Shadows casted by dust accumulation

A recent study of Ueda et al. (2019) showed that dust can accumulate at the inner edge of a dead zone (a region with low ionization and low turbulence, Gammie, 1996), and cast shadows that extend up to 10 au.
We notice that our accumulation of dust at the snowline is similar to the dead zone scenario, in the sense that high dust-to-gas ratios are reached in a narrow region of the inner disk (Figure 5.4). Therefore, we hypothesize that similar shadows could be found in the regions just outside the snowline if enough dust is present. Still, radiative transfer simulations would be needed to determine the minimum dust-to-gas ratio necessary to cast a shadow.

Effects of the snowline traffic jam

The fast drift of the icy particles particles and the traffic jam at the snowline results in the accumulation of both small silicate dust and water vapor inside the snowline, even if the effect of the dust back-reaction is ignored (see Figure 5.9 and 5.10).
We find that if the initial dust supply is large enough (high ϵ_0 and large disk size), then during the early stages of the disk evolution ($t \lesssim 1\,\mathrm{Myr}$) we can expect the material

accreted into the star to be rich in silicates and refractory materials carried by the dust (see Figure 5.4), rich in oxygen (which is carried by the water vapor), and relatively poor in hydrogen, helium, and other volatile elements mixed with the gas outside the water snowline (see Figure 5.8), such as nitrogen and neon. The X-ray emission could provide estimates of the abundance ratios in the accreted material (Günther et al., 2006), though the coronal emission of neon in young stars could mask some of these abundances (H. M. Günther, private communication).
The increased concentration of water vapor in the warm inner regions would also enhance the emission from the water rotational lines. These lines have been already detected in different disks (Carr & Najita, 2008; Salyk et al., 2008) in the mid-IR with Spitzer IRS, and could be further observed in the future using Mid-Infrared Instrument at the James Webb Space Telescope (MIRI, Rieke et al., 2015).
Additionally, the excess of water should lead to low C/O ratios inside the snowline for young protoplanetary disks (Öberg et al., 2011; Booth & Clarke, 2018).

5.6 Summary

In this study we included the effects of the dust back-reaction on the gas in a model of the water snowline, which is known to act as a concentration point for dust particles due to the change in the fragmentation velocity between silicates and ices, and the recondensation of water vapor into the surface of icy particles (Drążkowska & Alibert, 2017).
Our model shows how the dust back-reaction can perturb the gas dynamics and disk evolution, though the parameter space required for this to happen is limited.
In the vicinity of the snowline, provided that the global dust-to-gas ratio is high ($\varepsilon_0 \gtrsim 0.03$) and the viscosity low ($\alpha_\nu \lesssim 10^{-3}$), the effects of the dust back-reaction are:

- Revert the net gas flux outside the snowline.
- Reduce the gas inflow at the snowline by over an order of magnitude.
- Damp the gas accretion rate onto the star to a $30\% - 50\%$ of its initial value.
- Reduce the hydrogen-helium content in the inner regions, and concentrate water vapor at the snowline.
- Concentrate solids at the snowline reaching dust-to-gas ratios of $\epsilon \gtrsim 0.8$.

These effects build up as long as dust is supplied from the outer disk into the snowline, with the duration set by the growth and drift timescale of the outer regions. After the dust reservoir is exhausted, the back-reaction effects decay in the viscous timescale of the inner regions. For a disk with size $r_c = 100\,\mathrm{au}$, we find that dust accumulates only during the first 0.4 Myr, and that the perturbation onto the gas has disappeared by the age of 1 Myr. The high dust-to-gas ratios required to trigger the back-reaction effects, and the traffic jam at the snowline, can result in an enhanced water content in the inner regions, in the

accretion onto the star to be enriched with refractory materials and oxygen, and perhaps a shadow to be casted outside the snowline location by the accumulation of dust particles. Other types of dust traps could present similar behaviors, though each case must be revisited individually to evaluate the magnitude of the perturbation of the back-reaction into the gas velocity.

Chapter 6

Distinguishing the origin of a dust ring. Photo-evaporation or planet?

The contents of this chapter are being prepared for submission to the Astronomy & Astrophysics Journal.

In this chapter we describe the implementation and preliminary results of the evolution of a gas disk considering either the mass loss due to photo-evaporation or the gravitational effects due to the presence of a planet.
We will focus this chapter on the implementation of both ingredients, the effects of the back-reaction on the dust distribution, and propose our scientific question: Can we distinguish a gap carved by a planet from a gap carved by photo-evaporation?

6.1 Motivation

After the first images of gaps and rings where obtained by ALMA Partnership et al. (2015), the question that soon followed was: Are all the gaps carved by planets (Gonzalez et al., 2015), for which the answer is "not necessarily".
The reason why planets are a popular straightforward answer, and a good starting point, is because they can form in short timescales, and can be found through a wide range of orbital radii (as shown by our own solar system and the exoplanet data). This makes them a candidate mechanism to create rings and gaps at different locations, and at any stage of the disk lifetime.
However, other mechanisms can also create axissymetric sub-structures, for example: ice-lines (Stammler et al., 2017), dead zones (Pinilla et al., 2016), and photo-evaporation (Alexander et al., 2006a,b).
To be able distinguish between mechanisms we need accurate models for each of them, a good understanding of the conditions in which these operate, and what characteristics does their final dust distribution exhibit.
In Section 1.1 we described how photo-evaporation can clear a gap, which results in a pres-

sure maximum at the outer edge of the cavity. As we have discussed previously, pressure maximums act as dust traps where large grains accumulate, creating ring like structures (Whipple, 1972; Weidenschilling, 1977). Now, in this chapter we address the effect of photo-evaporation in the collective the gas and dust evolution.
An accurate model of photo-evaporation would then allow us to predict the expected dust distribution in a protoplanetary disk, and to fit observations that display similar characteristics (for example, an inner gap and a dust ring). This way, we can complement other indicators of photo-evaporation, such as the comparison of the gas accretion rate with the mass loss (Ercolano et al., 2017).
In contrast with previous models (Alexander et al., 2006a,b; Alexander & Armitage, 2007; Owen & Kollmeier, 2019), our simulations include particle growth by solving the coagulation equation, the collective evolution of gas and dust including the dust back-reaction, which should allow us to get an accurate prediction for the resulting dust distribution (see Section 3.4), the new X-ray photo-evaporation model from Picogna et al. (2019), and the dust mass loss rate which takes into account the entanglement of small particles to the gas flow (Franz et al., 2020).
An application of this study would be to compare the dust distributions from a photo-evaporation model against an embedded planet model, and answer which of the two provides the best fit to an observation, and which specific signatures we could find in both cases. For example we could try to characterize the extend of a dust ring, its optical depth, or the depletion of the inner disk.
In this chapter we will take a preliminary step, and compare the dust distributions from two self-consistent simulations, using the code `DustPy` (Stammler and Birnstiel, in prep.) In the following sections 6.2 and 6.3 we describe the implementation of both the photo-evaporative mass loss and the planet torque, and in Section 6.4 we show comparisons between these two models.

6.2 Implementation of photo-evaporation

In our model, the photo-evaporation due to stellar irradiation is implemented as a mass loss term in the mass transport equation of gas and dust (1.1 and 1.16). In this section we describe the expression used for the mass loss rate for both components, following the work of Picogna et al. (2019) and Franz et al. (2020).

6.2.1 Gas loss rate

For the gas we implement the surface density mass loss profile derived by Picogna et al. (2019) from a two dimensional model (radial and co-latitude) that combines the temperature profile obtained from a radiative transfer calculation (Ercolano et al., 2003, 2005, 2008) and a hydrodynamic simulation using PLUTO (Mignone et al., 2007).
The mass loss rate was calculated considering the X-Ray radiation pressure of a star with mass $M_* = 0.7 M_\odot$, and a disk with a mass ratio of $M_{\rm disk}/M_* = 0.01$.

The density mass loss rate for the gas is then given by:

$$\dot{\Sigma}_{\mathrm{g,w}}(r\,[AU]) = \left(\frac{6a\ln(r)^5}{r\ln(10)^6} + \frac{5b\ln(r)^4}{r\ln(10)^5} + \frac{4c\ln(r)^3}{r\ln(10)^4} + \frac{3d\ln(r)^2}{r\ln(10)^3} + \frac{2e\ln(r)}{r\ln(10)^2} + \frac{f}{r\ln(10)}\right) \ln(10)\frac{\dot{M}_{\mathrm{w}}}{2\pi r}\,[M_\odot\,\mathrm{AU}^{-2}\,\mathrm{yr}^{-1}], \tag{6.1}$$

with

$$\dot{M}_{\mathrm{w}}(r\,[AU]) = \dot{M}(L_X)10^{a\log_{10}(r)^6+b\log_{10}(r)^5+c\log_{10}(r)^4+d\log_{10}(r)^3+e\log_{10}(r)^2+f\log_{10}(r)+g}, \tag{6.2}$$

and the constants $a = -0.5885$, $b = 4.3130$, $c = -12.1214$, $d = 16.3587$, $e = -11.4721$, $f = 5.7248$, $g = -2.8562$. In Equation 6.1 and 6.2 the stellocentric radii given in AU, see Picogna et al. (2019) for more details. An expression for the integrated mass loss rate as a function of the stellar X-ray luminosity $\dot{M}(L_X)$ is described in Picogna et al. (2019), however during development we will restrict ourselves to a single luminosity of $L_X = 10^{30}$ ergs/s, which corresponds to a total mass loss of $\dot{M}(L_X) \approx 10^{-8}\,\mathrm{M}_\odot/\mathrm{yr}$.

6.2.2 Dust loss rate

From our understanding of dust dynamics, we know that solid grains couple to the gas motion depending on their size. Therefore, it is to be expected that if part of the gas is blown away due to photo-evaporation, a fraction of the dust will also be entangled into the photo-evaporative wind (Owen & Kollmeier, 2019; Franz et al., 2020).
We implement the dust loss rate into `DustPy` in the following way:

- We assume that the gas and dust vertical structure follow a gaussian profile characterized by the scale heights h_{g} and h_{d}, as described in Section 1.5.
- We assume that most of the photo-evaporative flow comes from the upper layers of the disk, above a height $h \geq h_{\mathrm{ph}}$.
- We assume that only small grains, with $a \leq a_{\mathrm{ph}}$ are entangled with the gas.
- We calculate the dust-to-gas ratio $\epsilon_{\mathrm{ph}}(a)$ of entangled dust grains ($a \leq a_{\mathrm{ph}}$), above the photo-evaporation height h_{ph}.

With this information we can calculate the dust loss rate profile of a given particle size as:

$$\dot{\Sigma}_{\mathrm{d,w}}(a) = f_{\mathrm{ph}}(a)\epsilon_{\mathrm{ph}}(a)\dot{\Sigma}_{\mathrm{g,w}}, \tag{6.3}$$

where the $f_{\mathrm{ph}}(a)$ is a dimensionless factor that can then be used to correct for the efficiency of the entanglement depending on the particle size. For initial tests we set $f_{\mathrm{ph}} = 1.0$, $h_{\mathrm{ph}} = h_{\mathrm{g}}$, and $a_{\mathrm{ph}} = 15\mu m$. The entanglement particle size was set based on the the results of Franz et al. (2020), and we expect to calibrate the other free parameters accordingly.

6.3 Implementation of a planet torque

To implement the gravitational effect of a planet embedded into a gas disk we include an additional force term in the momentum equations described in Section 2.1, that acts on both the gas and dust components.
Due to the 1-dimensional nature of our model, we can only consider the azimuthally averaged torque exerted by the planet on the protoplanetary disk, as in Armitage & Natarajan (2002); Fontecilla et al. (2017). This method emulates the gap opening due to the planet gravity, but misses the spiral wakes that should be caused by the Lindblad resonance (Goldreich & Tremaine, 1979; Lin & Papaloizou, 1979, 1993; Bryden et al., 1999; Bae & Zhu, 2018).
The azimuthal torque exerted by a planet with orbital radii r_p, onto a parcel of gas located at a radii r can be written as:

$$\Lambda = \begin{cases} -\frac{1}{2} f q^2 \Omega_K^2 r^2 \left(\frac{r}{\Delta}\right)^4 & r < r_p \\ \frac{1}{2} f q^2 \Omega_K^2 r^2 \left(\frac{r_p}{\Delta}\right)^4 & r > r_p, \end{cases} \tag{6.4}$$

where $f \approx 10^{-2}$ is a dimensionless correction factor (used to fit the gap width, Armitage & Natarajan, 2002), $q = M_p/M_*$ is the planet-to-star mass ratio, $\Delta = \max(r_H, h_\mathrm{g}, |r - r_p|)$, is the maximum between the Hill's radius, the gas scale height, and the radial distance between the parcel of gas and the planet.
The hill sphere, which corresponds to the region in which motion of dust and gas is locally dominated by planet instead of the star, is defined as by the radius:

$$r_H = r_p \left(\frac{q}{3}\right)^{1/3}. \tag{6.5}$$

The planet torque is included in the momentum equations 2.1 and 2.2 as a force term $f_q \hat{\theta} = \Lambda / r\, \hat{\theta}$. Solving the momentum equations as in Appendix A, we arrive to the following gas and dust velocities:

$$v_{\mathrm{g},r} = A v_\nu + 2B v_P + v_q, \tag{6.6}$$

$$\Delta v_{\mathrm{g},\theta} = \frac{1}{2} B v_\nu - A v_P, \tag{6.7}$$

$$v_{\mathrm{d},r} = \frac{1}{1+\mathrm{St}^2} v_{\mathrm{g},r} + \frac{2\mathrm{St}}{1+\mathrm{St}^2} \Delta v_{\mathrm{g},\theta} + \frac{\mathrm{St}^2}{1+\mathrm{St}^2} v_q, \tag{6.8}$$

$$\Delta v_{\mathrm{d},\theta} = \frac{1}{1+\mathrm{St}^2} \Delta v_{\mathrm{g},\theta} - \frac{\mathrm{St}}{2(1+\mathrm{St}^2)} v_{\mathrm{g},r} + \frac{\mathrm{St}}{2(1+\mathrm{St}^2)} v_q, \tag{6.9}$$

where the additional velocity term due to the planet torque is defined as:

$$v_q = \frac{2\Lambda}{\Omega_K r}. \tag{6.10}$$

It is interesting to notice that we can also rewrite the gas and dust radial velocities as:

$$v_{\mathrm{g/d},r}(q) = v_{\mathrm{g/d},r}(q=0) + v_q, \tag{6.11}$$

which means that to obtain the gas/dust radial velocities considering the planet torque, it is only necessary to calculate the gas/dust radial velocities without the planet torque (as in Equation 2.3 and 2.5), and add the velocity component v_q. This implementation is particularly convenient for 1-dimensional simulations. The additional advection term due to the planet torque is then included into the mass transport equations for gas and dust (1.1 and 1.16) in `Dustpy`.
While this implementation of the planet torque has the advantage that it allow us to evolve both the gas and dust simultaneously, along with the dust growth model, it fails to capture the 2-dimensional asymmetries that the planet gravity causes in the disk, including the dust concentration at the spiral arms of the disk (Cuello et al., 2019b).

6.4 Early results

In this section we seek to get an intuition of the back-reaction effects onto a ring formed by a planet and by a photo-evaporative gap, and to compare both types of simulations.
We use a common setup for these simulations using a self-similar initial profile for the gas surface density (Equation 1.11). The rest of the common simulation parameters are described in Table 6.1 and Table 6.2.

Parameter	Value	Description
M_*	$0.7\,M_\odot$	Stellar mass
M_{disk}	$0.01 M_*$	Disk mass
T_0	150 K	Temperature at r_0
r_0	1 AU	Normalization radius
r_c	60 AU	Cut-off radius
α_ν	10^{-3}	turbulent viscosity
α_t	10^{-3}	Dust turbulence
v_{frag}	$1000\,\mathrm{cm\,s^{-1}}$	Fragmentation velocity
μ	2.3	Gas mean molecular weight
a_0	1 μm	Dust initial size
ρ_s	1.6 g cm^{-3}	Dust material density
ε_0	0.015	Initial dust-to-gas ratio

Table 6.1: Fiducial parameters for the numerical model.

6.4.1 Back-reaction effects on a planet induced ring.

We run a protoplanetary disk simulation using the parameters described above, including an embedded planet following the equations described in Section 6.3. The planet-to-star

Parameter	Value	Description
n_r	150	Number of radial grid cells
n_m	113	Number of mass grid cells
r_{in}	4 AU	Radial inner boundary
r_{out}	200 AU	Radial outer boundary
m_{min}	10^{-12} g	Dust mass lower limit
m_{max}	10^{4} g	Dust mass upper limit

Table 6.2: Grid parameters for the numerical model.

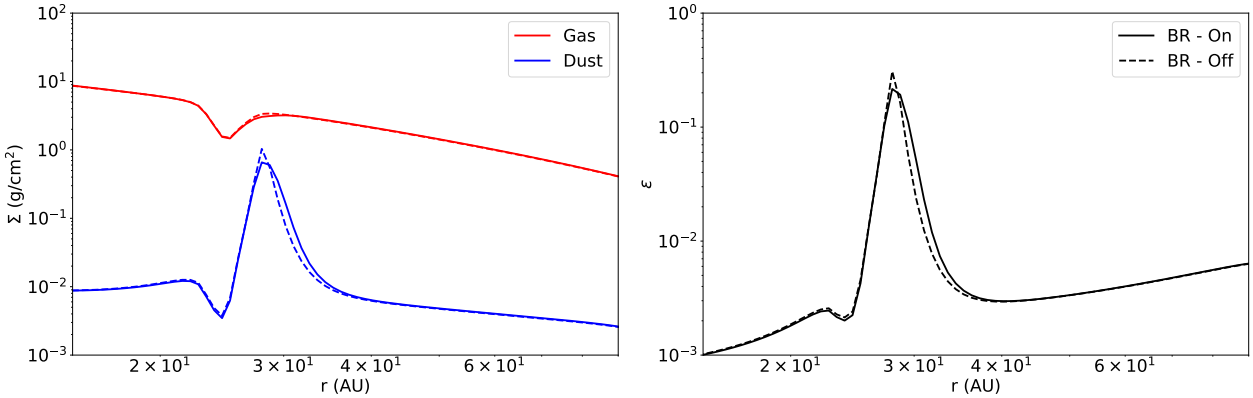

Figure 6.1: *Left:* Surface density profiles for the gas (red) and dust (blue), for the cases with and without back-reaction (solid and dashed lines, respectively), for a simulation with an embedded planet, after 0.16 Myrs. *Right:* Dust-to-gas ratio profiles.

mass ratio is $q = 10^{-3}$, and the orbital radius is $r_p = 25$ AU.
In Figure 6.1 we measure the effects of the back-reaction for an initial global dust-to-gas ratio of $\varepsilon_0 = 0.015$. The simulations show that the dust accumulates in a ring located at 28 AU.
The effect of the dust back-reaction appears to be almost negligible in this situation, and its effects are limited to reduce maximum dust-to-gas ratio at the ring from $\epsilon = 0.3$ to $\epsilon = 0.2$, and to spread the ring outer boundary approximately by 0.7 AU.
This spread seems to be in agreement with the comparison presented in Drążkowska et al. (2019), for a similar situation. Our results also agree qualitatively with the spread shown by Kanagawa et al. (2018), however (as discussed in Chapter 5 and Gárate et al., 2020) the magnitude of the back-reaction spreading is much lower, since the fragmentation limit prevents the particles from reaching sizes where their dynamics can significantly perturb the gas at these concentrations.
These subtle changes due to the back-reaction are unlikely to be detected in observations, as the resolution required would be too high, and there is no clear comparison point to measure against.
For planets located further away, the ring spreading might be proportionally increased, but

it is also necessary to consider that the total dust reservoir would be smaller, decreasing the back-reaction dynamical effects.
For now it seems safe to ignore the back-reaction in the modeling of a ring caused by a planet, assuming that the global dust-to-gas ratio does not exceed the typical ISM values.

6.4.2 Back-reaction effects on a photo-evaporation induced ring.

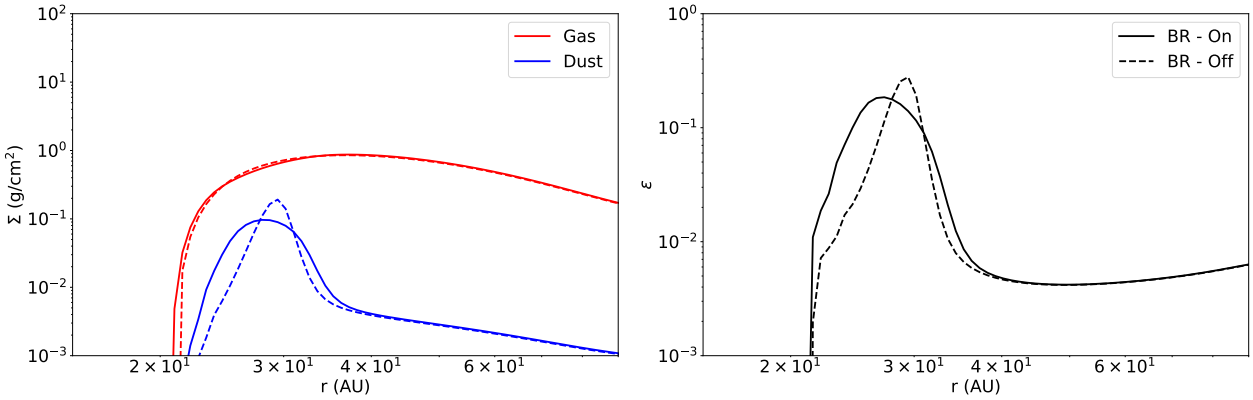

Figure 6.2: *Left:* Surface density profiles for the gas (red) and dust (blue), for the cases with and without back-reaction (solid and dashed lines, respectively), for a simulation of a photo-evaporative disk, after 0.16 Myrs *Right:* Dust-to-gas ratio profiles.

We run a protoplanetary disk simulation using the parameters described above, considering the photo-evaporation from the central star, implemented following Section 6.2 and Picogna et al. (2019). We consider that the integrated mass loss rate due to X-ray emission is $\dot{M}(L_X) = 3 \times 10^{-8}\,\mathrm{M}_\odot/\mathrm{yr}$.
In these simulations, the mass loss due to photo-evaporation is high in comparison with the disk accretion rate. This means that from the very beginning of the simulation the photo-evaporation has the potential to open a gap, and does so after ~ 0.1 Myrs from the start of the simulation. While this may not necessarily be the case in a real disk, we can interpret our initial condition as a disk which has already undergone significant viscous evolution, allowing us to reduce the computing time to observe the photo-evaporation effects.
From Figure 6.2 we observe that the dust back-reaction acts as described in Section 3.4, by radially spreading the dust ring and reducing the maximum dust concentration from $\epsilon = 0.27$ to $\epsilon = 0.18$. The width of the ring (measured from the dust-to-gas ratio profile at the base concentration of $\epsilon = 0.015$, expands from 9 AU (without back-reaction) to 12 AU (with back-reaction).

6.4.3 Comparison between ring types

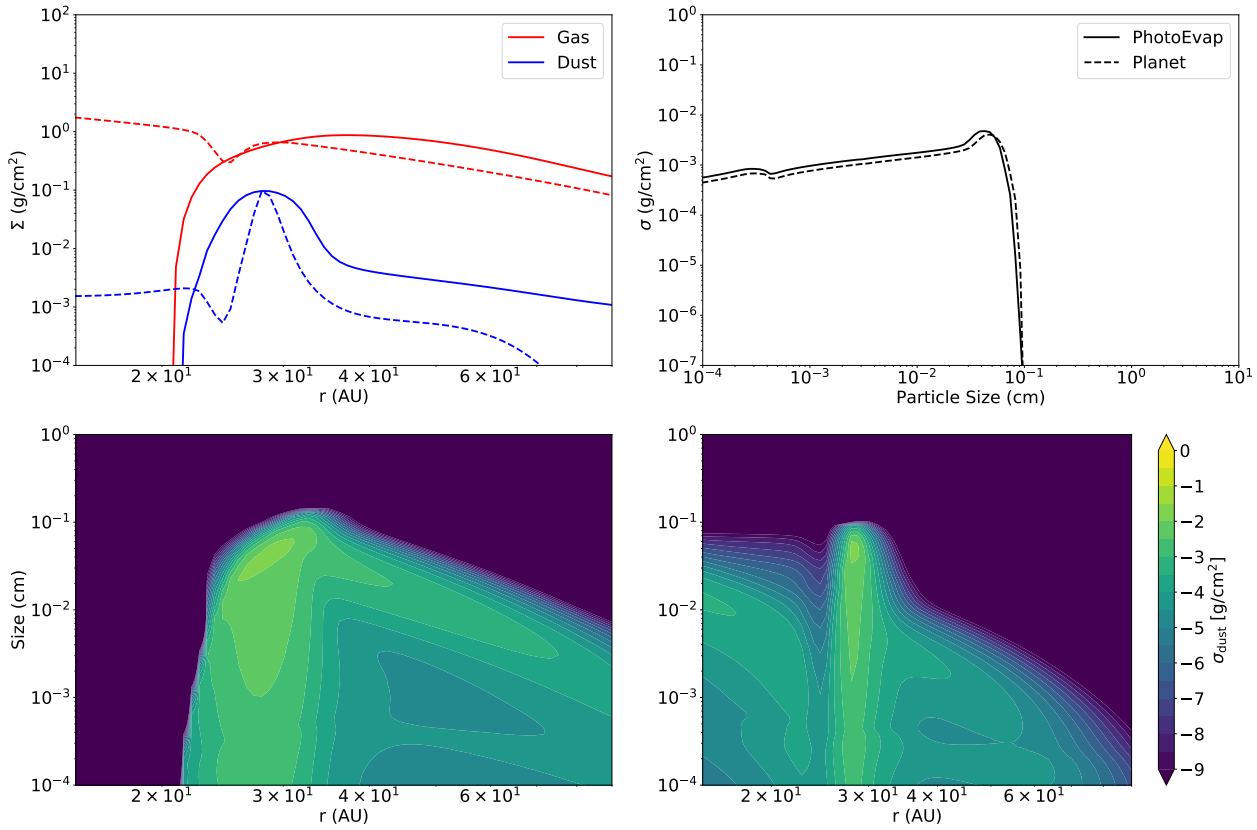

Figure 6.3: *Top Left:* Surface density profiles for the gas (red) and dust (blue), for the rings created by photo-evaporation (solid) and by a planet (dashed). *Top Right:* Dust size distribution at the ring location at 28 AU. *Bottom*: Dust distribution for the photo-evaporative (left) and planet (right) simulations. The initial disk mass was scaled down for the planet simulation, so that the gas density profiles and dust distributions would be comparable after , after 0.16 Myrs.

From the previous results we would like to know if we can tell apart a dust ring caused by a planet, from one caused by photo-evaporation. In Figure 6.3 we show the surface density and dust size distributions for both planet and photo-evaporative simulations, considering the back-reaction effects.
In order for the disks to be comparable, we reduced the disk mass by a factor of 5 for the planet simulation. This way the gas surface density (and coincidentally the dust surface density) of both scenarios match each other at the ring location of 28 AU, after 0.16 Myrs of evolution.
From the dust surface density profile we can spot a few differences. First, we notice that the ring formed by photo-evaporation is wider by $\approx$ 5 AU at the half-maximum of the

dust-distribution.
The second difference is that the depletion of the inner region is much more pronounced in the case with photo-evaporation. While the simulation with a planet allows for a fraction of the dust to filter towards the inner regions (Weber et al., 2018), the simulation with photo-evaporation removes all the material in this zone. For the simulation with a planet, we find that the inner regions present a dust-to-gas ratio of $\epsilon \approx 10^{-3}$ inside 20 AU, while the simulation with photo-evaporation is completely depleted.
Unfortunately, the dust size distribution at the ring location does not show any relevant profile differences. Since in both scenarios the growth is limited by fragmentation, the dust sizes follow the same distribution.
In Figure 6.4 we show a set of comparisons between the fiducial photo-evaporative simulation dust profile and simulations different planet masses, orbital radius, and disk masses. The planet simulations that best fit the ring maximum dust concentration (which should be equivalent to fit the peak of the continuum emission in an observation) all show narrower rings than in the photo-evaporative simulation. The planet simulation that best fits the ring width corresponds to a higher disk and planet masses ($q = 5 \times 10^{-3}$, and $M_{\rm disk} = 0.01 M_*$), however in this case we could expect to find larger particles that the ones shown in Figure 6.2, since the maximum Stokes number (determined by the fragmentation barrier) would remain constant, but the particle size would adjust proportionally to the increment in the gas mass (see Equation 1.22, 1.28). In order to distinguish between the planet and photo-evaporation scenarios, some key points that can favor one model or the other could be:

- The ring width, as photo-evaporation produces wider dust distributions.
- The emission from the inner regions, as photo-evaporation depletes both small and large particles, while a planet allows for particles to pass through and grow again in the inner regions.
- The maximum dust size. In order to fit a wider ring with a planet simulation, it would be necessary to increase the dust mass. In turn, this would require a proportional increase of the gas mass, which leads to larger particle sizes.
- The shape of the dust distribution. Dullemond et al. (2018) fitted of the rings from the D-SHARP survey (Andrews et al., 2018), and found that the tail of the distribution is wider than a gaussian profile. We could repeat this experiment for our dust distributions to find characteristic features.

6.5 Caveats

The results on this chapter should be considered as preliminary, as both the planet and photo-evaporation model require additional ingredients and testing.
In particular the photo-evaporation model still needs to implement a second flavor of

photo-evaporation, that considers the increased gas loss rate once the cavity is opened. In this situation, the remaining material between the star and the gap outer edge becomes optically thin, allowing for the stellar radiation to remove additional material that is closer to the midplane (see Picogna et al., 2019). Similarly, we also need check if the code is able to reproduce previous photo-evaporation results when using their corresponding mass loss profiles, such as the ones in Alexander & Armitage (2007). Also, we need to calibrate the dust loss rate in function of the particle size, by fully implementing the results of (Franz et al., 2020) in Equation 6.3.

For the planet simulations we used the model of Armitage & Natarajan (2002), which was initially developed for AGN simulations, in which the f factor (see Equation 6.4) was calibrated to match the width of the gap. To apply this for the modeling of dust rings, we should revisit the calibration, and make sure that the location of the pressure maximum at the outer edge of the gap, which is where the dust grains will accumulate, is in agreement with 2D and 3D simulations.

Similarly, we should check if the pressure profile of the resulting disk, leads to a similar dust distribution to that of a full 3D simulation including a planet potential (such as FARGO-3D, Benítez-Llambay & Masset, 2016). This last point is particularly important, since the study of Weber et al. (2018) showed that 2D grids lead to wider dust rings have a higher dust permeability through the gap (i.e. grains can cross the gap more easily) than in 1D simulations.

A possible solution would be to use a two-dimensional code with dust growth to model the planet dust distribution (Drążkowska et al., 2019), and keep the 1D simulations only for the photo-evaporative models

Checking these points should allow us to point out if it is possible or not to distinguish between a gap carved by a planet, from one carved by photo-evaporation.

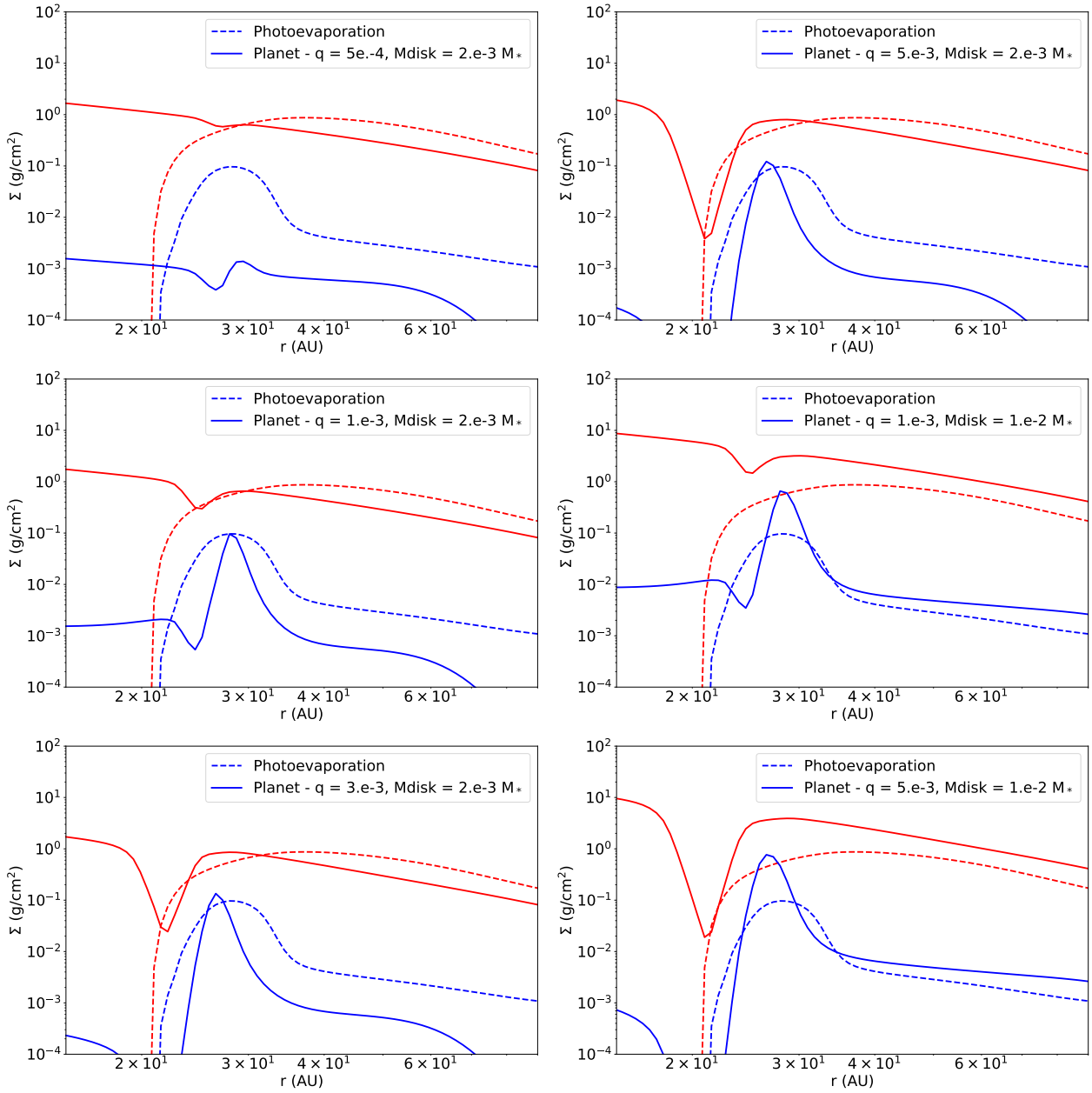

Figure 6.4: Dust and gas density profiles for different planet masses, orbital radius, and disk masses.

Chapter 7

Conclusions and Outlook

In this work we studied the coupled evolution of gas and dust in protoplanetary disks. Starting from the momentum conservation equations for both components, we derived the gas and dust velocities while considering the effect of their mutual drag force, in which the force exerted by the solid grains onto the gas is commonly referred as "dust back-reaction". From our derivation we are able to interpret the dust back-reaction effects in terms of a damping factor, that corrects the gas and dust dynamics for the total mass of the mixture, and a pushing term factor, that originates from the conservation of angular momentum, which results in the dust particles drifting towards the gas pressure maximum, while the gas is pushed away from the pressure maximum.
We implemented our model for the dust back-reaction into different hydro-dynamical codes, that include both the advection of gas and solids, and the growth of multiple species of dust grains, allowing us to solve the evolution of protoplanetary disks in a self-consistent manner (improving previous work that neglected the dust back-reaction).
We find that the maximum grain size, the initial dust-to-gas ratio, and the gas turbulence determine whether or not the dust back-reaction plays an important role in the collective gas and dust dynamics. In general, we find that global dust-to-gas ratios higher than the ISM value by a factor of a few ($\varepsilon_0 \sim 0.03$), low turbulence values ($\alpha \lesssim 10^{-3}$), and mildly coupled dust grains ($\mathrm{St} \gtrsim 10^{-2}$) can lead to scenarios where the back-reaction push is comparable to the standard viscous accretion, slowing down the disk evolution.
Starting from this framework, we studied different types of protoplanetary disks, while incorporating our back-reaction model to their evolution. We find that:

- In the event of a dead zone re-activation, both dust and gas accumulated at the inner regions can flow towards the star in timescales from a few years to a decade, increasing the dust accretion rate by several orders of magnitude. In this scenario, dust back-reaction can slow down the collective flow of gas and dust by a factor of a few, since there is a high concentration of small grains mixed with the gas. This results in an accretion event that can last for a few decades. This enhanced and prolonged dust accretion event could be the origin of the sudden dimmings of the RW Aurigae star, which in the past decade has shown signatures of an enhanced dust content in the line of sight and in the accreted material.

- At the water snowline, dust back-reaction can stop the gas flow, temporarily disconnecting the inner disk from the outer disk in terms of accretion of volatiles mixed with the gas phase (i.e. everything except water vapor). The dust back-reaction then results in a reduced accretion rate onto the star, and an enhancement of the dust-to-gas ratio at the snowline location, where large grains pile-up.

- In dust rings, such as in the outer edge of a gap carved by a either by a planet or by photo-evaporation, the dust back-reaction smooths the gas pressure gradient, which in turns spreads the dust ring over a wider area.

Further applications, and extensions of our current work include:

- Use our photo-evaporative disk models to characterize observations of rings and gaps, and to distinguish the underlying formation mechanism. On the same note, we can look for further signatures and consequences of photo-evaporation in the disk global dust distribution.

- Test if the dust accumulation at the water snowline can cast a shadow on the disk (Ueda et al., 2019), which in turn could affect its temperature profile, and scattered-light signal.

- Combine our photo-evaporation model with the planetesimal formation prescriptions of Drążkowska et al. (2016); Drążkowska & Alibert (2017), and measure the resulting planetesimal distribution. Simultaneously, we can test if planetesimal formation limits the optical depth of the resulting dust ring in this scenario (as shown in Stammler et al., 2019).

- Expand our dead zone re-activation models by considering the accretion heating and measure the expected increment in the gas and dust scale heights.

As illustrated by our results, the dust back-reaction can slow down the collective disk evolution, enhance the dust content, spread out a dust ring, and alter the overall gas and dust dynamics. With this work we now have the tools to determine when the back-reaction becomes a crucial ingredient for our models, when it can be ignored, and what effects can we expect from the coupled gas and dust evolution in protoplanetary disks under a variety of situations.

Appendix A

Derivation of the back-reaction coefficients

In Chapter 2 we derived the gas and dust velocities considering the dust back-reaction onto the gas (Equation 2.3 to 2.6), and expressed them in terms of the back-reaction coefficients (see Section 2.2).
In this section we present the derivation of these expressions, starting from the momentum conservation system of equations, that consider the mutual gas and dust drag forces (considering multiple dust species), the stellar gravity, the pressure support, and the viscous force.

A.1 System of linear equations

We start by expanding the time derivative of the velocity:

$$\frac{d\mathbf{v}}{dt} = \partial_t \mathbf{v} + (\mathbf{v} \cdot \nabla)\mathbf{v}. \tag{A.1}$$

Here the velocity $\mathbf{v}$ can be used to represent either gas and dust, since the first part of the derivation is the same for both. For simplicity, from here onward we will use the notation ∂_i to refer to the partial derivative in the variable i, and v_i to refer to the spatial coordinate i of the velocity.
Expanding the material derivative in cylindrical coordinates we have:

$$(\mathbf{v} \cdot \nabla)\mathbf{v} = \left(\begin{bmatrix} v_r \\ v_\theta \\ v_z \end{bmatrix} \cdot \begin{bmatrix} \partial_r \\ r^{-1}\partial_\theta \\ \partial_z \end{bmatrix} \right) \begin{bmatrix} v_r \\ v_\theta \\ v_z \end{bmatrix} + \begin{bmatrix} -v_\theta^2 r^{-1} \\ v_r v_\theta r^{-1} \\ 0 \end{bmatrix}. \tag{A.2}$$

Following (Nakagawa et al., 1986) we write the velocities as:

$$\mathbf{v} = v_r \hat{\mathbf{r}} + (v_K + \Delta v_\theta)\hat{\theta} + v_z \hat{\mathbf{z}}, \tag{A.3}$$

where $v_K = r\Omega_K$ is the keplerian orbital velocity, and we also make the following approximations:

- The gas and dust reach the terminal velocity, so $\partial_t v = 0$.
- There is azimuthal symmetry, so $\partial_\theta v_i = 0$.
- The keplerian velocity is the dominant component, therefore $v_K \gg v_r, \Delta v_\theta, v_z$. Therefore any second order term that involve v_r, Δv_θ, and v_z, or a combination of them is negligible.

Applying these approximations we obtain:

$$\frac{d\mathbf{v}}{dt} = -\left(r\Omega_K^2 + 2\Omega_K \Delta v_\theta\right)\,\hat{\mathbf{r}} + \frac{1}{2}\Omega_K v_r\,\hat{\theta} + 0\,\hat{\mathbf{z}}. \tag{A.4}$$

Now we proceed to expand the momentum equations (Equation 2.1 and 2.2) into the radial and azimuthal components. For the gas we have the following equations:

$$-r\Omega_K^2 - 2\Omega_K \Delta v_{\mathrm{g},\theta} = \sum_m \frac{(v^m_{\mathrm{d},r} - v_{\mathrm{g},r})}{t_{\mathrm{stop}}}\epsilon_m - r\Omega_K^2 + f_P, \tag{A.5}$$

$$\frac{1}{2}\Omega_K v_{\mathrm{g},r} = \sum_m \frac{(v^m_{\mathrm{d},\theta} - v_{\mathrm{g},\theta})}{t_{\mathrm{stop}}}\epsilon_m + f_\nu. \tag{A.6}$$

For each dust species we have the following pair of equations corresponding to the azimuthal and radial components:

$$-r\Omega_K^2 - 2\Omega_K \Delta v^m_{\mathrm{d},\theta} = -\frac{(v^m_{\mathrm{d},r} - v_{\mathrm{g},r})}{t_{\mathrm{stop}}} - r\Omega_K^2, \tag{A.7}$$

$$\frac{1}{2}\Omega_K v^m_{\mathrm{d},r} = -\frac{(v^m_{\mathrm{d},\theta} - v_{\mathrm{g},\theta})}{t_{\mathrm{stop}}}. \tag{A.8}$$

Notice that for Equation A.5 to A.8 we expanded our notation for the dust velocity, where $v^m_{\mathrm{d},i}$ refers to the velocity component in the "i" coordinate, for the dust species "m". Therefore, we have a set of $2N+2$ linear equations, where N is the number of dust species. We can rearrange these equations to our convenience by canceling the $-r\Omega_K^2$ term that appears in Equation A.5 and A.7, and dividing all the equations Ω_K, so that we can form the Stokes number $St = t_{\mathrm{stop}}\Omega_K$, and notice that $v^m_{\mathrm{d},\theta} - v_{\mathrm{g},\theta} = \Delta v^m_{\mathrm{d},\theta} - \Delta v_{\mathrm{g},\theta}$. Therefore, our equations become:

$$2\Delta v_{\mathrm{g},\theta} + \sum_m \frac{(v^m_{\mathrm{d},r} - v_{\mathrm{g},r})}{\mathrm{St}}\epsilon_m = -2v_P, \tag{A.9}$$

$$\frac{1}{2}v_{\mathrm{g},r} - \sum_m \frac{(\Delta v^m_{\mathrm{d},\theta} - \Delta v_{\mathrm{g},\theta})}{\mathrm{St}}\epsilon_m = \frac{1}{2}v_\nu, \tag{A.10}$$

$$2\Delta v^m_{\mathrm{d},\theta} - \frac{(v^m_{\mathrm{d},r} - v_{\mathrm{g},r})}{\mathrm{St}} = 0, \tag{A.11}$$

$$\frac{1}{2} v^m_{\mathrm{d},r} + \frac{(\Delta v^m_{\mathrm{d},\theta} - \Delta v_{\mathrm{g},\theta})}{\mathrm{St}} = 0, \tag{A.12}$$

where we replaced the terms $f_P/\Omega_K = 2v_P$ and $f_\nu/\Omega_K = v_\nu/2$, with the pressure and viscous velocity equivalents.
With this system we can now proceed to solve for the gas and dust velocity components.

A.2 Solving for the dust velocities

We begin by finding a solution for the dust velocities in terms of the gas velocities. We can write the reduced system of Equation A.11 and A.12 in matrix form as:

$$\begin{bmatrix} -\mathrm{St}^{-1} & 2 \\ 1/2 & \mathrm{St}^{-1} \end{bmatrix} \begin{bmatrix} v^m_{\mathrm{d},r} \\ \Delta v^m_{\mathrm{d},\theta} \end{bmatrix} = \begin{bmatrix} -\mathrm{St}^{-1} v_{\mathrm{g},r} \\ \mathrm{St}^{-1} \Delta v_{\mathrm{g},\theta} \end{bmatrix}. \tag{A.13}$$

Solving this equation system we recover the dust velocities from Equation 2.5 and 2.6:

$$v_{\mathrm{d},r} = \frac{1}{1+\mathrm{St}^2} v_{\mathrm{g},r} + \frac{2\mathrm{St}}{1+\mathrm{St}^2} \Delta v_{\mathrm{g},\theta}, \tag{A.14}$$

$$\Delta v_{\mathrm{d},\theta} = \frac{1}{1+\mathrm{St}^2} \Delta v_{\mathrm{g},\theta} - \frac{\mathrm{St}}{2(1+\mathrm{St}^2)} v_{\mathrm{g},r}. \tag{A.15}$$

A.3 Solving for the gas velocities

To find the gas velocities, we start by replacing the dust velocities found in the previous section (Equation A.14 and A.15) into the equations Equation A.9 and A.10, obtaining:

$$2\Delta v_{\mathrm{g},\theta} - v_{\mathrm{g},r} \sum_m \frac{\mathrm{St}}{1+\mathrm{St}^2} \epsilon_m + 2 v_{\mathrm{g},\theta} \sum_m \frac{1}{1+\mathrm{St}^2} \epsilon_m = -2 v_P, \tag{A.16}$$

$$\frac{1}{2} v_{\mathrm{g},r} + v_{\mathrm{g},\theta} \sum_m \frac{\mathrm{St}}{1+\mathrm{St}^2} \epsilon_m + \frac{1}{2} v_{\mathrm{g},r} \sum_m \frac{1}{1+\mathrm{St}^2} \epsilon_m = \frac{1}{2} v_\nu. \tag{A.17}$$

From these equations we notice some common factors, defined in Okuzumi et al. (2012) (also in Tanaka et al., 2005; Dipierro et al., 2018) as:

$$X = \sum_m \frac{1}{1+\mathrm{St}^2} \epsilon_m, \tag{A.18}$$

$$Y = \sum_m \frac{\mathrm{St}}{1+\mathrm{St}^2} \epsilon_m. \tag{A.19}$$

Writing the system of equations in matrix form we have:

$$\begin{bmatrix} -Y & 2(X+1) \\ (X+1)/2 & Y \end{bmatrix} \begin{bmatrix} v_{\mathrm{g},r} \\ \Delta v_{\mathrm{g},\theta} \end{bmatrix} = \begin{bmatrix} -2v_P \\ v_\nu/2 \end{bmatrix}. \tag{A.20}$$

Solving the system we find that:

$$v_{\mathrm{g},r} = \frac{1}{(X+1)^2 + Y^2} \left((X+1)\, v_\nu + 2Y v_P \right), \tag{A.21}$$

$$\Delta v_{\mathrm{g},\theta} = \frac{1}{(X+1)^2 + Y^2} \left(\frac{1}{2} Y v_\nu - (X+1)\, v_P \right). \tag{A.22}$$

Here it is convenient to defined the back-reaction coefficients as

$$A = \frac{X+1}{Y^2 + (X+1)^2}, \tag{A.23}$$

$$B = \frac{Y}{Y^2 + (X+1)^2}, \tag{A.24}$$

which results in the equations described in Chapter 2 for the gas velocities:

$$v_{\mathrm{g},r} = A v_\nu + 2B v_P, \tag{A.25}$$

$$\Delta v_{\mathrm{g},\theta} = \frac{1}{2} B v_\nu - A v_P. \tag{A.26}$$

Appendix B

Semi-Analytical test for back-reaction simulations

The contents of this chapter where published in the Astronomy & Astrophysics Journal.
Credit: Appendix of Gas accretion damped by dust back-reaction at the snow line, Gárate et al., A&A, 635, A149, 2020.

B.1 An equivalent α value to describe the back-reaction.

In this section we intend to rewrite the radial velocity of the gas (Equation 2.3) in a similar way to the standard viscous velocity of Lynden-Bell & Pringle (1974).
We use the modified forms of the viscous and pressure velocity given by Equation 2.24 and 2.25 which were defined as:

$$v_\nu = -3\alpha_\nu \frac{c_s^2}{v_K}\gamma_\nu, \tag{B.1}$$

$$v_P = -\frac{1}{2}\frac{c_s^2}{v_K}\gamma_P. \tag{B.2}$$

Using these expressions, we can rewrite the gas radial velocity (Equation A.25) as the viscous velocity in Equation 2.24, with the following α_ν-equivalent parameter:

$$\alpha_{\rm eq} = \alpha_\nu A + \frac{\gamma_P}{3\gamma_\nu}B, \tag{B.3}$$

$$v_{\rm g} = -3\alpha_{\rm eq}\frac{c_s^2}{v_K}\gamma_\nu. \tag{B.4}$$

This means that we can understand the evolution of a gas disk considering dust back-reaction, as a viscous evolution with a modified α_ν value (we discuss the limits of this interpretation in Appendix B.1.2). From this point we can make further simplifications

to develop a semi-analytical test for a back-reaction simulation using a standard viscous evolution model.
Our first simplification is that the surface density and temperature follow a power law profile with $\Sigma \propto r^{-p}$ and $T \propto r^{-q}$, which sets the factor $\gamma_P/(3\gamma_\nu)$ involving the density and temperature gradients to:

$$\frac{\gamma_P}{3\gamma_\nu} = -\frac{2p+q+3}{6(2-p-q)}. \tag{B.5}$$

In particular, if the disk is in steady state with $p = 1$ and $q = 1/2$, then $\gamma_P/(3\gamma_\nu) = -11/6$, and the accretion rate is:

$$\dot{M} = 3\pi\alpha_{\rm eq}\frac{c_s^2}{\Omega_K}\Sigma_g. \tag{B.6}$$

Now, assuming that the distribution of dust particles has sizes between $0 < \mathrm{St} < \mathrm{St}_{\rm max}$, and that $\mathrm{St}^2 \ll \epsilon$, we can constrain the value of $\alpha_{\rm eq}$ using the single particle approximation for the coefficients $A_{\rm single}$ and $B_{\rm single}$ (Equation 2.13 and 2.14). Then the minimum value that $\alpha_{\rm eq}$ can take, given by the largest size particles, is:

$$\alpha_{\rm eq,\ min} \approx \frac{\alpha_\nu}{\epsilon+1} - \frac{11}{6}\frac{\epsilon\,\mathrm{St}_{\rm max}}{(\epsilon+1)^2}, \tag{B.7}$$

and the maximum value that $\alpha_{\rm eq}$ can take, given by the smallest particles with $\mathrm{St} \approx 0$, is:

$$\alpha_{\rm eq,\ max} \approx \frac{\alpha_\nu}{\epsilon+1}. \tag{B.8}$$

B.1.1 Setting up a test simulation

From the equivalent viscosity equation (Equation B.3) we can set a test to ensure that the back-reaction effects in a numerical simulation are acting according to the theoretical model.
We prepare a test for the code `twopoppy` that was used throughout the paper (Birnstiel et al., 2012), and also for the code `DustPy` (Stammler and Birnstiel, in prep.), that solves the Smoluchowski equation for particle growth by sticking and fragmentation of multiple dust species as in Birnstiel et al. (2010), along with the advection-diffusion equations (Equation 1.1 and 1.16).
The test disk has the following set-up:

- The surface density and temperature have steady state power law profiles with $p = 1$ and $q = 1/2$.
- To enhance the back-reaction damping and obtain obvious deviations from the regular dust-free evolution we set an unrealistic disk with $\epsilon = 0.5$.
- The fragmentation velocity follows $v_{\rm frag} \propto r^{-q}$ so that the maximum particle size (Equation 1.28) has a constant value of $\mathrm{St}_{\rm max} = 5 \times 10^{-3}$.

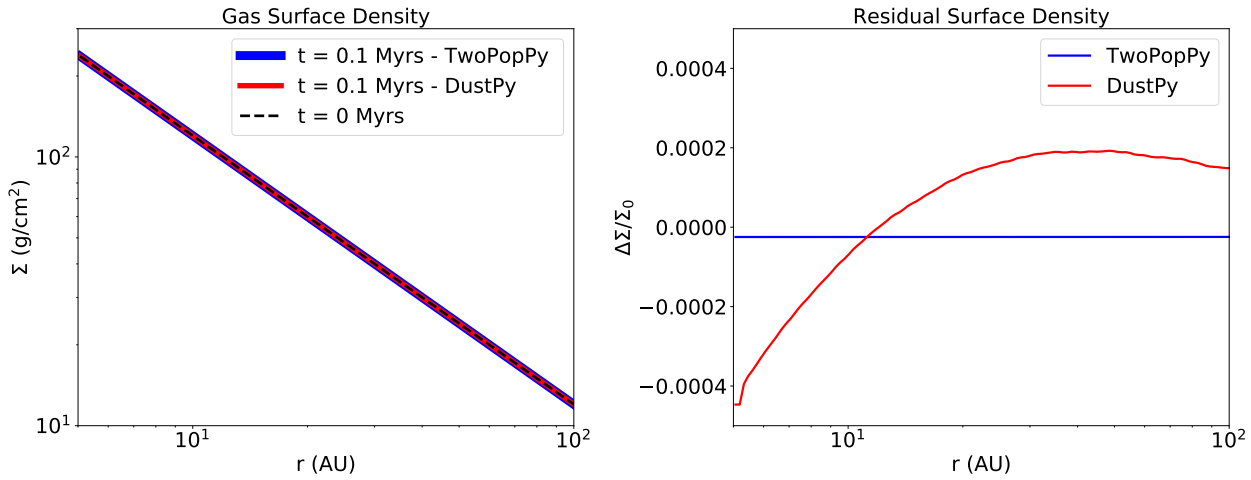

Figure B.1: *Left:* Initial and final surface density of the test simulations. If the disk evolution with back-reaction is equivalent to a regular viscous evolution, the steady state should be maintained through the simulation. *Right:* Surface density residuals relative to the initial state. After 0.1 Myrs of evolution, the simulations deviate by less a value of 0.05% from the steady state profile.

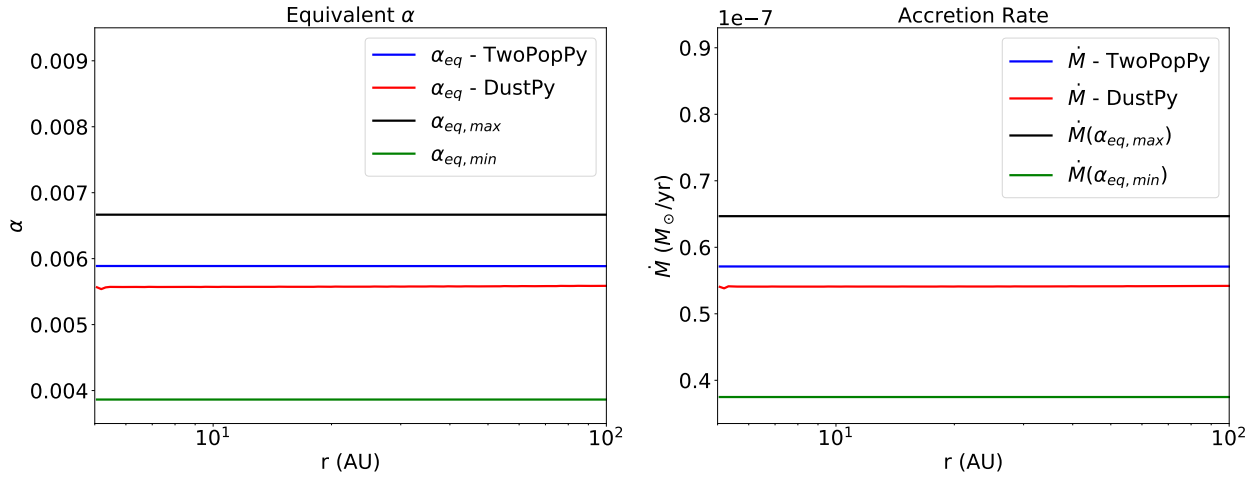

Figure B.2: *Left:* Equivalent α_ν value (Equation B.3) obtained from the simulations (red - DustPy, blue - TwoPopPy), and the analytical limits given by $\alpha_{\text{eq, min}}$ (green) and $\alpha_{\text{eq, max}}$ (black). The value obtained from the simulations is in between the two limits, in agreement with the analytical model. *Right:* Accretion rate measured from the simulations, and the steady state accretion rate for the different α_{eq} limits.

- The turbulent viscosity is set to $\alpha_\nu = 10^{-2}$, so that the back-reaction is not strong enough to reverse the accretion of gas.
- The dust diffusion is turned off, so that the dust is only advected through the velocity $v_{\mathrm{d,r}}$ (Equation 2.5).
- The disk is initialized with a fully grown particle distribution (so that the back-reaction effects are uniform through the disk).
- The back-reaction coefficients (in this test case) are implemented assuming that the dust-to-gas ratio is vertically uniform.

If the simulations are working properly, then the disk will remain in steady state, and the accretion rate will be constant in radius with a value given by the damped equivalent viscosity α_{eq} (Equation B.6). Since in this test case all the particles are small ($\mathrm{St} < \alpha_\nu$) and the size distribution is constant with radius, the dust-to-gas ratio and the back-reaction effects should also remain approximately uniform in time.
As shown in Figure B.1, after 0.1 Myr the disk surface density between $5 - 100$ au remains close to the steady state profile, with a deviation of less than 0.1% relative to its initial value.
Figure B.2 shows that the mass accretion rate of the gas in the simulations is $\dot{M} \approx 5.6 \times 10^{-8}\,\mathrm{M}_\odot/\mathrm{yr}$ and constant through the disk, in agreement with a steady state solution. More importantly, the value of the accretion is constrained between the minimum and maximum values given by $\alpha_{\mathrm{eq,\,min}}$ and $\alpha_{\mathrm{eq,\,max}}$ and Equation B.6.
In terms of the viscous accretion, the back-reaction effect in our setup is equivalent to reduce the turbulent viscosity α_ν to a value of $\alpha_{\mathrm{eq}} \approx 0.57\,\alpha_\nu$.
Both `twopoppy` and `DustPy` deliver similar results, with a relative difference of roughly 5% in the α_{eq} and $\dot{M}$ values. From here we can conclude that the back-reaction effects observed in the two population model are expected to be in agreement with those from a proper particle distribution.

B.1.2 Where the viscous approximation breaks

While we can always write the gas velocity in the form of Equation B.4 using the α_{eq} parameter (Equation B.3), the global disk evolution will still differ from a regular viscous evolution (unless $\alpha_{\mathrm{eq}} \propto \alpha_\nu$), as the value of γ_ν does not depend on the slope of α_{eq}.
In particular, the back-reaction effects cannot be treated as a viscous process if $\mathrm{St}\,\epsilon/(\epsilon{+}1) \gtrsim \alpha_\nu$ (Dipierro et al., 2018). In this case the back-reaction push becomes more important than the inward viscous transport, and results in negative equivalent α_{eq} values, meaning that mass will be transported against the pressure gradient.
Also, in the outer regions of the disk where the surface density profile becomes steeper (as in the self-similar solution Lynden-Bell & Pringle, 1974), the viscous evolution spreads the gas outwards ($\gamma_\nu < 0$, $v_\nu > 0$). In these regions the dust back-reaction pushes the gas in the same direction as the viscous spreading ($2Bv_P > 0$), and therefore contributes to evolve the outer disk faster than the inner disk.

Appendix C

Gap opening criteria

The contents of this chapter where published in the Astronomy & Astrophysics Journal.
Credit: Appendix of Gas accretion damped by dust back-reaction at the snow line, Gárate et al., A&A, 635, A149, 2020.

In this section we will derive a criterion to determine if the dust back-reaction can clear a gap in the gas, based on the transport of angular momentum and the global disk properties. The condition to clear a gap, is that the clearing timescale $t_{\rm clear}$ must be shorter than the viscous timescale t_ν:

$$t_{\rm clear} < t_\nu. \tag{C.1}$$

Now we proceed to derive $t_{\rm clear}$ from the exchange of angular momentum between the dust and gas.
The angular momentum of a parcel of material with mass m, at a radius r, and with orbital velocity $v_K = \sqrt{GM/r}$ is:

$$J = v_K\, r\, m. \tag{C.2}$$

The angular momentum required to transport a ring of material from a radius r to r_1 is:

$$\mathrm{d}J = \left(\sqrt{\frac{r_1}{r_0}} - \sqrt{\frac{r}{r_0}}\right) v_0 r_0\, \mathrm{d}m, \tag{C.3}$$

where v_0 is the keplerian velocity at radius r_0, and the mass of a gas ring is $\mathrm{d}m = 2\pi r \Sigma_{\rm g} \mathrm{d}r$. Assuming that the gas surface density is $\Sigma_{\rm g} = \Sigma_0 (r_0/r)$, then the total angular momentum required to clear a gap between r_0 and r_1 is given by:

$$J_{\rm clear} = \int \mathrm{d}J = 2\pi\, v_0 r_0^2 \Sigma_0 \int_{r_0}^{r_1} \sqrt{\frac{r_1}{r_0}} - \sqrt{\frac{r}{r_0}}\, \mathrm{d}r. \tag{C.4}$$

Solving the integral we obtain:

$$J_{\rm clear} = 2\pi\, v_0 r_0^3 \Sigma_0 \cdot \left(\frac{1}{3}\left(\frac{r_1}{r_0}\right)^{3/2} - \left(\frac{r_1}{r_0}\right)^{1/2} + \frac{2}{3}\right). \tag{C.5}$$

From Equation C.3 we can also infer that the dust drifting from a radius r_1 to r_0 loses angular momentum (and delivers it to the gas) at a rate of:

$$\dot{J}_{\rm drift} = v_0 r_0 \dot{M}_{\rm d}(r_1) \left(\left(\frac{r_1}{r_0} \right)^{1/2} - 1 \right), \tag{C.6}$$

where the accretion rate of dust at r_1 is:

$$\dot{M}_{\rm d}(r_1) = 2\pi r_1 \Sigma_{\rm d}(r_1) v_{\rm d,r}(r_1), \tag{C.7}$$

where we will assume an uniform dust-to-gas ratio, using $\Sigma_{\rm d} = \varepsilon \, \Sigma_{\rm g}$.
Then, considering only the drifting component of the dust velocity (see Equation 2.5) we obtain that:

$$v_{\rm d,r}(r_1) = 2{\rm St}\, v_P(r_1) = -{\rm St}\, \gamma_P \left(\frac{h}{r} \right)^2 v_0 \left(\frac{r_1}{r_0} \right)^{-1/2}, \tag{C.8}$$

where have taken the limit of small particles (${\rm St} \ll 1$), and expanded the expression for the pressure velocity given in Equation 2.25 using $h/r = c_s/v_K$.
Now we can write the gap opening timescale as:

$$t_{\rm clear} = \frac{J_{\rm clear}}{|\dot{J}_{\rm drift}|} = C \left(\frac{r_1}{r_0} \right) \left(\frac{h}{r} \right)^{-2} \varepsilon^{-1} {\rm St}^{-1} v_0^{-1} r_0, \tag{C.9}$$

with $C(x)$ a function of the ratio $x = r_1/r_0$:

$$C(x) = \frac{x^2 - 3x + 2\sqrt{x}}{3\gamma_P(\sqrt{x} - 1)}. \tag{C.10}$$

We apply this formula to our simulations, using a scale height of $h/r = 0.05$, $\gamma_P = 2.75$, and study the time required to clear a gap between $r_0 = 2.5\,{\rm au}$ (which is approximately the location of the snowline) and $r_1 = 10\,{\rm au}$, and find:

$$t_{\rm clear} \approx \left(\frac{\varepsilon}{0.01} \right)^{-1} \left(\frac{\rm St}{0.03} \right)^{-1} 0.84\,{\rm Myr}. \tag{C.11}$$

Now, we only need to compare it with the viscous timescale, which can be understood in this case as the time necessary to close the gap:

$$t_\nu = r_0^2/\nu = \frac{r_0}{v_0 \alpha} \left(\frac{h}{r} \right)^{-2}, \tag{C.12}$$

which at the snowline location of $r_0 = 2.5\,{\rm au}$ give us a time of:

$$t_\nu = \left(\frac{\alpha}{10^{-3}} \right)^{-1} 0.25\,{\rm Myr}. \tag{C.13}$$

To conclude we can derive from Equation C.1, (C.9) and (C.12) a condition on α, ε and St to see if the dust back-reaction can clear a gap:

$$\frac{\varepsilon \mathrm{St}}{\alpha} \gtrsim C(r_1/r_0 = 4) \approx 1, \tag{C.14}$$

where we have taken $r_0 = 2.5\,\mathrm{au}$ and $r_1 = 10\,\mathrm{au}$. Notice that this condition is similar to $2Bv_P \gtrsim Av_\nu$ (Equation 2.3), which indicates if gas motion is locally dominated by the dust back-reaction.

The advantage of this criteria is that it depends on the ratio r_1/r_0, and the disk global dust-to-gas ratio, instead of the local one. In Gárate et al. (2020) we showed that this criteria effectively describes when a gap is opened around the snowline using the disk global properties, for different values of ε and α.

Bibliography

Akeson, R. L., Boden, A. F., Monnier, J. D., et al. 2005, ApJ, 635, 1173

Alexander, R. D. & Armitage, P. J. 2007, MNRAS, 375, 500

Alexander, R. D., Clarke, C. J., & Pringle, J. E. 2006a, MNRAS, 369, 216

Alexander, R. D., Clarke, C. J., & Pringle, J. E. 2006b, MNRAS, 369, 229

ALMA Partnership, Brogan, C. L., Pérez, L. M., et al. 2015, ApJ, 808, L3

Andrews, S. M. 2020, arXiv e-prints, arXiv:2001.05007

Andrews, S. M., Huang, J., Pérez, L. M., et al. 2018, ApJ, 869, L41

Andrews, S. M. & Williams, J. P. 2005, ApJ, 631, 1134

Andrews, S. M., Wilner, D. J., Zhu, Z., et al. 2016, ApJ, 820, L40

Ansdell, M., Williams, J. P., van der Marel, N., et al. 2016, ApJ, 828, 46

Antipin, S., Belinski, A., Cherepashchuk, A., et al. 2015, Information Bulletin on Variable Stars, 6126, 1

Armitage, P. J. & Natarajan, P. 2002, ApJ, 567, L9

Audard, M., Ábrahám, P., Dunham, M. M., et al. 2014, Protostars and Planets VI, 387

Bae, J. & Zhu, Z. 2018, ApJ, 859, 118

Balbus, S. A. & Hawley, J. F. 1991, ApJ, 376, 214

Benítez-Llambay, P. & Masset, F. S. 2016, ApJS, 223, 11

Berdnikov, L. N., Burlak, M. A., Vozyakova, O. V., et al. 2017, Astrophysical Bulletin, 72, 277

Birnstiel, T., Dullemond, C. P., & Brauer, F. 2009, A&A, 503, L5

Birnstiel, T., Dullemond, C. P., & Brauer, F. 2010, A&A, 513, A79

Birnstiel, T., Klahr, H., & Ercolano, B. 2012, A&A, 539, A148

Blandford, R. D. & Payne, D. G. 1982, MNRAS, 199, 883

Blum, J. & Wurm, G. 2000, Icarus, 143, 138

Blum, J. & Wurm, G. 2008, ARA&A, 46, 21

Bohlin, R. C., Savage, B. D., & Drake, J. F. 1978, ApJ, 224, 132

Booth, R. A. & Clarke, C. J. 2018, MNRAS, 473, 757

Boss, A. P. 1997, Science, 276, 1836

Bozhinova, I., Scholz, A., Costigan, G., et al. 2016, MNRAS, 463, 4459

Brauer, F., Dullemond, C. P., & Henning, T. 2008a, A&A, 480, 859

Brauer, F., Henning, T., & Dullemond, C. P. 2008b, A&A, 487, L1

Bryden, G., Chen, X., Lin, D. N. C., Nelson, R. P., & Papaloizou, J. C. B. 1999, ApJ, 514, 344

Cabrit, S., Pety, J., Pesenti, N., & Dougados, C. 2006, A&A, 452, 897

Carr, J. S. & Najita, J. R. 2008, Science, 319, 1504

Carrera, D., Gorti, U., Johansen, A., & Davies, M. B. 2017, ApJ, 839, 16

Chatterjee, S. & Tan, J. C. 2014, ApJ, 780, 53

Ciesla, F. J. & Cuzzi, J. N. 2006, Icarus, 181, 178

Cuello, N., Dipierro, G., Mentiplay, D., et al. 2019a, MNRAS, 483, 4114

Cuello, N., Montesinos, M., Stammler, S. M., Louvet, F., & Cuadra, J. 2019b, A&A, 622, A43

Dipierro, G. & Laibe, G. 2017, MNRAS, 469, 1932

Dipierro, G., Laibe, G., Alexander, R., & Hutchison, M. 2018, MNRAS, 479, 4187

Drążkowska, J., Li, S., Birnstiel, T., Stammler, S. M., & Li, H. 2019, ApJ, 885, 91

Drążkowska, J. & Alibert, Y. 2017, A&A, 608, A92

Drążkowska, J., Alibert, Y., & Moore, B. 2016, A&A, 594, A105

Drążkowska, J. & Dullemond, C. P. 2018, A&A, 614, A62

Dubrulle, B., Morfill, G., & Sterzik, M. 1995, Icarus, 114, 237

Dullemond, C. P., Birnstiel, T., Huang, J., et al. 2018, ApJ, 869, L46

Eisner, J. A., Hillenbrand, L. A., White, R. J., et al. 2007, ApJ, 669, 1072

Ercolano, B., Barlow, M. J., & Storey, P. J. 2005, MNRAS, 362, 1038

Ercolano, B., Barlow, M. J., Storey, P. J., & Liu, X. W. 2003, MNRAS, 340, 1136

Ercolano, B. & Pascucci, I. 2017, Royal Society Open Science, 4, 170114

Ercolano, B., Rosotti, G. P., Picogna, G., & Testi, L. 2017, MNRAS, 464, L95

Ercolano, B., Young, P. R., Drake, J. J., & Raymond, J. C. 2008, ApJS, 175, 534

Espaillat, C., Muzerolle, J., Najita, J., et al. 2014, in Protostars and Planets VI, ed. H. Beuther, R. S. Klessen, C. P. Dullemond, & T. Henning, 497

Estrada, P. R., Cuzzi, J. N., & Morgan, D. A. 2016, ApJ, 818, 200

Facchini, S., Manara, C. F., Schneider, P. C., et al. 2016, A&A, 596, A38

Fontecilla, C., Chen, X., & Cuadra, J. 2017, MNRAS, 468, L50

Franz, R., Picogna, G., Ercolano, B., & Birnstiel, T. 2020, A&A, 635, A53

Fromang, S. & Nelson, R. P. 2009, A&A, 496, 597

Gammie, C. F. 1996, ApJ, 457, 355

Gárate, M., Birnstiel, T., Drążkowska, J., & Stammler, S. M. 2020, A&A, 635, A149

Gárate, M., Birnstiel, T., Stammler, S. M., & Günther, H. M. 2019, ApJ, 871, 53

Garaud, P. 2007, ApJ, 671, 2091

Ghez, A. M., White, R. J., & Simon, M. 1997, ApJ, 490, 353

Goldreich, P. & Tremaine, S. 1979, ApJ, 233, 857

Gonzalez, J.-F., Laibe, G., & Maddison, S. T. 2017, MNRAS, 467, 1984

Gonzalez, J. F., Laibe, G., Maddison, S. T., Pinte, C., & Ménard, F. 2015, MNRAS, 454, L36

Gundlach, B. & Blum, J. 2015, ApJ, 798, 34

Gundlach, B., Kilias, S., Beitz, E., & Blum, J. 2011, Icarus, 214, 717

Gundlach, B., Schmidt, K. P., Kreuzig, C., et al. 2018, MNRAS, 479, 1273

Günther, H. M., Birnstiel, T., Huenemoerder, D. P., et al. 2018, AJ, 156, 56

Günther, H. M., Liefke, C., Schmitt, J. H. M. M., Robrade, J., & Ness, J.-U. 2006, A&A, 459, L29

Güttler, C., Blum, J., Zsom, A., Ormel, C. W., & Dullemond, C. P. 2010, A&A, 513, A56

Haisch, Karl E., J., Lada, E. A., & Lada, C. J. 2001, ApJ, 553, L153

Hartigan, P., Edwards, S., & Ghandour, L. 1995, ApJ, 452, 736

Homma, K. A., Okuzumi, S., Nakamoto, T., & Ueda, Y. 2019, ApJ, 877, 128

Huang, J., Andrews, S. M., Cleeves, L. I., et al. 2018, ApJ, 852, 122

Hyodo, R., Ida, S., & Charnoz, S. 2019, A&A, 629, A90

Ingleby, L., Calvet, N., Herczeg, G., et al. 2013, ApJ, 767, 112

Johansen, A., Henning, T., & Klahr, H. 2006, ApJ, 643, 1219

Johansen, A., Oishi, J. S., Mac Low, M.-M., et al. 2007, Nature, 448, 1022

Johansen, A., Youdin, A., & Mac Low, M.-M. 2009, ApJ, 704, L75

Kanagawa, K. D., Muto, T., Okuzumi, S., et al. 2018, ApJ, 868, 48

Kanagawa, K. D., Ueda, T., Muto, T., & Okuzumi, S. 2017, ApJ, 844, 142

Kataoka, A., Tanaka, H., Okuzumi, S., & Wada, K. 2013, A&A, 557, L4

Koepferl, C. M., Ercolano, B., Dale, J., et al. 2013, MNRAS, 428, 3327

Kretke, K. A., Lin, D. N. C., Garaud, P., & Turner, N. J. 2009, ApJ, 690, 407

Lambrechts, M. & Johansen, A. 2012, A&A, 544, A32

Lambrechts, M., Johansen, A., & Morbidelli, A. 2014, A&A, 572, A35

Lamzin, S., Cheryasov, D., Chuntonov, G., et al. 2017, in Stars: From Collapse to Collapse, Vol. 510, 356

Lichtenberg, T. & Schleicher, D. R. G. 2015, A&A, 579, A32

Lichtenegger, H. I. M. & Komle, N. I. 1991, Icarus, 90, 319

Lin, D. N. C. & Papaloizou, J. 1979, MNRAS, 186, 799

Lin, D. N. C. & Papaloizou, J. C. B. 1993, in Protostars and Planets III, ed. E. H. Levy & J. I. Lunine, 749

Lin, D. N. C. & Pringle, J. E. 1987, MNRAS, 225, 607

Lodders, K. 2003, ApJ, 591, 1220

Lüst, R. 1952, Zeitschrift Naturforschung Teil A, 7, 87

Lynden-Bell, D. & Pringle, J. E. 1974, MNRAS, 168, 603

Manara, C. F., Testi, L., Herczeg, G. J., et al. 2017, A&A, 604, A127

Martin, R. G. & Lubow, S. H. 2011, ApJ, 740, L6

Mathis, J. S., Rumpl, W., & Nordsieck, K. H. 1977, ApJ, 217, 425

Mignone, A., Bodo, G., Massaglia, S., et al. 2007, ApJS, 170, 228

Musiolik, G. & Wurm, G. 2019, ApJ, 873, 58

Najita, J. R. & Bergin, E. A. 2018, ApJ, 864, 168

Nakagawa, Y., Sekiya, M., & Hayashi, C. 1986, Icarus, 67, 375

Nayakshin, S. 2017, PASA, 34, 002

Nealon, R., Cuello, N., & Alexander, R. 2020, MNRAS, 491, 4108

Nelson, R. P., Gressel, O., & Umurhan, O. M. 2013, MNRAS, 435, 2610

Öberg, K. I., Murray-Clay, R., & Bergin, E. A. 2011, ApJ, 743, L16

Okuzumi, S., Tanaka, H., Kobayashi, H., & Wada, K. 2012, ApJ, 752, 106

Onishi, I. K. & Sekiya, M. 2017, Earth, Planets, and Space, 69, 50

Ormel, C. W. & Cuzzi, J. N. 2007, A&A, 466, 413

Osterloh, M. & Beckwith, S. V. W. 1995, ApJ, 439, 288

Owen, J. E. & Kollmeier, J. A. 2019, MNRAS, 487, 3702

Paardekooper, S.-J. & Mellema, G. 2004, A&A, 425, L9

Petrov, P. P., Gahm, G. F., Djupvik, A. A., et al. 2015, A&A, 577, A73

Picogna, G., Ercolano, B., Owen, J. E., & Weber, M. L. 2019, MNRAS, 487, 691

Pinilla, P., Benisty, M., & Birnstiel, T. 2012, A&A, 545, A81

Pinilla, P., Flock, M., Ovelar, M. d. J., & Birnstiel, T. 2016, A&A, 596, A81

Pinilla, P., Pohl, A., Stammler, S. M., & Birnstiel, T. 2017, ApJ, 845, 68

Pollack, J. B., Hubickyj, O., Bodenheimer, P., et al. 1996, Icarus, 124, 62

Poppe, T., Blum, J., & Henning, T. 2000, ApJ, 533, 454

Pringle, J. E. 1981, ARA&A, 19, 137

Rice, W. K. M., Armitage, P. J., Wood, K., & Lodato, G. 2006, MNRAS, 373, 1619

Rieke, G. H., Wright, G. S., Böker, T., et al. 2015, PASP, 127, 584

Rodriguez, J. E., Loomis, R., Cabrit, S., et al. 2018, ApJ, 859, 150

Rodriguez, J. E., Pepper, J., Stassun, K. G., et al. 2013, AJ, 146, 112

Rodriguez, J. E., Reed, P. A., Siverd, R. J., et al. 2016, AJ, 151, 29

Rosotti, G. P., Clarke, C. J., Manara, C. F., & Facchini, S. 2017, MNRAS, 468, 1631

Salyk, C., Pontoppidan, K. M., Blake, G. A., et al. 2008, ApJ, 676, L49

Schneider, P. C., Günther, H. M., Robrade, J., et al. 2015, A&A, 584, L9

Schneider, P. C., Manara, C. F., Facchini, S., et al. 2018, A&A, 614, A108

Schoonenberg, D. & Ormel, C. W. 2017, A&A, 602, A21

Shakura, N. I. & Sunyaev, R. A. 1973, A&A, 24, 337

Shenavrin, V. I., Petrov, P. P., & Grankin, K. N. 2015, Information Bulletin on Variable Stars, 6143

Skrutskie, M. F., Dutkevitch, D., Strom, S. E., et al. 1990, AJ, 99, 1187

Stammler, S. M., Birnstiel, T., Panić, O., Dullemond, C. P., & Dominik, C. 2017, A&A, 600, A140

Stammler, S. M., Drążkowska, J., Birnstiel, T., et al. 2019, ApJ, 884, L5

Steinpilz, T., Teiser, J., & Wurm, G. 2019, ApJ, 874, 60

Stoll, M. H. R. & Kley, W. 2014, A&A, 572, A77

Strom, K. M., Strom, S. E., Edwards, S., Cabrit, S., & Skrutskie, M. F. 1989, AJ, 97, 1451

Suzuki, T. K. & Inutsuka, S.-i. 2009, ApJ, 691, L49

Takeuchi, T. & Lin, D. N. C. 2002, ApJ, 581, 1344

Taki, T., Fujimoto, M., & Ida, S. 2016, A&A, 591, A86

Tanaka, H., Himeno, Y., & Ida, S. 2005, ApJ, 625, 414

Tazzari, M., Testi, L., Ercolano, B., et al. 2016, A&A, 588, A53

Teague, R., Bae, J., Bergin, E. A., Birnstiel, T., & Foreman-Mackey, D. 2018, ApJ, 860, L12

Toomre, A. 1964, ApJ, 139, 1217

Tripathi, A., Andrews, S. M., Birnstiel, T., et al. 2018, ApJ, 861, 64

Turner, N. J., Fromang, S., Gammie, C., et al. 2014, in Protostars and Planets VI, ed. H. Beuther, R. S. Klessen, C. P. Dullemond, & T. Henning, 411

Ueda, T., Flock, M., & Okuzumi, S. 2019, ApJ, 871, 10

van Boekel, R., Henning, T., Menu, J., et al. 2017, ApJ, 837, 132

Vericel, A. & Gonzalez, J.-F. 2020, MNRAS, 492, 210

Villenave, M., Benisty, M., Dent, W. R. F., et al. 2019, A&A, 624, A7

Wada, K., Tanaka, H., Suyama, T., Kimura, H., & Yamamoto, T. 2011, ApJ, 737, 36

Weber, P., Benítez-Llambay, P., Gressel, O., Krapp, L., & Pessah, M. E. 2018, ApJ, 854, 153

Weidenschilling, S. J. 1977, MNRAS, 180, 57

Whipple, F. L. 1972, in From Plasma to Planet, ed. A. Elvius, 211

Windmark, F., Birnstiel, T., Ormel, C. W., & Dullemond, C. P. 2012, A&A, 544, L16

Woitas, J., Leinert, C., & Köhler, R. 2001, A&A, 376, 982

Wünsch, R., Klahr, H., & Różyczka, M. 2005, MNRAS, 362, 361

Youdin, A. N. & Goodman, J. 2005, ApJ, 620, 459

Youdin, A. N. & Lithwick, Y. 2007, Icarus, 192, 588

Zhu, Z. & Stone, J. M. 2018, ApJ, 857, 34

Acknowledgements

I want to start by thanking my supervisor Til Birnstiel, for giving me the oportunity to start this PhD, for the countless discussions, for all the advise, and for managing to create a fun and healthy work environment.
I want to thank the Star and Planet formation group, and specially to Sebastian, Joanna, and Apostolos, for all the meetings, the support, and the Wonderful Wednesdays (a.k.a. Fabulous Fridays) lunches.
To the friends I met during the IMPRS: Maria, Souradeep, Francesco, Misa, and Jere, that made this three years so much fun, thank you so much for the time together, for the travels, the dinners, and the evenings of exploding kittens, a giant hug to all of you.
I want to send a big thank you to my parents, that have supported me through all my career and continue to do so even from the distance.
And most importantly, I want to thank Rima, for being the best wife in the world. For supporting when things were most difficult, for crossing the Atlantic back and forth to stay by my side, for holding my pieces together, for making me laugh, and for always being there for me.
To everyone that I didn't mention, thanks for everything. I couldn't have finished this PhD without all the huge amounts of help and friendship that I received from all of you.